January 2015

Investigation of Noise Sources and Propagation in External Gear Pumps

Timothy John Opperwall
Purdue University

PURDUE UNIVERSITY
GRADUATE SCHOOL
Thesis/Dissertation Acceptance

This is to certify that the thesis/dissertation prepared

By Timothy Opperwall

Entitled
Investigation of Noise Sources and Propagation in External Gear Pumps

For the degree of Doctor of Philosophy

Is approved by the final examining committee:

Andrea Vacca
Chair

J. Stuart Bolton

Monika Ivantysynova

John Lumkes

To the best of my knowledge and as understood by the student in the Thesis/Dissertation Agreement, Publication Delay, and Certification Disclaimer (Graduate School Form 32), this thesis/dissertation adheres to the provisions of Purdue University's "Policy of Integrity in Research" and the use of copyright material.

Approved by Major Professor(s): Andrea Vacca

Approved by: Bernard Engel 12/7/2015
Head of the Departmental Graduate Program Date

INVESTIGATION OF NOISE SOURCES AND PROPAGATION IN EXTERNAL GEAR PUMPS

A Dissertation
Submitted to the Faculty
of
Purdue University
by
Timothy J. Opperwall

In Partial Fulfillment of the
Requirements for the Degree
of
Doctor of Philosophy

December 2015
Purdue University
West Lafayette, Indiana

To my wife Stacey

ACKNOWLEDGEMENTS

First, I thank my major professor, Professor Andrea Vacca, for giving me the opportunity to work on exciting research related to my interests, and for creating a great work environment in his group at Maha Fluid Power Research Center. I thank him for demanding excellence by always trying to help me achieve my best. I am also grateful for my committee members Professor Monika Ivantysynova, Professor Stuart Bolton, and Professor John Lumkes for being willing to share their expertise in the fields of fluid power and acoustics.

For help setting up my experiments and simulations, I would like to thank my coworkers, with special thanks to Ram Devendran and Sidhant Gulati for aid in measurements and in creating new pump designs for me to analyze. Thanks to Anthony Franklin for his advice and practical problem solving in the lab. I would also like to thank Richard Klop and Paul Kalbfleisch for designing the anechoic room at Maha and getting the lab started on noise research under Professor Ivantysynova's direction. Many more thanks to my other coworkers for sharing the journey into research on hydraulic components and systems.

I want to thank my parents and siblings for supporting me unconditionally through all of these years of school. Also thanks for giving me the drive to learn and the courage to continue on in my education.

Most of all I would like to thank my wife Stacey for supporting me through all of this and for being willing to share my joys and struggles.

TABLE OF CONTENTS

Page

Page

LIST OF TABLES

LIST OF FIGURES

Figure Page

Figure Page

Figure Page

Figure Page

Figure Page

NOMENCLATURE

Symbol	Description	Units
A	Matrix of equations for nodal degrees of freedom	[N/A]
b	Gap width	[mm]
B	Matrix of equations for nodal degrees of freedom	[N/A]
c	Speed of sound in air	[m/s]
c_{eq}	Coefficient of discharge	[N/A]
C_s	Damping matrix	[N*s/m]
F_s	Boundary conditions set	[N]
F_a	Response force	[N]
F_s	Boundary conditions set	[N]
F_a	Response force	[N]
f_1	First frequency caused by number of tooth space volumes	[Hz]
h	Height of the gap	[μm]
I	Acoustic intensity	[W/m^2]
j	Imaginary operator	[N/A]
K_s	Stiffness matrix	[N/m]
k	Acoustic wavenumber	[1/m]
L_p	Sound pressure level	[dB]
L_C	Coupling matrix	[N/A]
M_s	Mass matrix	[m]
$\dot{m}$	Fluid mass flow	[kg/s]
N_a	Matrix of global shape function associated with nodes on surface	[N/A]
N_a	Matrix of global shape function associated with nodes on surface	[N/A]

Symbol	Description	Units
N_s	Matrix of global shape functions for unconstrained degrees of freedom	[N/A]
N_w	Matrix of global shape functions for constrained degrees of freedom	[N/A]
N_s	Matrix of global shape functions for unconstrained degrees of freedom	[N/A]
N_w	Matrix of global shape functions for constrained degrees of freedom	[N/A]
nc	Number of discrete displacing chambers	[N/A]
n	Shaft speed	[rpm]
p_{ref}	Reference pressure (20 μPa)	[μPa]
p_{rms}	Root mean square pressure	[Pa]
$\hat{p}$	Steady state acoustic pressure	[Pa]
p_j	Control volume pressure	[bar]
$\vec{r}_a$	Surface vector	[N/A]
$Re_{i,j}$	Reynold's number	[N/A]
r_1	First fundamental frequency of shaft	[Hz]
S	Structure surface area	[m^2]
T_s	Structure normal vector of the acoustic nodes	[N/A]
u	Velocity of the gap wall	[m/s]
$\hat{v}_n$	Surface normal velocity	[m/s]
V_{HP}	Outlet port volume	[mm^3]
V_{LP}	Inlet port volume	[mm^3]
$V_{1,i}$	Control volume for tooth space on drive gear	[mm^3]
$V_{2,i}$	Control volume for tooth space on driven gear	[mm^3]
V_j	Size of control volume	[mm^3]
$V_{var,j}$	Variable volume of control volume	[mm^3]
$\|v\|^2$	Spatially averaged mean square velocity	[m/s]
W_{ref}	Reference sound power level (1E-12 Watts)	[W]
W	Radiated power	[W]
θ	Angle of gear rotation	[deg]
ρ	Fluid density	[kg/m^3]
$\Omega_{i,j}$	Area of connection	[mm^2]

Symbol	Description	Units
μ	Dynamic viscosity	[Pa*s]
Symbol	Description	Units
$\widehat{w}_{(xyz)}$	Nodal displacement in x, y, or z	[m]
ω	Frequency	[rad/s]
ρ_0	Air density	[kg/m$^{3]}$
Δr	Distance between microphone pair	[m]
$\widehat{w}_{(xyz)}$	Nodal displacement in x, y, or z	[m]
θ	Angle of gear rotation	[deg]
μ	Dynamic viscosity	[Pa*s]
ρ	Fluid density	[kg/m^3]
ρ_0	Air density	[kg/m$^{3]}$
σ	Acoustic radiation efficiency	[%]
$\Omega_{i,j}$	Area of connection	[mm^2]
ω	Frequency	[rad/s]

ABBREVIATIONS

Name	Description
ABN	Air-Borne Noise
BEM	Boundary Element Method
CFD	Computational Fluid Dynamics
CSD	Cross Spectral Density
CV	Control volume
dB	Quantity is on the decibels scale
FFT	Fast Fourier Transform
FBN	Fluid-Borne Noise
FEM	Finite Element Method
FS	Full Scale, referring to sensor accuracy
EGM	External Gear Machine
EGP	External Gear Pump
GM	Gear Machine
HYGESim	HYdraulic GEars Machines Simulation
MPTR	Multi-Purpose Test Rig
PSD	Power Spectral Density
SBN	Structure-Borne Noise
SPL	Sound Pressure Level
SWL	Sound Power Level
TS	Tooth Space
TSV	Tooth Space Volume

ABSTRACT

Opperwall, Timothy J. MSME, Ph.D., Purdue University, December 2015. Investigation of Noise Sources and Propagation in External Gear Pumps, Major Professor: Andrea Vacca, School of Agricultural and Biological Engineering.

Oil hydraulics is widely accepted as the best technology for transmitting power in many engineering applications due to its advantages in power density, control, layout flexibility, and efficiency. Due to these advantages, hydraulic systems are present in many different applications including construction, agriculture, aerospace, automotive, forestry, medical, and manufacturing, just to identify a few. Many of these applications involve the systems in close proximity to human operators and passengers where noise is one of the main constraints to the acceptance and spread of this technology.

As a key component in power transfer, displacement machines can be major sources of noise in hydraulic systems. Thus, investigation into the sources of noise and discovering strategies to reduce noise is a key part of applying fluid power systems to a wider range of applications, as well as improving the performance of current hydraulic systems.

The present research aims to leverage previous efforts and develop new models and experimental techniques in the topic of noise generation caused by hydrostatic units. This requires challenging and surpassing current accepted methods in the understanding of noise in fluid power systems. This research seeks to expand on the previous experimental and modeling efforts by directly considering the effect that system and component design changes apply on the total sound power and the sound frequency components emitted from displacement machines and the attached lines.

The case of external gear pumps is taken as reference for a new model to understand the generation and transmission of noise from the sources out to the environment. The lumped parameter model HYGESim (HYdraulic GEar machine Simulator) was expanded to investigate the dynamic forces on the solid bodies caused by the pump operation and to predict interactions with the attached system. Vibration and sound radiation were then predicted using a combined finite element and boundary element vibro-acoustic model as well as the influence of additional models for system components to better understand the essential problems of noise generation in hydraulic systems. This model is a step forward for the field due to the coupling of an advanced interal model of pump operation coupled to a detailed vibro-acoustic model.

Several experimental studies were also completed in order to advance the current science. The first study validated the pump model in terms of outlet pressure ripple prediction through comparison to experimentally measured results for the reference pump as well as prototype pumps designed for low outlet pressure ripple. The second study focused on the air-borne noise through sound pressure and intensity measurements on reference and prototype pumps at steady-state operating conditions. A third study over a wide range of operating speeds and pressures was completed to explore the impact of operating condition and system design to greater detail through measuring noise and vibration in the working fluid, the system structures, and the air.

Applying the knowledge gained through experimental and simulation studies has brought new advances in the understanding of the physics of noise generation and propagation in hydraulic components and systems. The focus of the combined simulation and modeling approach is to clearly understand the different contributions from noise sources and surpasses the previous methods that focus on the outlet pressure ripple alone as a source of noise. The application of the new modeling and experimental approach allows for new advances which directly contribute to advancing the science of noise in hydraulic applications and the design of new quieter hydrostatic units and hydraulic systems.

1. INTRODUCTION

The introductory chapter is divided into several sections. First is a background and overview of the motivations behind the current work. Second is a general background and overview of sources and transmission of noise in hydraulic components and systems. The third section introduces the main reference case of the external gear pump (EGP). The fourth section explores the current state of the art in noise research in hydraulics. The final section of the introductory chapter covers the main research aims of the current work.

1.1 Research Motivation

Currently, oil hydraulics is the best technology for transmitting mechanical power in many engineering applications due to its advantages in power density, ease of control, layout flexibility, and efficiency. Due to these advantages, hydraulic systems are present in many different application including construction, agriculture, aerospace, automotive, forestry, medical, and manufacturing just to name a few. Many of these applications involve the systems in close proximity to human operators and passengers where noise is of the main constraints to the acceptance and spread of this technology. With the increase of environment health and safety standards such as OSHA 1910.95 (1990-2015), evaluating the amount of noise generated by hydraulic components has increased in importance. In lighter and quieter applications, the importance of the level of noise transmitting from the hydraulic components to the passengers and environment has developed into a primary design concern relatively recently. In order to increase the range of applications where fluid power is advantageous and acceptable, the noise generation must be better understood and ultimately reduced. Besides environmental concerns, decreasing the noise and vibration of hydraulic components has potential additional

benefits of improving control stability and increasing machine life and reliability. As the key component in power transfer, positive displacement machines can be major sources of noise in hydraulic systems. In many cases, the limiting factor in the adoption of hydraulic systems is the amount of noise and vibration introduced into the environment by the displacement machines, as opposed to the noise from valves, loads, and other hydraulic sources. Thus, investigation into the sources of noise is focused on the displacement machines and discovering strategies to reduce noise is a key part of applying fluid power systems to a wider range of applications. In particular, the applications for external gear machines (EGMs) have been widely researched under Dr. Andrea Vacca (2005-2015). These machines are selected as key component since open circuit pumps are required in nearly all hydraulic applications to deliver fluid from the tank to all the components of the hydraulic system. Due to their widespread use, EGMs are a key component for improving the noise performance of hydraulic systems.

1.2 Noise Sources in Hydraulic Systems

Study of the physical phenomena of noise is typically separated into three categories: fluid, structure, and air-borne noise which are presented in Figure 1.1. Separation of sources into three separate domains is a useful division which is common in many studies of noise in hydraulic applications. However, the connection between the three domains shows that the mechanics of noise generation are a singular and continuous process from the internal sources out to the environment.

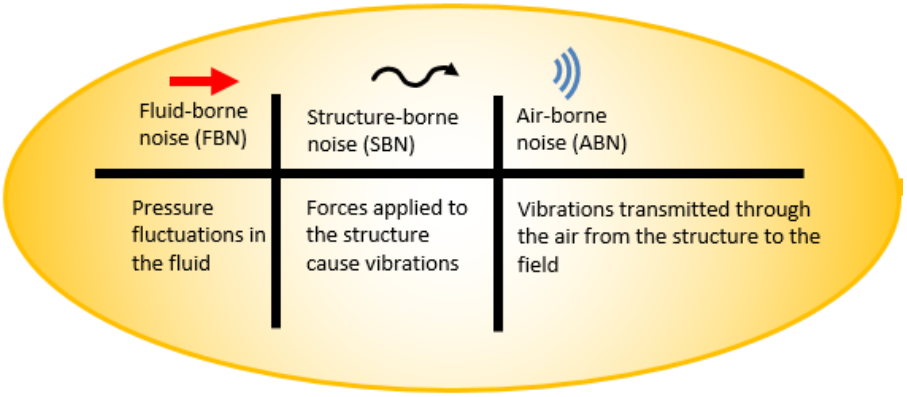

Figure 1.1 Noise approach in three domains

While many approaches are available to study the air-borne noise (ABN) for general acoustic applications, it is difficult to simulate the mechanisms of noise generation in hydrostatic units to predict the fluid-borne noise (FBN) and structure-borne noise (SBN) sources. The FBN can be composed of a variety of different phenomena. Primarily, there are large scale pressure fluctuations caused by the displacing action and the resulting loading forces. Additional point sources of noise can be localized cavitation, pressure peaks, and dynamic pressure gradients.

As the loads applied by the unit operation interact with the solid body of the pump and attached structures, the SBN can be separated into two main aspects. The structure is typically considered both as impedance for the transmission of FBN to the environment, and also transmits its own sources of noise in the forms of forces and moments carried by the moving components. In an axial piston machine, the main sources of SBN are the moments on the swash plate. In external gear machines, the main mechanical source of SBN is the contact forces between the two gears carried by the journal bearing forces.

A separate and large source of noise on these systems is often an electric motor or engine driving the hydraulic pump. Due to the high power density of hydraulic systems, engines and electric motors of equivalent power must be significantly larger in volume and mass relative to pumps of equal power. Independent of fluid power applications many studies have been completed by the automotive industry for reducing engine noise by all engine manufacturers such as Usuda et. al. at Toyota (2002). As research efforts reduce engine noise, this shifts motivation for the current study towards the hydraulic noise. Additionally, the noise from hydraulics can often be more irritating to the human user than the engine noise due to the higher frequency components.

As the most important component for noise in the hydraulic system, the internal sources must be better understood and the transmission of noise sources out the environment analyzed as shown in Figure 1.2. This summarizes and motivates for the sources of noise in a typical displacement machine. This includes the fluid behavior from the inlet through pressurization and delivery to the outlet, the bearing loads and structure-borne transmission, and finally radiation out into the air.

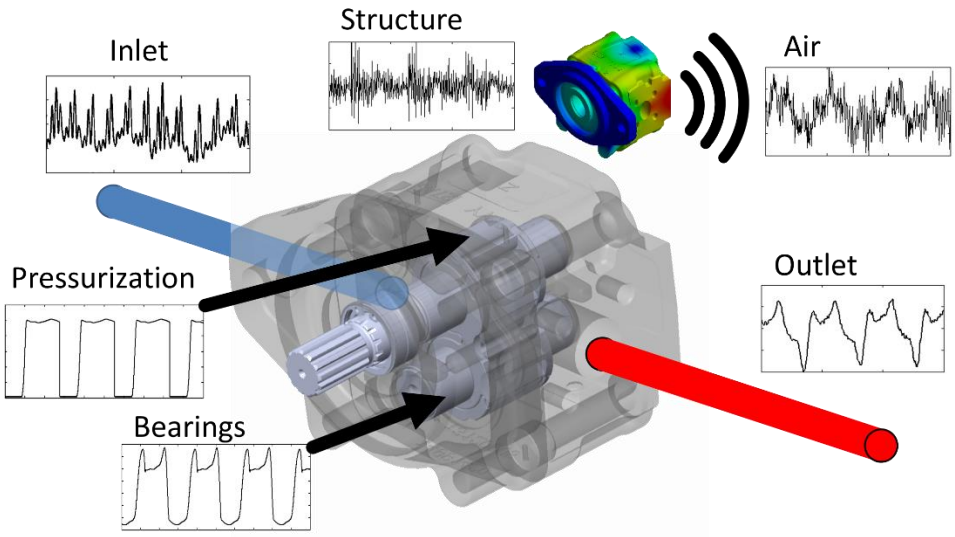

Figure 1.2 Noise sources and propagation in an external gear pump.

The goal of the research is to identify the important noise sources and how they propagate out into the system and the environment. All of the internal sources of noise to a displacement machine must propagate out through one of three available physical paths: first, through the fluid and out into the attached fluid system on the inlet or outlet of the machine; second, through the physical coupling of different solid bodies into the connected physical system (i.e. the shaft coupling, the pump flange and bolts, or hydraulic lines vibrated by the pump body); or third, in direct radiation of sound power from the surface of the pump body out into the environment.

Stepping through this propagation of noise from inside to outside, first there is the sound transmission from the displacement machine through the fluid and out into the hydraulic system. Attached lines with impedances have fluid harmonic frequencies where the mass and stiffness of the fluid along with the geometry of the lines interact to result in potential resonant behavior. This results in the formation of standing waves in the fluid, which large magnitude pressure oscillations and noise transmission. Furthermore, there can be significant interactions with attached loads and other components in a typical hydraulic system. Foremost of these are valves. Each valve has its own resonant frequencies and these are greatly excited by the oscillations present in that flow. Valve noise typically occurs at higher frequencies than pumps and motors due to the smaller mass of the components involved. There are also cases where internal orifices and volumes occur in

valves which result in low resonant frequencies. Rapid movement of actuators or valve spools can also result in noise generation from fluid momentum changes with effects similar to the water hammer effect as shown by Subani (2015). A second application of system level load interaction occurs in hydrostatic transmissions between couple pumps and motors. These are examples where the fluid forms the transmission path for oscillatory energy to pass from one component to the rest of the system where the combined performance is potentially worse than the sum of the individual components.

Other than the fluid path for noise to leave the displacement machine, the second path is to consider the coupling of the system due to mechanical and structural paths. The pump vibration can pass into the flange of the pump and then into the rigid structures of the machine that it is mounted to. Different types of mounting may mitigate this as a transmission path as shown by Skaistis (1988), but typically a stiff mounting must be used due to the large size of the displacement units. Second, the shaft of the displacement machines must be coupled to an engine or electric motor driving unit as previously mentioned. There is coupling between the engine shaft oscillatory dynamics to the torque oscillations in the hydraulic pump. Due to the discrete number of chambers in both engines and hydraulic pumps, there is uneven shaft torque throughout a single revolution which can introduce additional oscillations and vibrations to the system. However, simple experiments have shown more vibration transmitted from the prime mover into the displacement machine than vice-versa.

The final solid parts connected to a pump are the lines or pipes that move fluid to the system. In production machines these will be made of steel-braided rubber hose or steel pipes. Vibration of the pump body results in vibrations of the attached line structures. For rubber hoses, the compliance of the material reduces the propagation of energy through the structural path. For steel pipes, fully rigid connections should be avoided due to creating structural paths for vibrations to transmit from the vibration of the pipe and the fluid inside the pipe into additional system components.

The final path and the one that is generally of most interest to commercial ventures is the radiation from the solid surfaces of all the hydraulic components into the air and out into the environment. Fluid-borne noise sources at the inlet and outlet eventually propagate

out through the pump body and lines. Furthermore, the effect of pressure gradients, cavitation, and structure-borne noise need to evaluated in terms of their contributions to the overall radiated noise. Here is where all of the considerations must intersect in order to better understand the most important features in noise generation and propagation in hydraulic systems.

1.3 Reference Case of the External Gear Pump

The mechanics of noise generation are very similar between all types of positive displacement machines due to the physics of displacing action and oscillatory loads. The research methods are suitable for a wide range of different types of machines and different designs within those types as will be described in the state of the art section following. A widely used type of displacement machine, the external gear machine (EGM) is taken as a reference for this study with the particular case of the external gear pump (EGP). The relative sizes of units under consideration range from 10 cc/rev up to 40 cc/rev with maximum speeds up to 3600 rpm and pressures up to 250 bar.

The present research aims to leverage previous efforts in the topic of noise generation in hydrostatic units while developing new methods to predict air-borne noise for the reference machine. In axial piston type units, the number of displacing chambers is generally less than eleven due to size and complexity/cost limitations of the rotating kit. The selection of number of pistons is a primary design concern for axial piston machines. The smaller number of displacing chambers generally leads to larger flow oscillations and therefore larger sources of noise due to the oscillating pressure and force loads and the design of such is shown by Ivantysynova (2009). The case of external gear machines often has twelve or greater number of teeth on the gears, the elevated number of chambers already limits the pulsations due to the displacing action compared to axial piston machines.

Gear pumps and motors have major advantages in many types of fluid power applications. Primarily, they are very robust and durable. They are also inexpensive to manufacture with respect to other types of displacement machines due to their small number of parts and simple principle of operation. The key components of an EGP are the

drive gear and driven gear. The drive gear is directly coupled to a source of mechanical energy such as electric motor or engine as discussed in the previous sections. The contact forces between the gears provides for sealing and smooth transfer of energy. The final primary feature in an EGM is the lateral pressure plates which provide for the lateral sealing, bearing, and grooves for timing of the machine as shown in Figure 1.3.

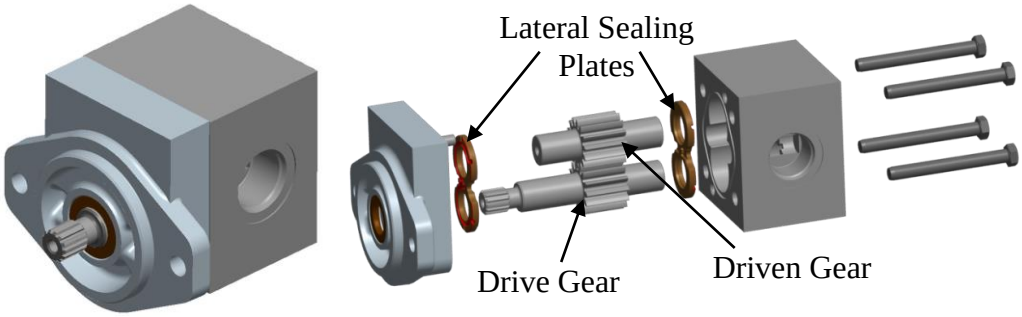

Figure 1.3. Internal components of a typical pressure compensated external gear pump.

In high pressure EGM designs, the lateral plates are pressure compensated; they are specifically designed to float between the casing and the gears in order to provide good sealing on the lateral faces of the gears. These also provide lateral lubrication and load support. Additionally, many common EGPs use thicker lateral plates with pressed journal bearing built into the floating blocks. Reference Pump #1 and #2 use pressure plates, while Referece Pump #3 implements the journal bearings into the lateral bushings. These two common designs cover the vast majority of the high pressure EGM market. Grooves are often added to the lateral plates in order to control provide better pump performance.

The displacing action in an EGM is achieved by the meshing of two gears, which causes the changes of the volume inside every tooth space volume (TSV) in each gear. The fluid is brought into the TSVs on the inlet side; it is then carried around the sides of the gears by the teeth. The displacing action occurs, where the fluid in the TSV is delivered to the output port, then new fluid is drawn from the inlet port. Both mechanics are accomplished by the meshing of the gears during the displacing action. A typical pressure profile from one TSV is shown in Figure 1.5.

There are many different designs for external gear pumps. The chosen reference pumps are among the most successful designs for high pressure (up to 300 bar)

applications. The pump body is typically composed of two or three pieces which enclose the gears and have machined ports for connecting the pump to a hydraulic system. An example simplified geometry of an external gear pump is shown in Figure 1.4. The angle frame of reference is shown in yellow where the starting angle is the axis between the gears and the rotation is towards the inlet from the starting angle.

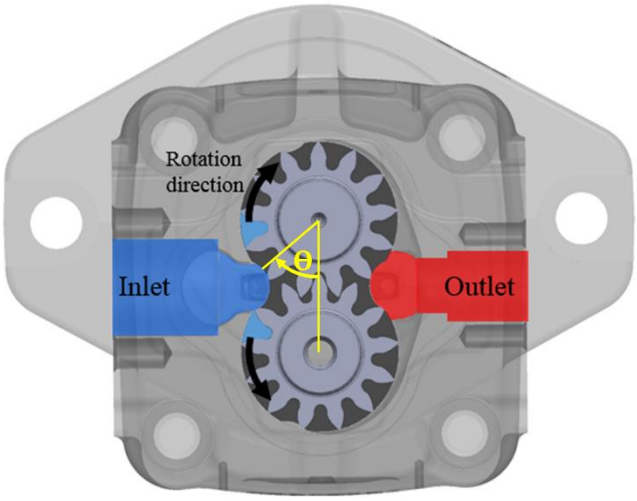

Figure 1.4. Typical external gear pump.

However, in EGMS, the displacing action occurs over a shorter portion of the machine revolution as shown in Figure 1.5 as opposed to the sinusoidal volume variation over each revolution in an axial piston machine. This rapidly changing volume can lead to large pressure peaks or cavitation inside a particular tooth space volume (TSV).

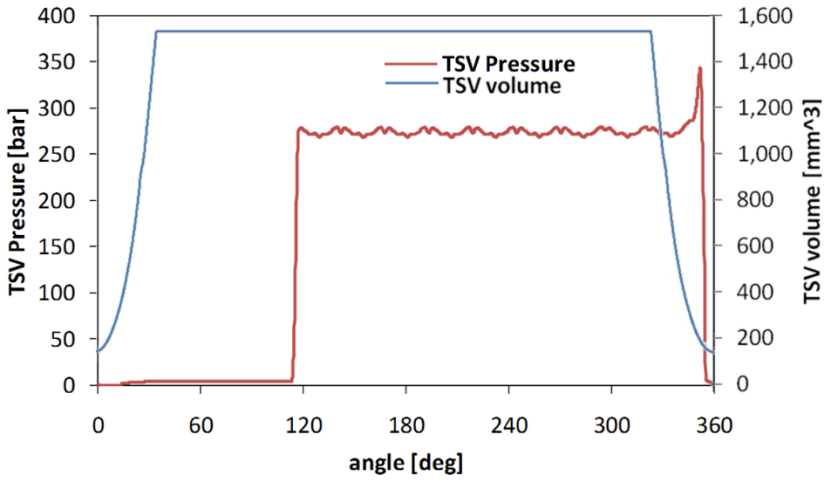

Figure 1.5 Typical EGM working volume and pumping chamber pressure.

Noise and vibration are introduced into the system due to the discrete amount of pumping chambers. The flow delivered is uneven, which produces time transient pressure and force oscillations when acting against a load. Additionally, each chamber generally sees an oscillation from the inlet to the outlet pressure and back through the course of one shaft revolution seen at 110º and 355º. This force oscillation in the chamber during the chamber pressurization is a much greater magnitude than the inlet of outlet dynamic pressure fluctuations. When the fluid pressure changes rapidly, localized cavitation and air release can also happen in the fluid from 0º through 10º. Introduction of air vapor into the pump operation due to cavitation is undesirable due to loss in volumetric efficiency due to delivery of the air, and also because rapid pressurization of air vapor bubbles causes bubble collapse, which in turn can cause noise generation and solid surface degradation. In many types of displacement machines, there are also parts in solid contact or in hydrostatic/hydrodynamic force balances which are vulnerable to oscillating forces which result in micro-motion of the gears relative to the housing and motion of the lateral sealing plates relative to the gears and pump housing. An essential part of understanding external gear pump operation from a standpoint of noise generation is the modeling of the internal phenomena. A significant issue in the performance of displacement machines is flow pulsations created by the finite number of displacement chambers. During the meshing process, fluid can be trapped between the points of contact of the gears, this leads to pressure overshoots in the trapped regions. When the trapped volume begins to increase in volume again as it leaves the meshing zone, the pressure inside the tooth space volume (TSV) may also go below the vapor pressure of the fluid and cause the release of entrained air or violent suction flow.

When each TSV is trapped between the points of contact during the meshing process as shown in Figure 1.6, it is advantageous to avoid isolation from both the inlet and outlet ports while the volume is changing by connecting the volume to either the inlet or outlet port through grooves on the lateral pressure plates. This leads to smoother pump operation and a lower magnitude flow fluctuation.

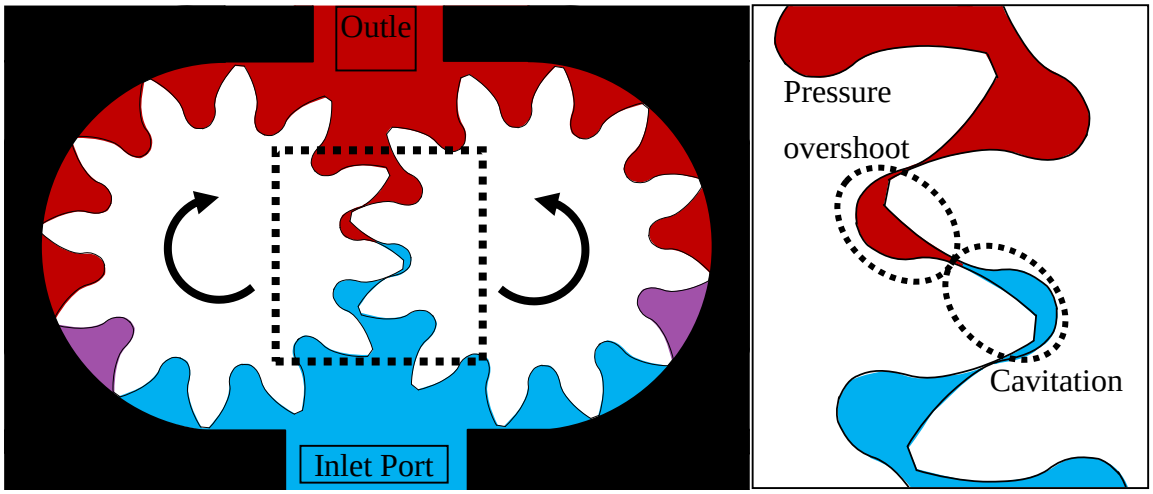

Figure 1.6: Principle of operation of external gear machine.

Much research has been done on minimizing the pressure ripple in hydraulic lines both through improvements to the displacement machines through manipulation of grooves on the lateral bushings of EGMs. These grooves are also referred to as the suction groove on inlet side, the delivery groove on the outlet side, and the high speed backflow groove along the edge of the plate typically connected to the HP side and its presence is indicated by the TSVs colored in red in Figure 1.6. These delivery and suction grooves allow for precise timing of the connections between volumes are highlighted in Figure 1.7 according to their placement in the pump casing shown in Figure 1.3.

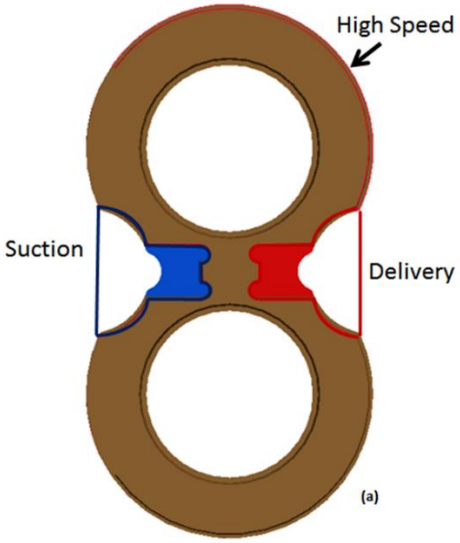

Figure 1.7: Lateral pressure plates with grooves highlighted.

Three main reference pumps were examined for the present work, the differences in size and teeth numbers are shown in Table 1.1.

Table 1.1: Reference pump specifications.

Pump#	Description	Displacement	# of Teeth
1	Pressure compensated design	22cc/rev	13
2	Pressure compensated design	38cc/rev	14
3	Pressure compensated design	12cc/rev	12

All three pumps were modeled in HYGESim (Hydraulic Gear machine Simulator). Reference pump #1 was used for the acoustic modeling and several experimental studies. Reference pump #2 was used for an optimization effort for reducing noise, and Reference Pump #3 was considered for the cavitation and inlet ripple study shown in Chapter 6. Evaluating several different designs is useful in order to compare and contrast differences in operation and noise generation.

For Reference Pump #1, a study was completed for modifying the backflow groove to smooth the pressurization timing and compare to the unmodified design. For Reference Pump #2, an new design for the lateral pressure plates was created for reduced outlet pressure ripple. This design is experimentally compared to Reference Pump #2 in Chapter 4. Finally, for Reference Pump #3, an extreme design modification was made in order to test hypotheses about the presence of noise at the inlet of the pump. This study is shown in Chapter 6.

1.4 State of the Art

Hydraulic systems occupy an important role in both on and off-highway vehicles. Designing for improved noise performance of fluid power systems is an essential part of improving current systems and opening up new applications. As the technology advances and spreads to lighter applications, the noise generation and propagation from hydraulic components becomes a primary design concern. The present work is motivated by the need for a better understanding of noise sources and propagation in hydraulic systems. The focus in most research on noise in fluid power is on reducing the peak to peak magnitude of the

pressure ripple at the outlet of displacement machines. This pressure ripple in pumps can be characterized using the ISO 10767 standards. The reduction of pressure oscillations is usually accomplished through manipulations of the volume connections using grooves such as the ones shown in Figure 1.7, or in the specific case of external gear machines, it can also be accomplished though changing the instantaneous volumes themselves, accomplished with geometry changes of the gears. Primarily, these past efforts are focused on only the peak-to-peak magnitude of the FBN. That is, the highest overall peak in the time domain is minimized with the expectation that the overall design will be quieter. Prototyping and design of new displacement machines is often done by trial-and-error procedures, but has also been accomplished through design changes guided by the use of advanced models and simulation-based optimization techniques, such as the studies by Devendran et al (2013) for external gear machines or by Seeniraj et al (2009) for axial piston units, just to mention some significant works in this area. These works often emphasize on the internal sources of FBN, such as work done by Mucchi (2014). Some work also focuses on reducing internal sources of structure-borne noise (SBN). In the example of axial piston pumps, the moments around the swash plate are considered strong sources of SBN which results in a large amount of case vibration. The work at Maha Fluid Power Research Center on designing new external gear machines has extended the focus on the FBN to include not only the peak-to-peak magnitude of the FBN, but also to consider all frequencies present in the pressure ripple as part of design optimization of the machine.

All the noise sources in the FBN and SBN have an effect on the total radiated air-borne noise (ABN). However, a method of quantifying the impact that different noise sources have on the radiated noise variables is not clear from a design perspective. This is the fundamental problem this research addresses. Previous efforts related to this work have focused on modeling the sound radiated from the pump body as well as the influence of the attached lines (Opperwall, 2013-2014). However, modeling efforts alone have been insufficient to identify the different noise sources and transmission paths due to the complexity of the problem.

Difficulty in modeling the sources of noise comes mainly from the complexity of simultaneously modeling pump phenomena such as fluctuating fluid pressures on internal

surfaces, pressure peaks, cavitation, contact forces, and bearing performance. At Maha Fluid Power Research Center of Purdue University, modeling the operation of gear pumps and axial piston pumps has advanced through the development of multi-domain simulation models that combine different simulation approaches. The simulations aim to carefully analyze the complex fluid, structure, and thermal interactions characterizing the flow and the lubricating gap behavior in these machines with Vacca (2011) focusing on external gear machines and Ivantysynova (2009) focusing on axial-piston type machines.

Research by Casoli et al (2008), Vassena and Vacca (2010), Devendran and Vacca (2012), for EGMs; and Seeniraj (2008, 2011), Ericson et al.(2009) for the similar case of axial piston units has been done to reduce these primary pressure fluctuations through design optimization. However, although empirical approaches have been investigated, as discussed in Hartmann et al (2012), for all different designs of hydrostatic units there is not a clear correlation between the features of the pressure ripple and the ABN. Because of this, additional research is required to better understand the relationship between the FBN and the ABN, and other sources of noise in the displacement machine. This includes all internal sources of noise including pressure transition regions and inlet cavitation which have not been comprehensively studied previously in EGMs.

1.4.1 Solutions to reduce noise

An important part of the state of the art is the current implementation of quiet pump designs by industry. There are general methods for solutions to reduce noise which are generally focused on adding porting grooves between the inlet and outlet volumes and the pumping chambers. There are many efforts by researchers specifically conceived to reduce these sources of noise emissions in EGMs. In particular, design methods for the lateral sealing plates are described in Casoli and Vacca (2010) and in Wang et al (2011) aimed to realize an optimal and gradual timing for the commutations between the TSVs and the inlet and outlet ports. Beyond manipulations of the port connections in external gear machines, there are also advanced designs of the gears which provide for either better sealing or smoother operation. In particular, there are dual flank contact designs where each tooth contacts both adjacent teeth on the other gear during the meshing process as shown by

Negrini (1996). The gears in the Reference Pump #1 and #2 contact on a single flank, while some external gear pump designs use dual-flank gears which remain in contact in two places during meshing as shown in Figure 1.8.

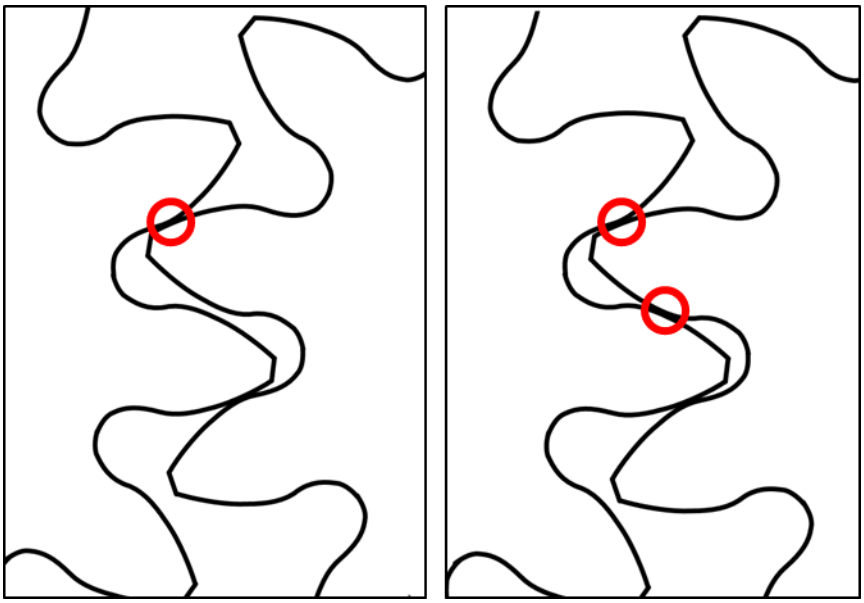

Figure 1.8 Single-flank contact (left) and dual-flank contact (right) gear designs.

The suggestion of mismatched pairs of gears as a source of noise was investigated by Mucchi (2010). There are also less cost effective solutions based on helical gear designs with epicycloidal profiles which provides for nearly continuous delivery of flow to the outlet as shown by Lätzel (2012). Another design option pursued for noise is asymmetric gear profiles. These types of designs are currently in use by large scale pump manufacturers. A limitation of these efforts is that they are based only on kinematic evaluations, meaning, they consider only the displaced volume or number of teeth. This shows the need for a comprehensive model in order to understand the importance of different frequency and compressibility effects on the noise generated by the pump.

Many researchers have tried to reduce the radiated noise by minimizing the pressure ripples in the lines of hydraulic systems. This has been done using targeted attenuators such as Helmholtz resonators and expander mufflers demonstrated by Ortwig (2005) shown in Figure 1.9 and Figure 1.10. Other concepts relating to attenuating line pressure ripple were presented by Earnhart and Cunefare (2012).

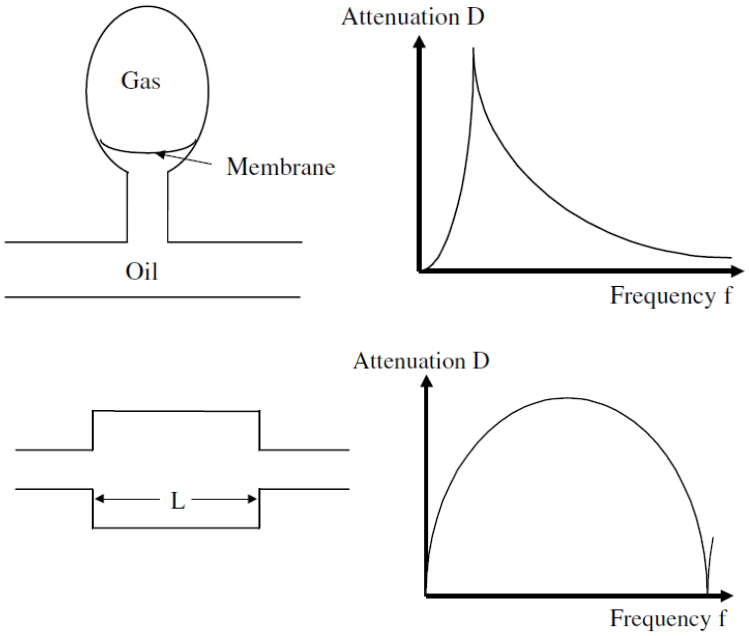

Figure 1.9: Standard types of passive dampers in noise transmission by Ortwig (2005).

In these cases, the attenuators damp the FBN in a targeted frequency range. However, this approach leads to more complicated and expensive systems and is limited to targeted frequencies. An additional limitation is that small variations in the excitation frequencies can result in a large reduction in attenuation effectiveness.

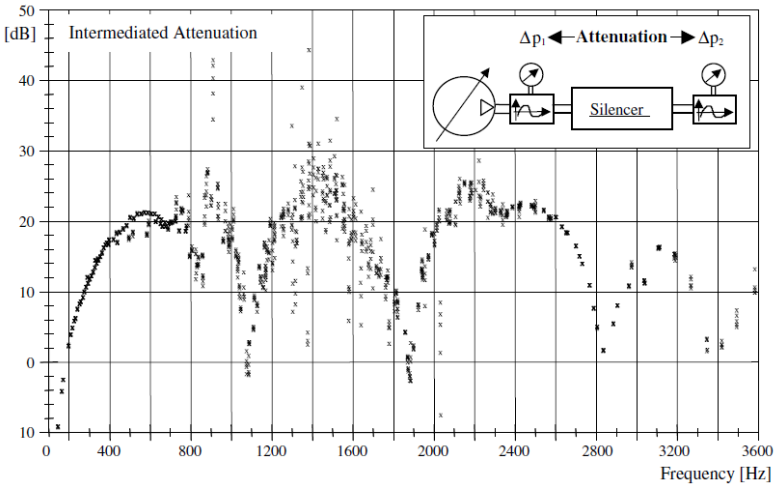

Figure 1.10: Resulting attenuation for passive dampers by Ortwig (2005).

Another attenuation method uses an adaptive Helmholtz resonator in the system with a variable length cylinder to reduce frequencies in a key range Kela (2010). This

allows for the system to respond to the excitation frequencies to remain at maximum effectiveness for different operating conditions.

Modeling noise from cavitation shockwaves was completed by Seo (2008), and a computational fluid dynamics (CFD) code for a cavitation model by Singhal (2002). There was also a study of sound generation from turbulence using CFD by Seror (2001), and the simulation and measurement of noise from jet streams using numerical simulations was done by Moore (2007). A proposed source of noise in the journal bearings in external gear machines was presented by Bonanno (2008).

An exploration into noise source identification and reduction in farming equipment with hydraulic systems was done by Balaban (2010). Edge (1999) presents a variety of methods for designing quieter hydraulic systems. Fiebig (2007) ranked sources based on the entire hydraulic system. He found that the frequencies of the pressure ripple are the main frequencies present in the noise radiated. He damped the system by submerging the pump in the oil tank. Fiebig also modeled and designed a pump using compression filter volumes connected to the trapped volumes in the meshing zone (2010). This solution is aimed to improve the noise emission in traditional external gear machines. There are several other solutions for positive displacement machines. Seeniraj (2009) worked on optimizing axial piston machines through use of silencing grooves and pre-compression filter volumes. This proved effective at reducing FBN and resulted in much smoother operation.

1.4.2 Efforts for modeling noise propagation

There are many developments in techniques to model and understand the noise generation of various types of rotating machinery. These types of machinery typically have strong peaks in frequency in the ABN due to the highly cyclical nature of their operation. An early model of noise was done by Jeannon (1975). In this model of a gerotor pump, an approximation was made by modeling a single piston source in an infinite baffle. Various approaches were also tried as demonstrated by Kesseler (1999) who used a modal analysis approach for modeling rotating machinery. In another model for noise analysis, Nandi (2004) examined the fluid-structure interaction problem for sound radiation from a

refrigeration compressor. Still later, a finite element and Rayleigh Integral approach to predicting noise radiation of a gearbox was used by Abbes (2008).

There are also a variety of solutions for measuring the noise of rotating machinery, with Cho and Bolton (2004) with a statistically optimized acoustic holography to locate sources of noise radiation. Instrumentation for measuring noise and vibration in fluid power systems as well as types of passive damping and noise reduction were presented by Gerges (2011). Measuring sound intensity in an anechoic chamber for a hydraulic transmission was completed by Klop and Ivantysynova (2010). Klop and Ivantysynova (2008) also investigated reducing noise sources in the cylinder pressures and swash plate moments in axial pistons machines and studied system interactions between pumps and motors and the length of the intermediate lines.

From a classical structural acoustics point of view, Cremer (2005) explained that generation of the noise in this case is the oscillatory pressures and the resulting forces on the structure. The forces then propagate throughout the structure, and the finally radiate to the surroundings. Advanced methods that are most similar to what is proposed by this thesis were shown in a finite element method (FEM) and boundary element method (BEM) model for an axial piston machine using basic equations for the input loads to predict surface vibration and radiation of noise Yamazaki and Kojima (2003), and by Schleihs and Murrenhoff at the University of Aachen (2014,2015). A model in predicting sound power from an induction motor also used FEM/BEM shown by Wang (2004).

BEM computational approaches have been improved through using Modal Acoustic Transfer Vectors (MATVs) to increase simulation speed for simulating multiple operating point in rotating machinery, which are independent of the load condition McCulloch (2002). A simplification can be made by observing the participation of the various modes by Lau (2004). A model of the response of a structure with an acoustic cavity which compared a finite element model to a modal matching technique was done by Puri (2007). A BEM model for a gearbox of a centrifuge achieved noise reduction via modification of casing material properties for attenuation in a certain frequency range as shown by Engelen (2009). More structure designs based on minimizing radiated sound power was shown by Constans (1998), and structurally optimizing to reduce radiated sound

power by Choi (2011). There are also several recent books which describe methods for calculating radiation from structures by Vasques (2011) and Cremer (2005).

1.5 Research Aims

The primary goal of this research is to advance the understanding of the noise generation and propagation in external gear pumps. More specifically, it is to enhance understanding of the phenomena connecting pressure and force fluctuations to radiated noise, and to formulate ideas for the design of quieter and better performing pumps and motors. The primary aims of the research are as follows:

(1) Accurately model the fluid-borne noise for the reference EGPs and attached lines using the pump model HYGESim with the goal of identifying all important internal sources in the FBN.

(2) Validate the pump model for the reference external gear pump through experimental study of the fluid-borne noise in a steel pipe connected to a reference EGP.

(3) Model the vibro-acoustic behavior of typical hydraulic unit with a focus on a reference EGP.

(4) Measure the noise generation and propagation in multiple domains over many different operating conditions to gain a complete picture of the pump operation with respect to noise.

(5) Experimentally study the impact additional system components in order to better understand the propagation of noise from the internal sources out the environment.

To accomplish the first aim, a methodology is needed to take advantage of existing fluid dynamic tools. Pressure fluctuations must be accurately modeled to capture the main components of fluid-borne noise. The lines in a physical system must be included to allow for a comparison and validation of the predicted pressure ripple for the second aim.

The third aim is accomplished by multiple analyses and modeling efforts based on understanding the noise propagation as it moves from the internal sources modeled by HYGESim and then through the structural and acoustic domains modeled by finite and boundary element methods.

Once the nature and generation of the internal sources is understood, the noise generation can be quantified experimentally by determining radiated sound power intensity

off a physical EGP and the attached lines using the semi-anechoic chamber and testing equipment present at Maha Fluid Power Research Center. These measurements will determine sound pressure level (SPL) and sound intensity (used to calculate total sound power level SWL). The total SWL of the pump can be used as a benchmark for design improvements, and plots of sound intensity on a virtual grid surrounding the pump can help guide design of noise-reduction solutions. Quantifying the noise performance as dependent on operating condition is a primary concern of the study.

With a proven simulation approach, investigation will move to a further level with reduction of noise sources identified during the experimental and simulation studies. Management of the sources of noise can be used as design variables for the existing pump optimization algorithms for external gear machine design by researchers under Dr. Vacca. Starting from a clear understanding of noise generation phenomena will permit the reduction of noise generation in the design phase of the unit.

2. EXTERNAL GEAR MACHINE FLUID MODEL

The reference displacement machine considered for the remainder of the document is the reference external gear pump. Although they are inexpensive, their operation is characterized by several aspects that are very difficult to simulate. This chapter is divided into sections covering an introduction to the pump model, the lumped parameter fluid dynamic model development, and results of the model. This model also serves as the basis for further development in understanding noise sources in EGPs through validation experiments.

2.1 Introduction to HYGESim

One of the main reasons for modeling displacement machines is to better understand the mechanism of flow and pressure pulsations. The model described in this section has been under development by researchers under Dr. Andrea Vacca at Maha Fluid Power Research Center of Purdue University. This model is named HYGESim (HYdraulic GEar machines Simulation).

The modeling activity proposed here takes advantage of an existing simulation model for EGP which was presented and validated by Vacca and Guidetti (2011). The main focus for noise modeling is on the force and pressure oscillations caused by the main unit in pumping operation. Other noise sources such as cavitation and pressure peaks are included in the lumped model. The main characteristics of the pump model operation are shown in Figure 2.1.

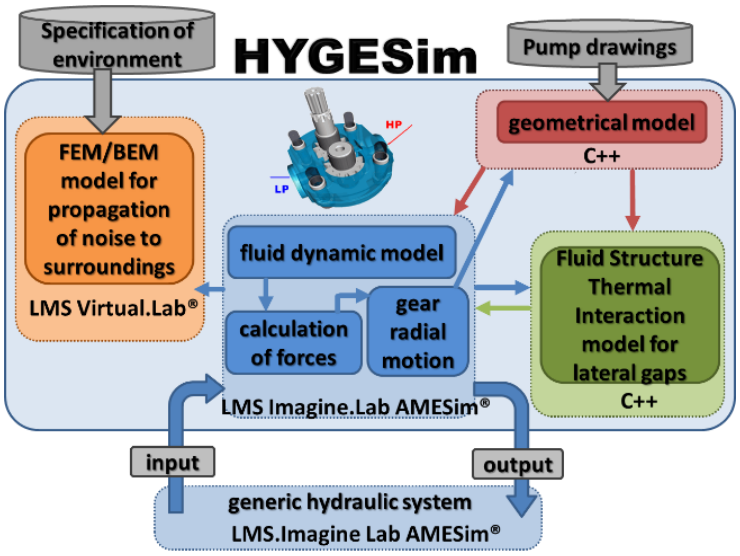

Figure 2.1 Layout of pump model

Pressures and flows inside the pump casing and the interior of the lines are found through a combination of an advanced geometric model and customized submodels coded in C++ in the AMESim environment. The outputs of this model are used as the main inputs for the acoustic models discussed in Chapter 3.

HYGESim permits the study of the machine when it is used in generic or specific circuits. This allows a prediction of the flow resulting from the interaction between different hydraulic systems with the external gear machine. The geometrical model provides the different orifice areas and control volumes at each angular step of rotation of the gears for the lumped parameter approach. The fluid dynamic model evaluates the flow through the machine, the pressure inside the TSV, and also the different forces acting on the gear. The most advanced version of the model also calculates contact forces and casing wear in the machine as well as predicting the axial balance of the machine.

The model has been leveraged for use not only in simulation of existing solutions, but also for design purposes as has been published in the works of Vassena (2010) and Devendran (2012, 2013) for optimal design of grooves and gears, and Thiagarajan (2014) for optimization of the axial balance. New designs have been produced and validated, and the tool is used to optimize not only for volumetric efficiency, but also for the design of quieter gear machines.

2.2 Lumped Parameter Pressure Model

The external gear machine model under development at Purdue University combines several simulation strategies to create an efficient model for different fluid phenomena. The principal design of the model involves four main control volumes. They are the inlet port volume, the outlet port volume, the set of control volumes for the tooth space volumes (TSVs) in the drive gear, and the set of volumes for the TSVs in the driven gear.

As represented in Figure 2.2, the model can simulate the unit starting from the CAD drawings of the machine. HYGESim solves the main flow through the unit considering the radial micro-motion of the gears and the features of the lubricating gap flow between the gears and the lateral bushings. This section provides a simplified description of the fluid dynamic model used by HYGESim used in the following part of this research. Further details about HYGESim can be found in Vacca and Guidetti (2011), Vacca et al (2011), and in Dhar (2012).

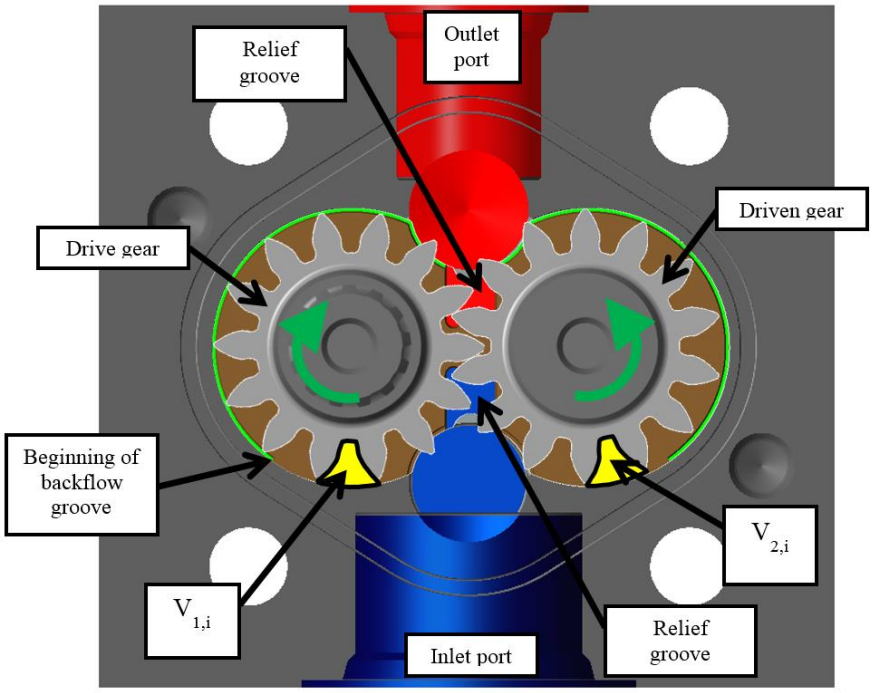

Figure 2.2. Key features of the reference EGP.

The external geometric model converts standard CAD files into area plots for connections between the various control volumes shown in Figure 2.3. This is an abstract way to picture the different volumes of the machine shown in Figure 2.2. The two pistons V_1 and V_2 represent the volumes occupied by the set of TSVs. The connections to the LP and HP volumes represent the time in each revolution when the TSV is connected to the inlet or outlet ports of the pump. According to the lumped parameter approach, the pump is subdivided in a number of control volumes in which fluid properties are assumed uniform and only time dependent. As shown in Figure 2.3, the model considers a control volume (CV) for each tooth space volume of both gears. Under the hypothesis of same number of teeth on the drive and the driven gears, as the shaft rotates, the particular tooth space volume $V_{1,i}$ of driver gear always meshes with the corresponding $V_{2,i}$ of the driven gear.

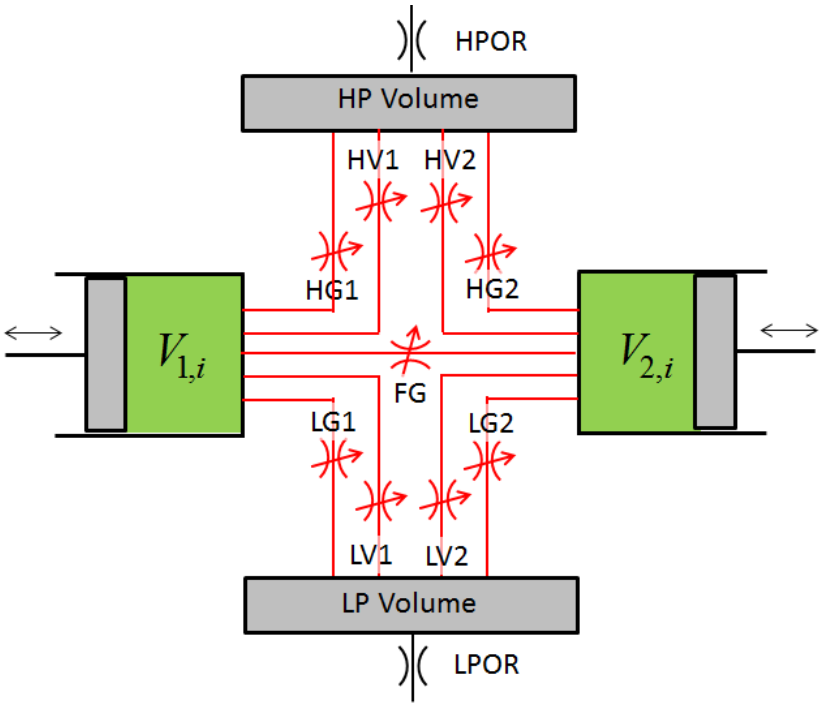

Figure 2.3: Elementary control volume connections for HYGESim model.

The diagram in Figure 2.3 shown is simplified to emphasize the key control volumes and connections in an external gear machine. The descriptions of these key connections are shown in Table 2.1. For the simplified model, the laminar flow equation is used for flow around the gear tooth tip as described in the subsequent sections.

Table 2.1: Descriptions of connections between the various control volumes.

	Description
FG	Connection between the two corresponding TSVs (the connection is closed outside the meshing zone).
HV	Connection between the TSV and the HP volume through the gear whole depth.
LV	Connection between the TSV and the LP volume through the gear whole depth.
HG	Connection between the TSV and the HP port through the recesses machined on the lateral pressure plates.
LG	Connection between the TSV and the LP port through the recesses machined on the lateral pressure plates.

The connections between the TSVs and the grooves on the lateral plates are shown by the HG and LG connections in Table 2.1.

The model takes into account the different connections between the TSV and the surroundings as well as the changing of net volume in the meshing zone. The pressure inside the volume as a function of fluid properties, geometric volume variation and the net mass transfer with the adjacent volumes can be given by the pressure build up equation from Vacca (2011).

$$\frac{dp_j}{dt} = \frac{1}{V_j}\frac{dp}{d\rho}\bigg|_{p=p_j}\left[\sum \dot{m}_{in,j} - \sum \dot{m}_{out,j} - \rho\bigg|_{p=p_j}\left(\frac{dV_j}{dt} - \frac{dV_{var,j}}{dt}\right)\right] \quad (2.1)$$

The summation terms in brackets are used to indicate the overall mass flow rates entering and leaving a particular control volume (CV). The term V_i represents the instantaneous volume of the considered CV. In case of a TSV in a gear pump, the displacing action is obtained by means of the variability of this volume.

The flow areas connecting each TSV with its surroundings and the actual values of volumes are considered depending on the shaft angular position. In this way, the pressure inside each CV can be predicted accurately. By also considering the performance of the

shaft journal bearings, the inter-axis micro motion of the gears can be predicted, which in turn can be used to predict casing wear. The mass flow equations are shown in Equations 2.2 and 2.3 from Vacca (2011). For turbulent flow,

$$\dot{m}_{i,j} = \frac{(p_i - p_j)}{|(p_i - p_j)|}\rho(\overline{p_{i,j}})c_{eq}(Re_{e,j})\Omega_{i,j}(\theta)\sqrt{\frac{2(p_i - p_j)}{\rho(\overline{p_{i,j}})}} \tag{2.2}$$

For laminar flow in simplified gaps at the tooth tips

$$\dot{m}_{i,j} = \rho\left[-\frac{h^3}{12\mu}\frac{p_i - p_j}{L} + \frac{uh}{2}\right]b \tag{2.3}$$

Where u is the velocity and h, L, and b are the height, length, and width of the gap respectively.

A more advanced version of the model can also be used for detailed analysis as shown in Figure 2.4. Instead of relying on the laminar flow equation for the flow in the lateral gaps, the coupled CFD gap model for considering the phenomena in the lateral gap has been added. The adjacent TSVs are connected to a particular TSV through two different main leakages. The first is around the tip of the tooth through the clearance between the gear tip and the casing. The second leakage is through the lateral gap between the gear lateral face and the lateral pressure plate. The lateral leakage is calculated by the coupled CFD code (Dhar, 2012).

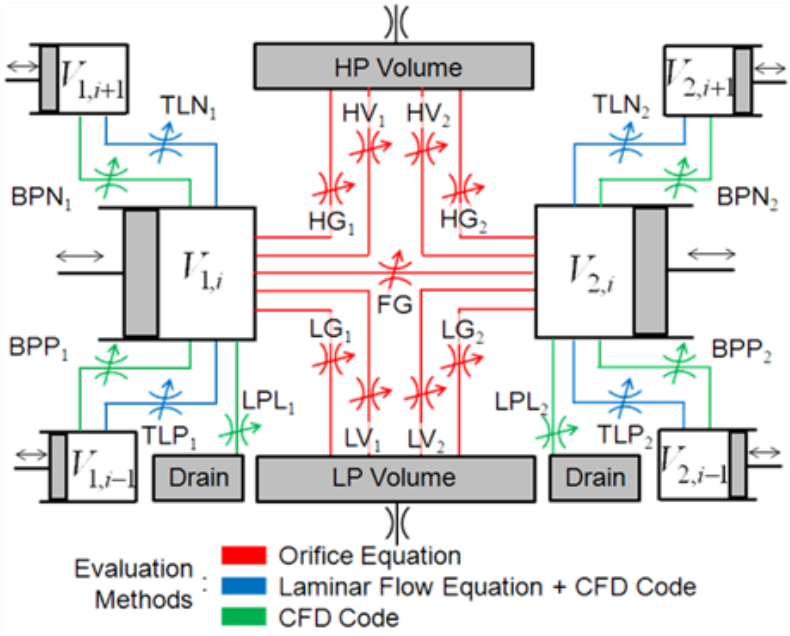

Figure 2.4: Connections between control volumes in HYGESim.

A description of the additional connections is shown in Table 2.2.

Table 2.2: Additional connections in the coupled CFD model.

	Description
TLP TLN	Leakages between adjacent TSV due to clearances among tooth tip and casing. TLP refers to the connection with the previous TSV on the same gear, while TLN is for the connection with the following TSV.
TTL	Leakage from radial gap flow into lateral gap from the tooth tip, subtracted from TLP and TLN.
TSL	Leakage from TSV into lateral gap.
BPL	Connection between a tooth space volume and shaft bearing.
LPL	Leakage from low pressure into lateral gap.
HPL	Leakage from high pressure into lateral gap.
DL	Leakage from lateral gap into drain.

The CFD model takes care of the evaluation of the various hydrostatic and hydrodynamic effects taking place in the lateral gaps of the machine and also for the axial motion of the lateral pressure plates. More information about the externally coupled model is found in Vacca, Dhar, and Opperwall (2011). The pressure boundary conditions are provided by the HYGESim fluid dynamic module. The finite volume solver then calculates the pressure and flow fields in the lateral gap in order to accurately model the hydrodynamic behaviour of the floating pressure plate according to the Reynold's equation. This allows for calculation of the total leakages from each control volume, which are communicated back to the main solver.

The total load on the gears is of interest for noise since this force is transmitted to the pump body through the shaft journal bearings. The total force on the gears is the sum of all forces in x and y directions due to pressure as calculated by

$$F_{p,x}(\vartheta) = \sum_{i=1}^{z}\sum_{k=1}^{Ns} f_{x,i,k}(\vartheta) \quad where\ Ns = 1\ or\ 3 \tag{2.4}$$

$$F_{p,y}(\vartheta) = \sum_{i=1}^{z}\sum_{k=1}^{Ns} f_{y,i,k}(\vartheta) \quad where\ Ns = 1\ or\ 3. \tag{2.5}$$

The caluculation of force areas is shown in Figure 2.5.

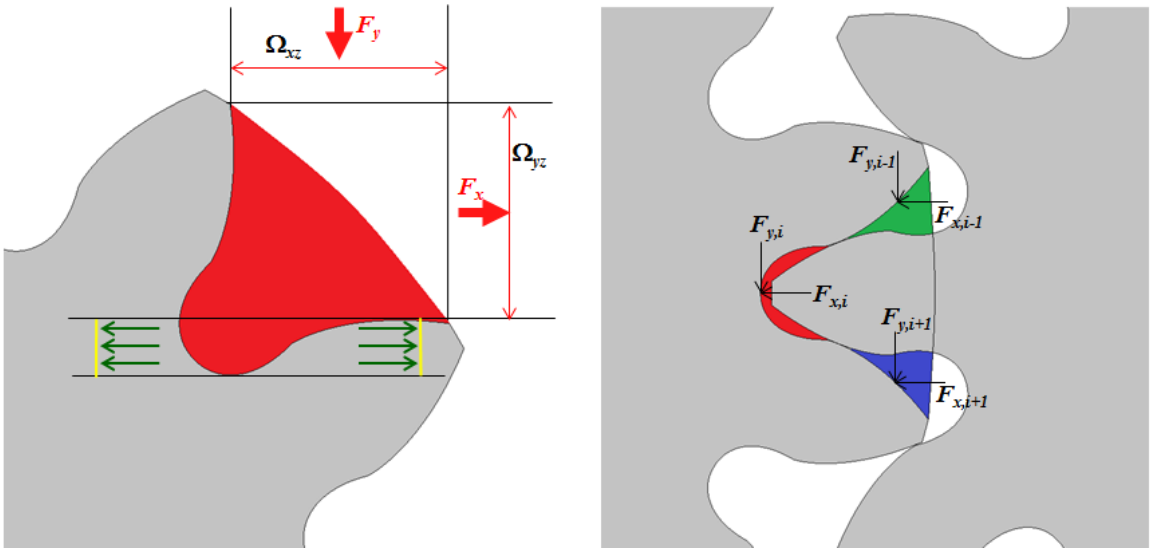

Figure 2.5: Forces on gear due to modeled fluid pressure in each TSV.

The total net force on the gear due to the pressure in each TSV during operation must be reacted by the force carried in the journal bearing.

2.3 Model Results

An example input and output of HYGESim is shown in Figure 2.6. The right side scale and blue line shows a single TSV around a full revolution. A single TSV is at full volume for approximately 270° of the gear rotation, and decreases down to a minima at the center of the meshing zone. The resulting pressure in that TSV is generated from an orifice load and is shown by the left side scale and the red line. Several sources of predicted noise are also shown in the pressure in Figure 2.6 as described previously. The figure shows the rate at which the fluid pressurizes and decompresses. Also, the pressure peak at around 350° is caused by the trapped volume in the meshing zone. Since the TSV is not connected to either the HP or LP ports at that time while the volume is also decreasing, pressure

overshoot occurs in that volume. Likewise, from 355° through 10°, the pressure in the TSV can fall below atmospheric due to the increasing volume of the trapped TSV.

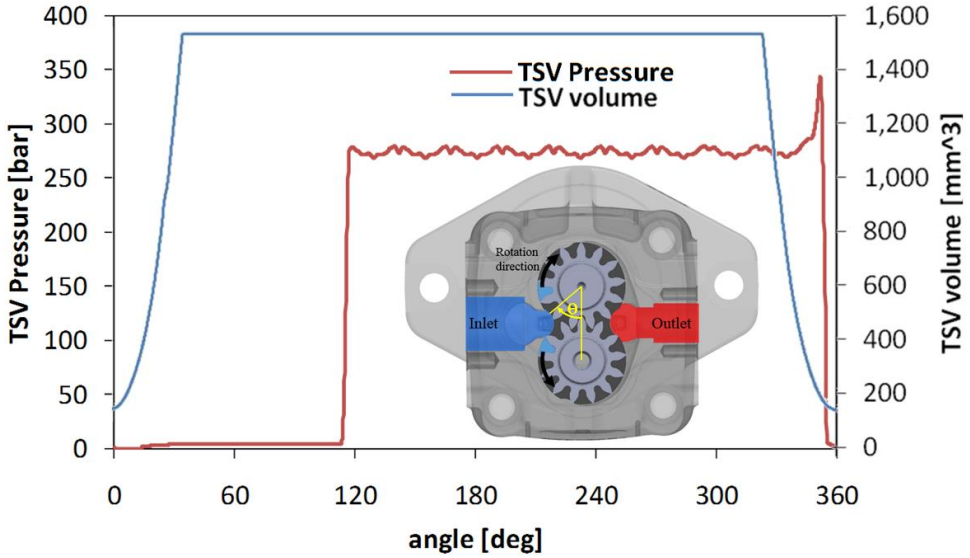

Figure 2.6: Pressure distribution in a TSV around one revolution.

When the TSV is connected to the outlet HP port via a specially machined groove typically on the lateral pressure plate, the pressure rapidly rises in the chamber to near the outlet pressure. Additionally, the outlet pressure ripple can be observed and compared to experiments as shown in Figure 2.7.

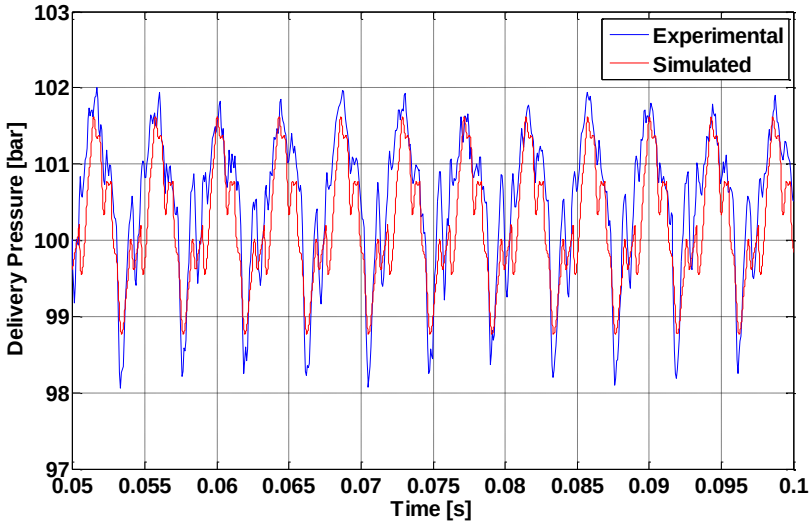

Figure 2.7: Filtered experimental and simulated data for outlet pressure ripple.

The HYGESim model can be used with a variety of different lines and loads to compare to physical hydraulic systems as shown in Figure 2.8.

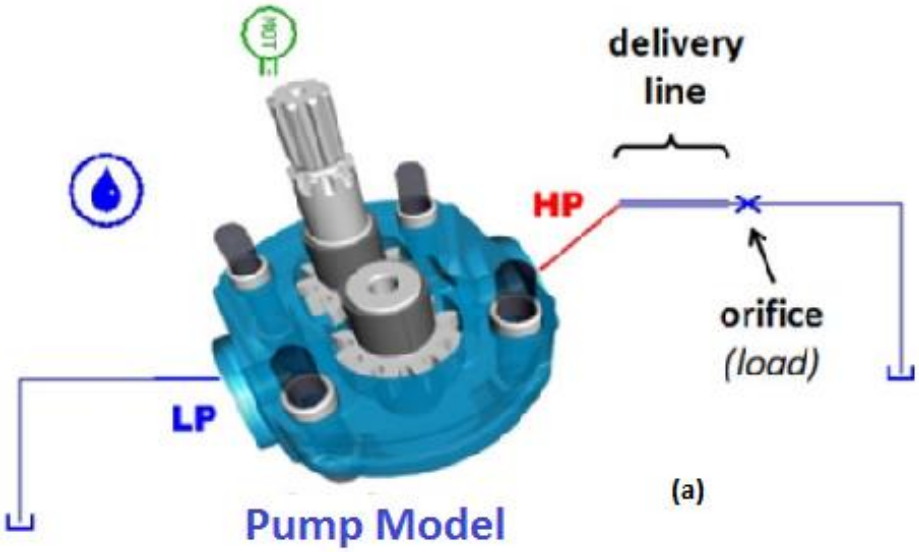

Figure 2.8: HYGESim in an example system.

This allows for many applications of the model under different load conditions and different attached systems.

2.4 Model of Hydraulic Lines

Modeling line contributions to noise is important since the lines provide a key path for noise to propagate from the sources out into the environment. The geometry and dynamics of the lines and the load can play an important role in how the forces and pressures are applied to the interior of the lines, and also the subsequent propagation through the walls of the lines and out to the environment. The effects of the hydraulic lines are present for every hydraulic system. The goal of modeling the noise propagation through the hydraulic lines is to characterize the effect on noise that a basic hydraulic line causes and to determine how to design better systems.

The relevant base speeds of free wave propagation are shown in Table 2.3. The speeds in fluids were calculated according to:

$$c = \sqrt{\frac{K}{\rho}} \tag{2.6}$$

K is the bulk modulus and ρ is the fluid density. For ISO 46 oil at 50ºC and 250 bar, c=1474 m/s.

Table 2.3 Speed of wave propagation in relevant mediums

Medium	**Free wave propagation speed [m/s]**
Oil	1474
Steel	6000
Braided rubber hose	900-1150 (Klop 2010)
Air	343

Understanding the propagation of noise from the internal sources out to the surrounds requires an understanding of how the waves travel through each media.

The hydraulic line model is based on a distributed one dimensional line with lumped elements. This model takes into account frequency dependent friction and flexure of the line walls, which allows for determining source terms for acoustic excitation and radiation. The 1D model assumes a high length to diameter ratio of the line such that the pressure is assumed to be homogenous through the cross section of the pipe and varies only along the length. Considering the fidelity of the line model is an important detail that greatly affects the simulation results. If too few nodes along the pipe length are considered, a poor approximation of the loading conditions is provided. If too many elements are added, the effective stiffness of the fluid exceeds the true behavior and results in amplification of higher order frequencies due to an increased number of potential fluid harmonics.

According to lumped parameter models there is a limit to the number lumped masses for a given volume based on its geometry. A simplified spring-mass-damper simplification to explain the physics of the distributed line model is shown in the following figures. The distributed line model contributes to frequency content because of added stiffness. An example single degree of freedom system is shown in Figure 2.9.

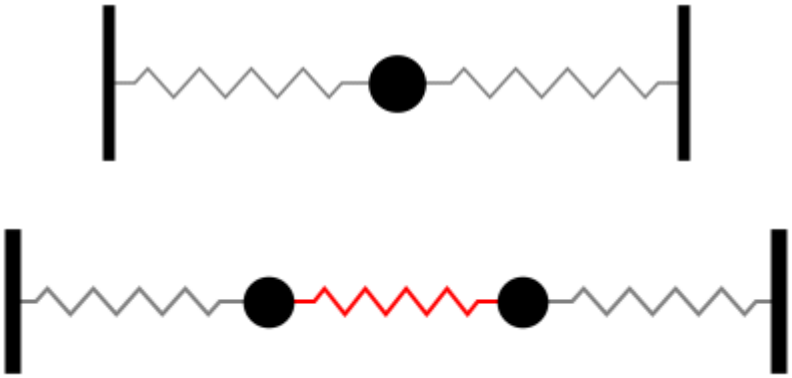

Figure 2.9 One and two degree of freedom systems.

With a single mass, and two equal springs representing the fluid stiffness, then the fluid harmonic frequencies occur at multiples of $\omega=(2s/m)^{1/2}$.With two equal masses such that $M_1+M_2=M$ with the same total mass. Two masses and 3 equal springs the resonance can occur at two frequencies, $\omega_1=(2s/m)^{1/2}$ and $\omega_2=(3s/m)^{1/2}$. The estimated modal resonant frequencies of simplified system are shown in Figure 2.10.

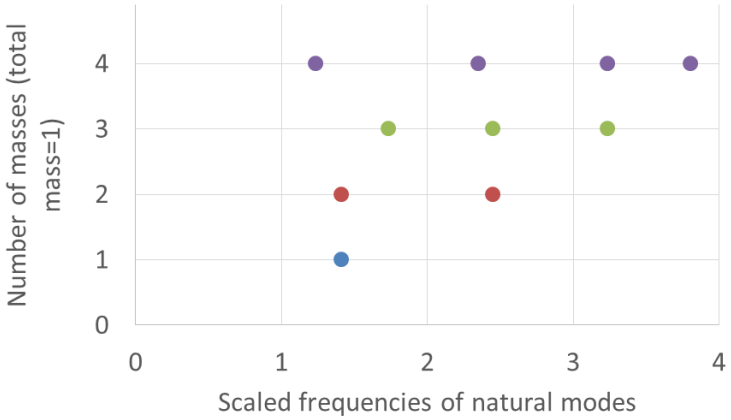

Figure 2.10 Example modal frequencies based on simple system

More nodes results in two changes in the system, more total stiffness (total mass is constant) means higher frequencies, and more modal frequencies in all frequency ranges. This contributes to the consideration for the harmonic frequencies of the oil in the pipe. Similar to many instruments, the fluid inside a cylindrical shell acts in a harmonic way according to the geometry of the cavity and the properties of the fluid. This dominates when the system does not have a strong forced excitation at certain frequencies, and may amplify existing frequencies in the system.

Basic equations for fluid motion inside a cylindrical shell can be derived from the geometry by making simplifying assumptions. An example simplified diagram of the fluid behavior in the steel pipe where the pump has been replaced by a single oscillating piston, and the load orifice is represented by a simple mechanical impedance as shown in Figure 2.11.

Figure 2.11 Simplified pipe model for fluid harmonic study

The fluid harmonic behavior can be modelled as forward and backward travelling plane waves from left to right in the diagram.

$$p = Ae^{j[\omega t + k(L-x)]} + Be^{j[\omega t - k(L-x)]} \tag{2.7}$$

By assuming different end conditions, one can approximate harmonics of the fluid analytically as shown by McKee et al. (2009).

Rigid end cap at right:

$$f = \frac{nc}{4(L + 0.4d)} \qquad \text{n=1,3,5…} \tag{2.8}$$

Open pipe at right:

$$f = \frac{nc}{2(L + 0.3d)} \qquad \text{n=1,2,3…} \tag{2.9}$$

Harmonic frequencies of the fluid based on the geometry of the pipe and the fluid properties. Harmonics take the form of standing waves in the pipe at different frequencies if the excitation is not being forced to specific frequencies. The fluid harmonic behavior in the test setup pipe is between the two extreme values based on the mechanical impedance of the orifice plate. The harmonics couple to the excitation frequencies when under a forced excitation similar to the oscillation of flow introduced by the pump since they are in a similar frequency range. This results in the observed fluid behavior in simulation and practice.

The analytical fluid harmonics estimate take the shape of sine and cosine waves in the fluid pressure. The frequencies that these shapes occur at are shown in Table 2.4 for two different end conditions.

Table 2.4 Analytical wave modal frequencies.

closed pipe (Hz)	open pipe (Hz)
365	731
1094	1463
1824	2194
2554	2926
3283	3657
4013	4389
4742	5120
5472	5851
6201	6583
6931	7314
7661	8046
8390	8777
9120	9509
9849	10240
10579	10971

The actual fluid model implemented uses lumped fluid elements, where L is the total line length and V is the total line volume. The pressure derivatives are calculated at the nodes and at the ports of the model with the formula:

$$\frac{\partial Q}{\partial t} = \frac{A}{\rho}\frac{\partial P}{\partial x} - v \cdot \frac{\partial Q}{\partial x} - \frac{ff \cdot Q^2 \cdot sign(Q)}{2 \cdot D \cdot A} \tag{2.10}$$

Which is dependent on the pipe properties of the cross-sectional area of the pipe A, and the friction factor ff according to Binder (1956).

Now, applying this to the pump model to while comparing results from number of nodes in the outlet line with 1000rpm operation in Figure 2.12 shows the coupling between the excitation pressure frequencies with the harmonic frequencies of the fluid in the pipe.

Five nodes is the suggested number according to the length to diameter ratio of the line. This number of nodes also allows for the best validation of the pressure ripple shown in the following section. The frequency spectra derived from a Fast Fourier Transform (FFT) is also shown.

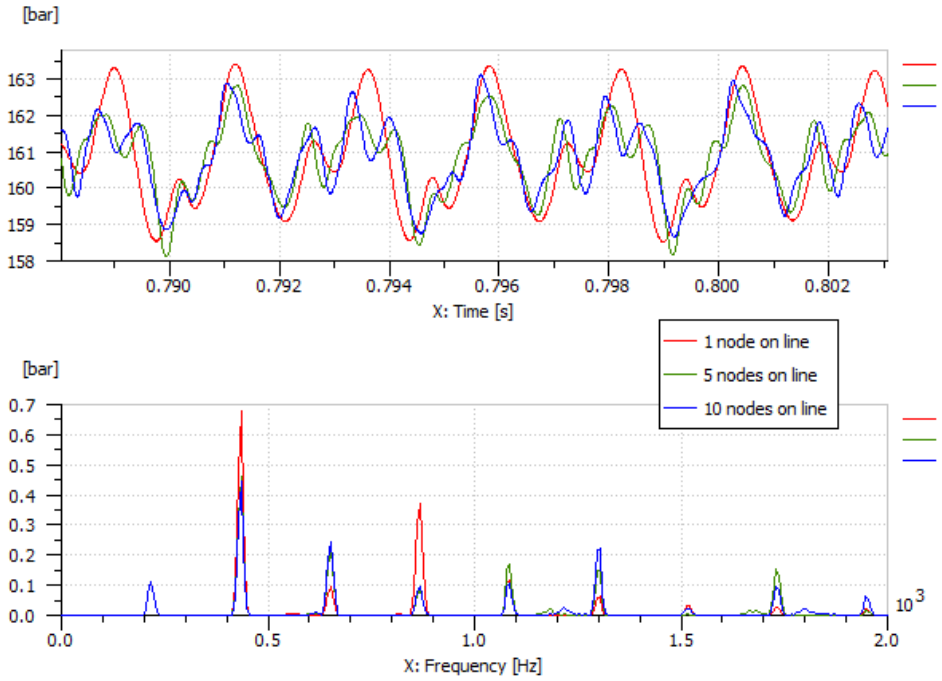

Figure 2.12 Outlet pressure ripple and FFT with varying number of nodes

The higher frequencies of pressure ripple are emphasized for more nodes which depends on the way to apply the load as discrete functions. The pressure at all five nodes considered is shown in Figure 2.13.

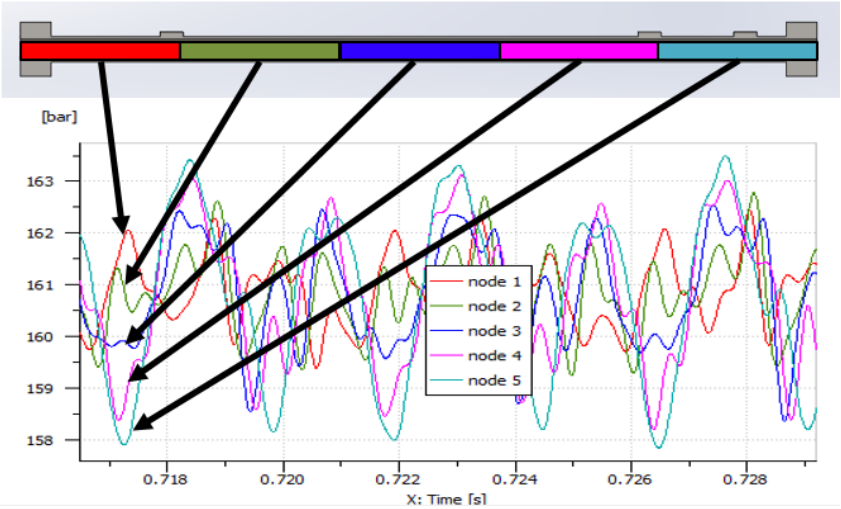

Figure 2.13 Pressure functions at five nodes in the pipe.

Considering pressures at 10 nodes as a surface in order to better visualize the pressure field as shown in Figure 2.14 and Figure 2.15.

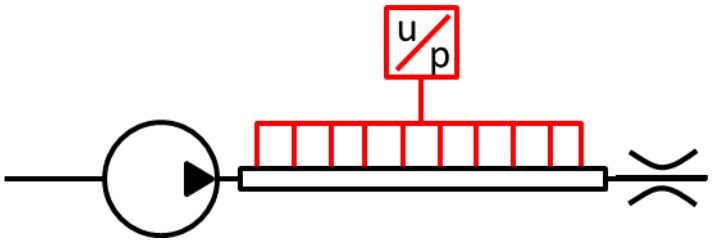

Figure 2.14 Pressure sensor locations for modeled result.

The large number of fluid nodes considers does limit the accuracy of the predicted magnitudes of the pressure waves. However, it is very useful for the sake of visualization and understanding of how the waves propagate in the pipe fluid volume.

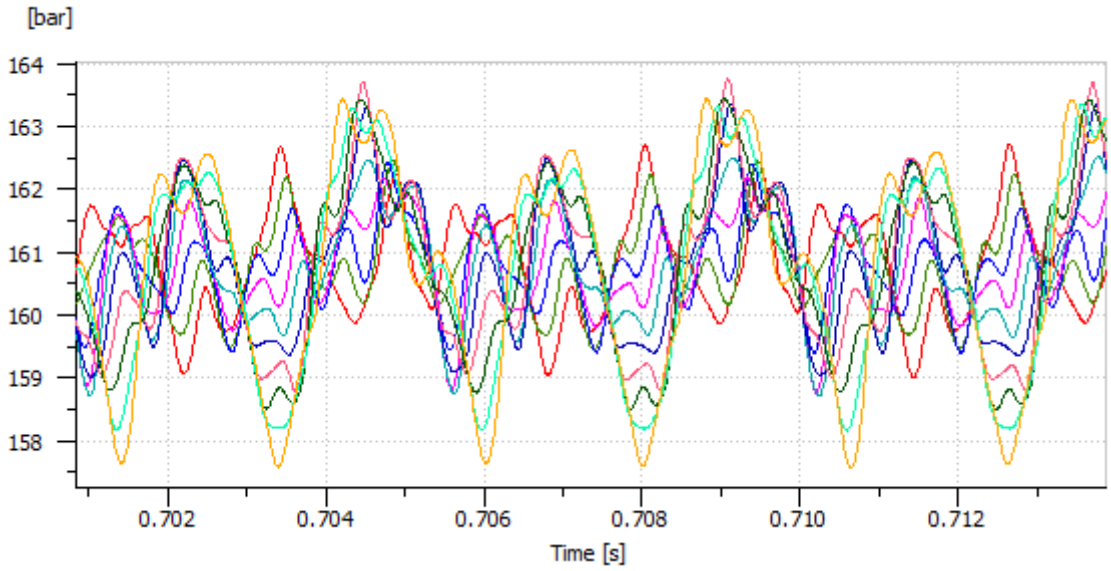

Figure 2.15 Pressure at 10 nodes in the pipe.

The modeled line pressure ripple at 1000rpm as shown above was then turned into a surface with time, length, and pressure as the axes shown in Figure 2.16.

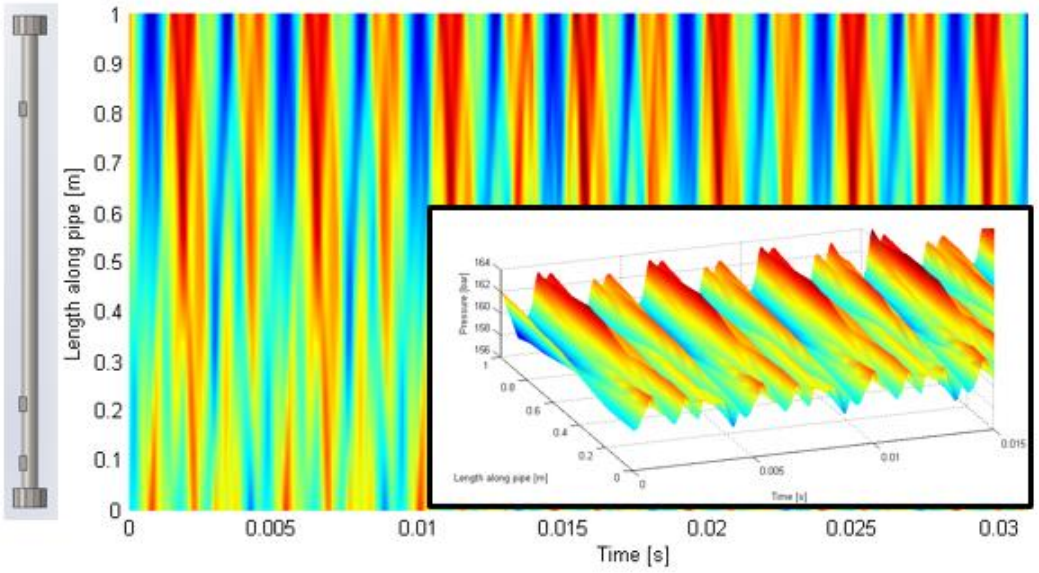

Figure 2.16 Pressure in the pipe

The fluid pressure oscillates from one end of the pipe to the other in a strong coupling between the fluid harmonics and the forcing frequencies.

In order to model line contributions to noise, a better understanding of the fluid harmonics in the pipe is needed. This then couples to the structure and the air. The free wave propagation speed in different materials is shown below.

Pressure is pulsing back and forth in the 1m pipe with a node at center point of pipe (0.5m). This behavior dominates performance, out of phase by 180 degrees at opposite ends as shown in the magnitude of the frequency spectra of the pressure ripple in Figure 2.17.

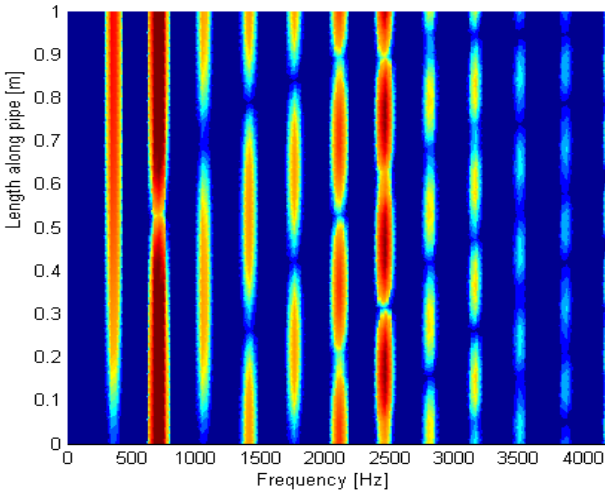

Figure 2.17 Frequency spectra magnitude.

Now instead of considering the pressure field across the length of the pipe, the knowledge gained in modeling the line leads the conclusion that an effect should be seen in the pressure ripple where there is an interaction between the harmonics of the fluid and the excitation frequencies of the pump. Consider a single pressure location at the outlet of the pump as shown in Figure 2.18.

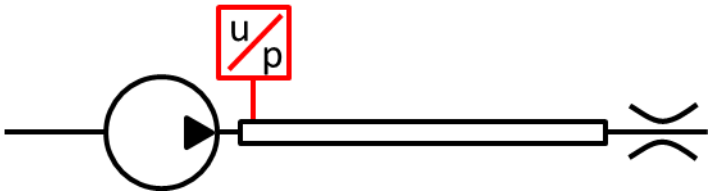

Figure 2.18 Single pressure sensor location at pump outlet.

If excitation frequencies align with harmonic frequencies of the fluid in the pipe, large outputs can occur in the line pressures. Such as around 650 Hz, which corresponds well with the analytical values calculated previously. This result is shown in Figure 2.19 in the highlighted bands around 700 and 1400 Hz in the frequency spectra, the pressure

ripple outputs are interacting with the harmonics of the line at each different speed, which results in a larger output. The outlet pressure for a range of pump shaft speeds is shown, and the harmonic behavior of the fluid is visible in the heavier bands.

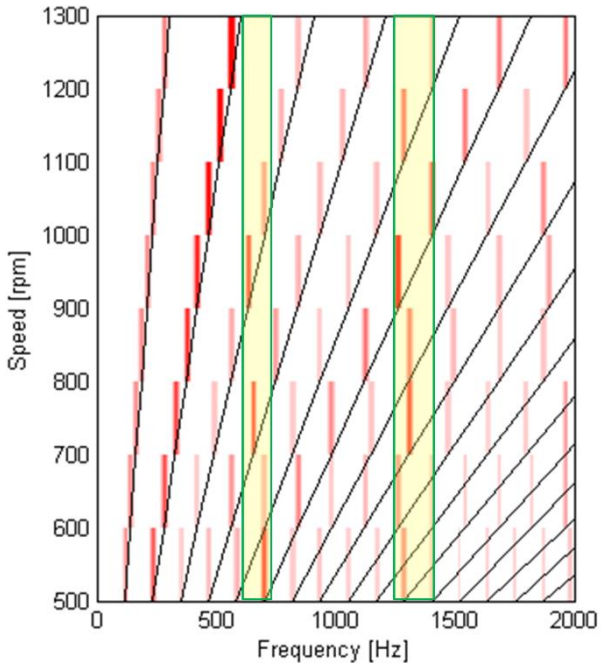

Figure 2.19 Simulated pressure spectra under varied speeds

The interaction between the fluid harmonics and the shape of the pipe has a large impact on the fluid behavior inside the pipe volume. If the forcing frequencies of the pump change (due to change in speed or number of pumping chambers), or if the harmonics of the fluid volume change (due to adjusting the pipe length or diameter or load impedance), then the coupled results will also be different. This makes for a very complicated problem, but understanding the interactions is a good step towards improving the system noise performance.

2.5 Model-based Design of External Gear Pumps

Model based analysis of EGPs allows for design of new units with unique fluid porting and volume variation. This is primarily done in EGPs through design of lateral pressure plates with porting grooves built in. A primary hypothesis in the creation of quieter hydraulic systems is the reduction of the FBN through the reduction of pressure ripples in the lines. Ways to achieve this reduction were discussed in the literature review. Several

new designs for low pressure ripple and high efficiency were proposed for the lateral pressure plates of the reference gear pump #2 by Devendran (2012) using a genetic algorithm based in Mode Frontier coupled with the HYGESim lumped parameter model. The design allow for small changes to be made to the LP and HP grooves on the lateral plates which improve the performance of the reference pump without increasing the complexity of the machine or adding components. The objective functions considered are to minimize pressure ripple, minimize pressure peak, minimize localized cavitation, and maximize volumetric efficiency. The pressure ripple is determined by summing the energy of the ripple frequency spectra in bands. The pressure peak in the TSV pressure that occurs in the trapped volume in the meshing zone. Local cavitation is the drop below ambient pressure. Volumetric efficiency is characterized by the provided flow rate with respect to the pump speed and geometric displacement.

An optimized design of the lateral plates was selected according to the above parameters and optimization routine in order to be tested alongside the Reference Pump #2. This design will be referred to as prototype 12, and it was designed with minimized outlet pressure ripple in order to test the influence on noise.

2.6 Experimental Validation

The HYGESim model was validated previously by Vacca (2011) with measurements of both the TSV chamber pressure as well as the outlet pressure and flow. A new unit under consideration for the present work contains different features for consideration and the understanding of the performance of the unit is improved by a new validation. The validation of the pump performance is important to the overall noise research due to the use of the pump model as a load function for the acoustic model. Understanding the noise generation and propagation begins with the internal loads, and experience gained through measuring the FBN experimentally is useful for guiding the later stages of modeling and experiments. An additional validation of the pump model was completed with respect to the mean measured flow rates in comparison to simulated data.

2.6.1 Pressure ripple measurements

The main characteristics of interest in comparing HYGESim predictions to experimental values are to consider the total flow rate and the ripple in the pressure caused by flow ripples under a load condition. The test rig setup was realized on the Multi-Purpose Test Rig (MPTR). The schematic of the test setup is shown in Figure 2.20.

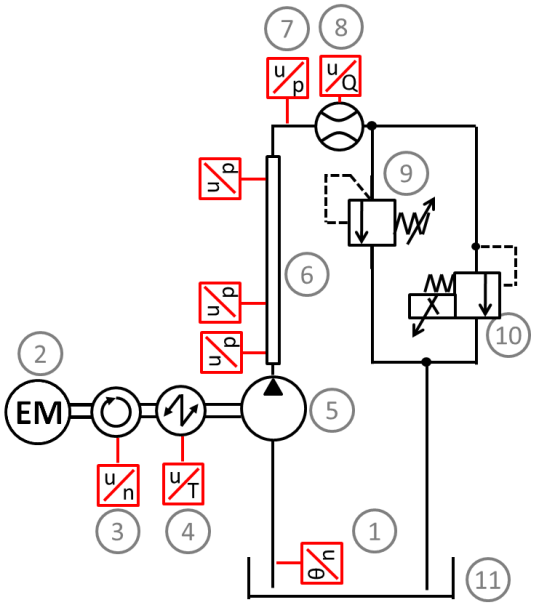

Figure 2.20: Pressure ripple measurement test rig layout.

The test pump is driven by an electric motor and a load is applied by use of a fixed orifice plate at the end of a steel pipe and also a proportional valve controlled by the data acquisition software. The steel pipe is the same as used by Klop (2008) and allows for precise measurement of the pressure ripple cause by the displacing action due to the fast response of the sensors. The rigid pipe and fixed orifice are more accurate to model than other line types and the pipe also tends to amplify the frequencies of the pressure ripple which allows for a more detailed comparison. The descriptions of individual components are shown in Table 2.5.

Table 2.5: Description of test rig components.

#	Description	Details
1	Inlet temperature sensor	Omega K-type resistive thermocouple, range 0-120° C, accuracy 1% FS
2	Electric motor	ABB, 93 kW, range 4000 rpm
3	Shaft speed sensor	HBM 10F/FS, not used in experiments
4	Shaft torque sensor	HBM 10F/FS, not used in experiments
5	Test pump	External gear pump Reference Pump #2
6	Calibrated steel pipe with embedded pressure sensors	Kistler 603B1 piezoelectric, 0-1000 bar, accuracy 1.1% FS, sensors located at 230mm, 350mm, and 950mm from outlet port including fittings.
7	Line pressure sensor	WIKA, 0-400 bar, accuracy 0.25% FS
8	Flow meter	VS 4 by VSE, gear type, 0-400 L/min, accuracy 1% FS
9	Pressure relief valve	300 bar safety setting.
10	Proportional valve	Hydraforce TS10-26A-8T-N-12DR proportional orifice
11	Oil tank	SAE 46 oil

The calibrated pipe used in the experiments is shown in Figure 2.21. The pipe is one meter in length and has a constant inner diameter of 25.4 mm. More details are described in Table 2.5.

Figure 2.21: Calibrated steel pipe with embedded sensors.

The results from the pressure ripple experiments will be compared in the following section to the simulated pump for the purpose of validation.

2.6.2 Frequency analysis of loading pressure

The primary frequencies in Hz in the simulated and measured data are at

$$f_1 = \frac{nc \cdot n}{60}. \tag{2.11}$$

Where n is the speed of the pump and 14 is the number of discrete pumping volumes. There are 14 discrete volumes on each gear, however, in the meshing action, a pair of volumes one on each gear act together as a single pumping volume when gears with single flank contact are used as in the reference pump. For example, at 1000rpm, f_1 occurs at 233Hz and the subsequent integer multiples of this frequency compose most of the energy in the frequency at frequencies in this range. There are additional peaks at multiples of the shaft frequency

$$r_1 = \frac{n}{60}. \tag{2.12}$$

A Butterworth filter was created to achieve the band pass effect and to remove low frequency noise from shaft oscillations that are not predicted by HYGESim. The band pass filter is from 100 to 5000Hz. Notice that this does not remove all of the shaft oscillation frequency. The first three main peaks in the unfiltered data are at approximately 16.7Hz, 33.3Hz, and 50Hz. The sum of the first pump frequency f_1 and the third multiple r_3 of the shaft oscillation creates a new peak inside of the filter band of interest that will be present in the experimental data but not the simulations as shown in Figure 2.22 at approximately 290Hz. The low frequency content is created by small eccentricities caused by the shaft coupling. Note that for frequencies above 100 Hz, the filtered and unfiltered data lie on top of each other.

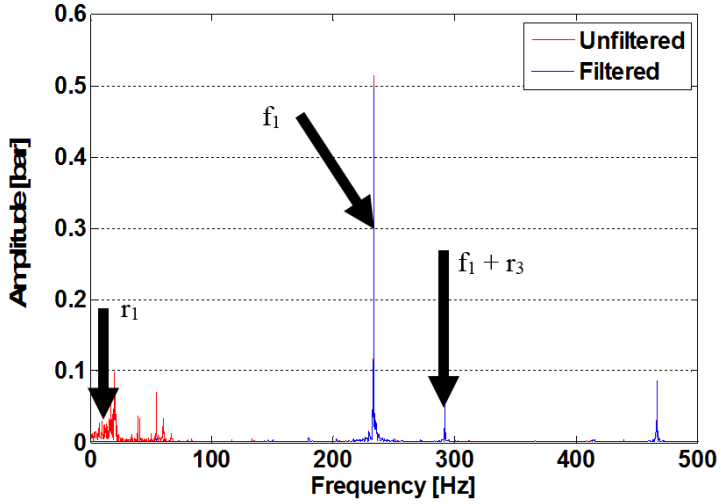

Figure 2.22: Filtering out of low frequency noise for comparison of results.

While the unfiltered data contains the trend of a sinusoidal oscillation of the moving average at 16.6Hz, the filtered data has a constant trend at as shown in Figure 2.23. The cause of the 16.6Hz oscillation is due mainly to eccentricity of the coupling between the electric motor and the pump.

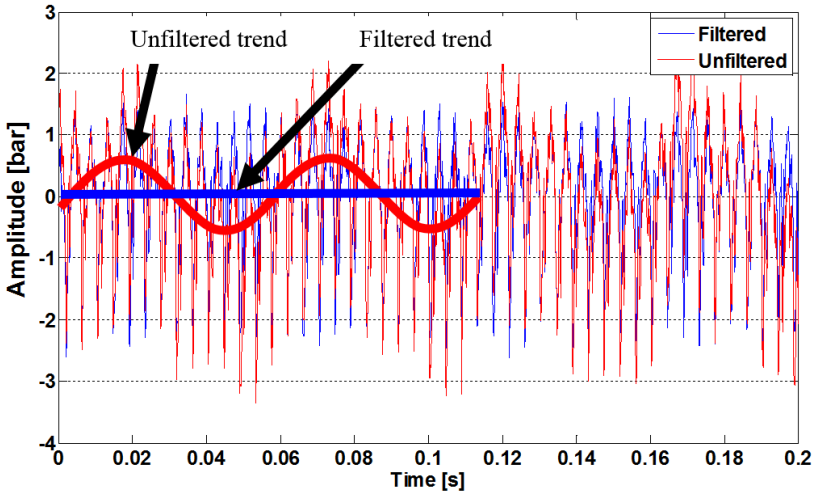

Figure 2.23: Comparison of filtered and unfiltered data.

When the shaft oscillation is removed, the comparison to the simulated data is excellent in the time and frequency domains. However the lack of shaft frequency in the simulated data is a limitation of the model when it comes to predicting the shaft frequency as a source of noise. This source is heavily dependent on the particular experimental setup

including possible eccentricities between the primary mover and the pump. The main features of the pressure ripple are captured by the model. This includes the mean value as well as the amplitude of the major sinusoidal components as shown in Figure 2.24.

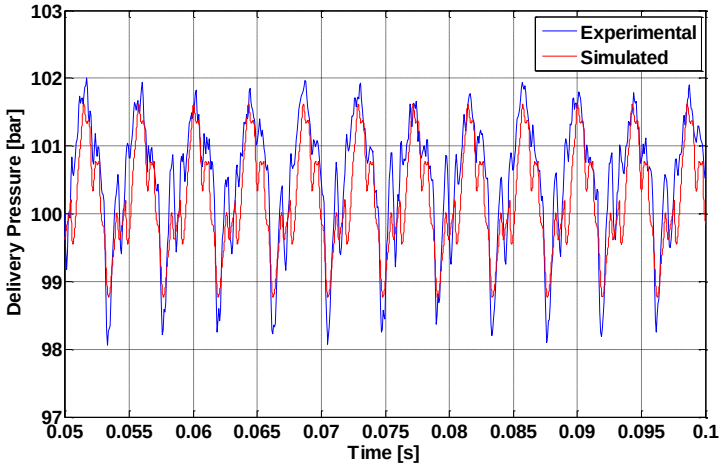

Figure 2.24: Filtered experimental and simulated data for outlet pressure ripple.

The Fourier spectra of the simulated and experimental pressure ripple are shown in Figure 2.25. The amplitude of the primary peaks is captured to a very accurate degree and this is a validation of the HYGESim model for Reference Pump #2. The spectra shows that as predicted, the pressure ripple at the pump outlet (which is connected to much of the interior of the pump casing by the high-speed groove) is highly oscillatory with the majority of the energy focused on multiples of the primary pump fundamental frequency f_1 which is created by the number of TSVs and the shaft speed of rotation.

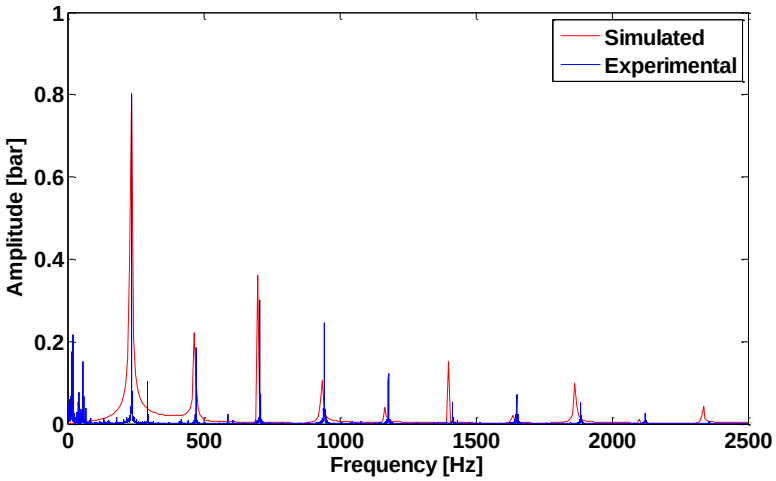

Figure 2.25: Frequency spectra of experimental and simulated data.

A linear display of the frequency spectra was shown here and will be repeated throughout the current studies in order to emphasize the peak values dominating the measured and simulated behavior of the system. While a logarithmic scale is often used in acoustic studies in order to better correlate with the dynamic hearing range of the human ear.

The accurate pressure prediction and pump model forms the basis of the noise model of internal sources. If the FBN and the other internal phenomena of the pump can be predicted, then an accurate acoustic model can be built on top of the model of internal sources.

3. ACOUSTIC MODEL FOR PUMP NOISE RADIATION

From the background shown in previous sections, the need for an acoustic model directly predicting the sound radiation from displacement machines was shown. The pump output in the lines and inside the case of the units themselves is dominated by the flow ripples caused during the displacing action. This chapter will explain the acoustic model built as a primary part of the research activity. This begins with a an overview of the assumptions made in modeling the pump, the theoretical basis for the model, an overview of the model layout, and a discussion of the results.

3.1 Acoustic Model Methodology

A vibro-acoustic model was developed using a combined Finite Element Method (FEM) and Boundary Element Method (BEM) approach. The FEM/BEM approach was chosen due to its efficiency and accuracy in predicting the ABN. In order to fully model the loading forces, the structure response, and the transmission to the air, a model is needed for each. The HYGESim model provides the loading forces. FEM models are widely accepted for the structural vibration, and BEM is accepted as the best for modeling the near-field acoustic effects in models that are placed in unbounded environments, for example, outdoors or in anechoic spaces. BEM is chosen because the fluid-structure coupling interaction between the radiated air pressure and the structure vibrations can be neglected due to the differences in stiffness and density as described by Sandberg (2009) Another simplification is the effect of the of the internal pump components such as the gears and the lateral plates in that they are included only the generation of the loading conditions, but not in the current acoustic propagation model. In the current model, the interaction of the structural components of the main body is considered through the fluid

separating the internal components from the case. The BEM wrapper mesh technique is used for calculation of the transmission of sound from the pump surface mesh out to the field. The model type considers the interaction of the load conditions with the mode shapes of the structure. The main structure is adapted from the BEM acoustics methodology for Virtual.Lab Acoustics and suggested by Desmet et al. (2012)

The additional information that is needed is the specification of the acoustic environment for the EGP. The basic inputs for the acoustic simulation are the pump model results delivered from the fluid dynamic model along with the environment information. Processing the fluid dynamic model results involves selecting load and surfaces and mapping loads onto the correct nodes of a structural Finite Element Method (FEM) mesh. The simulation results are solved for in LMS Virtual.Lab Acoustic.

A summary of the acoustic model is shown in Figure 3.1. This is an extension of the HYGESim model for the purpose of predicting sound radiation from the pump body.

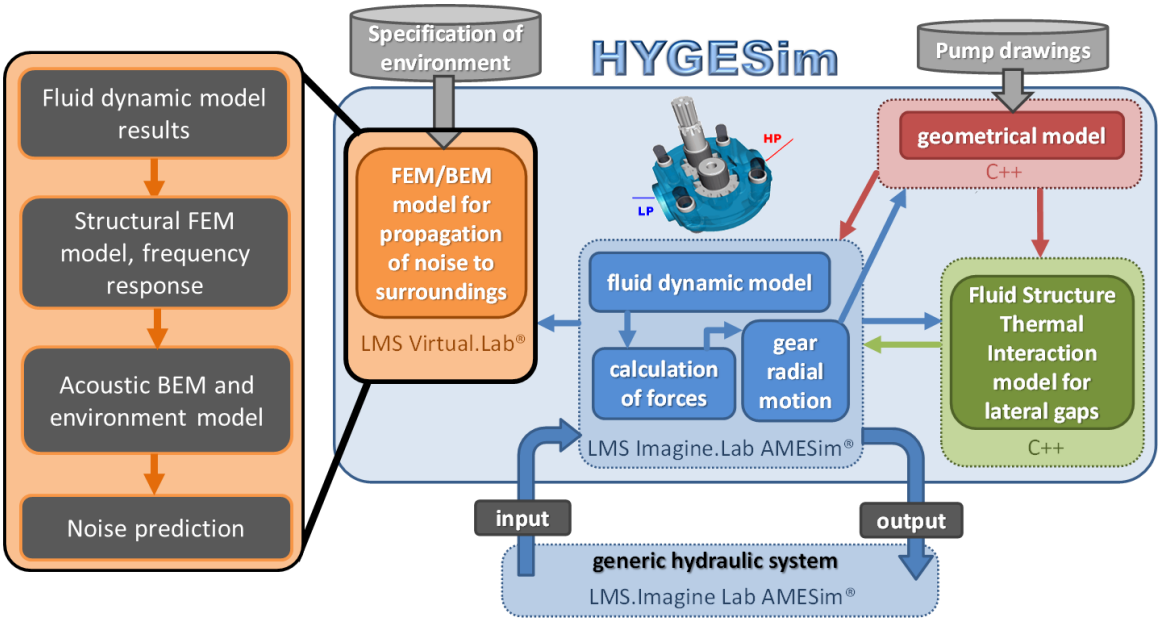

Figure 3.1: HYGESim model schematic including coupled acoustic model.

The predicted forces and pressures in the form of functions of frequency from the HYGESim model are used as loading functions since frequency loading allows a good estimation of the applied load without needing to perform long time-transient computations in the BEM solver. Potential areas of interest to noise that are considered in the HYGESim model were discussed previously and they include inlet and outlet dynamic pressure,

chamber pressurization phenomena, and bearing forces are considered in the ABN evaluation for radiation from the pump body. The acoustic model makes some key assumptions with respect to the input sources of FBN. The Fast Fourier Transform (FFT) is used to compute the frequency spectra of the loading forces. In EGPs, there are no mechanical parts directly in contact with and exciting the pump structure except through fluid boundaries. By comparison, the swash plate control in axial-piston type units can have a strong impact on the radiated noise. While in the EGP, all noise passing to the pump housing passes through the fluid in the pumping chambers, the ports, or the fluid bearings inside the unit. The force loads on the structure then propagate to the air-borne noise (ABN) which is what is heard and measured at the field points as shown in Figure 3.2.

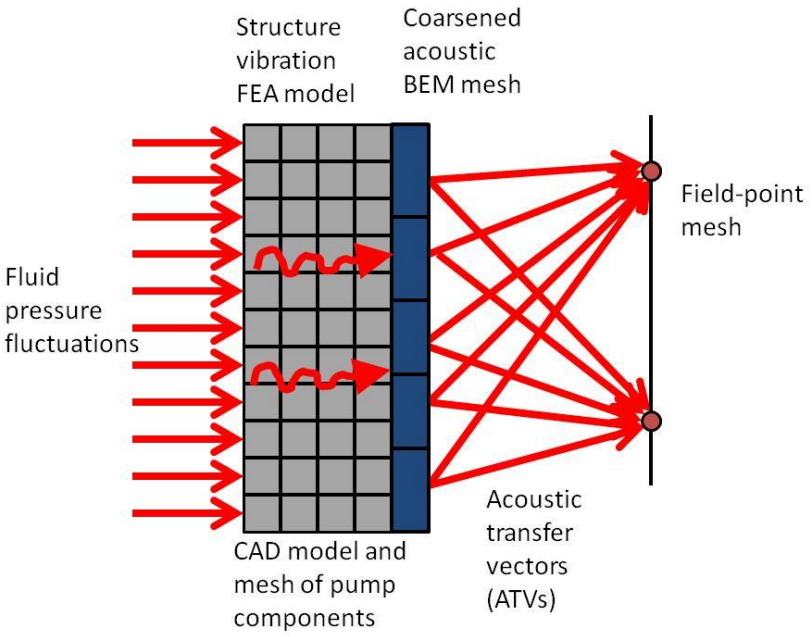

Figure 3.2: Transmission of sound from working fluid to field points.

The equations put into practice in the model are described in detail by Desmet et al (2012) and published by Opperwall (2012). The primary governing equation for the steady-state acoustic pressure is the second-order Helmholtz equation given by

$$\nabla^2 p(x,y,z) + k^2 p(x,y,z) = -j\rho_0 \omega q(x,y,z). \tag{3.1}$$

Where p is the pressure at any node and q is the excitation.

The structural dynamics are described by Hooke's Law where:

$$([K_s] + j\omega[C_s] - \omega^2[M_s])\{w_i\} = \{F_s\}. \tag{3.2}$$

Here, $[K_s]$ is the stiffness matrix, $[C_s]$ is the damping matrix, $[M_s]$ is the mass matrix, and $\{F_s\}$ is the boundary conditions set.

The structural finite element model is shown by:

$$\begin{Bmatrix} \widehat{w}_x(x,y,z) \\ \widehat{w}_y(x,y,z) \\ \widehat{w}_z(x,y,z) \end{Bmatrix} = [N_s]\{w_i\} + [N_w]\{\overline{w}_i\} \tag{3.3}$$

Where $[N_s]$ and $[N_w]$ are the global shape functions for the unconstrained and constrained translational and rotational degrees of freedom on the body. The w and its subscripts refer to the translational and rotational displacements of the corresponding nodes.

The acoustic boundary element approximations for steady state pressure and surface normal velocity are shown in:

$$\hat{p}(\vec{r}_a) = [N_a]\{\hat{p}_i\} \tag{3.4}$$

$$\hat{v}_n(\vec{r}_a) = [N_a]\{\hat{v}_{ni}\} \tag{3.5}$$

Where $\vec{r}_a$ are the surface vectors and N_a is the matrix of global shape functions which are associated with the nodes on the boundary surface.

The boundary elements of the pump consist of the external surfaces. The BEM mesh is based on an upper limiting frequency of 10000Hz where higher frequency results in a smaller wavelength and thus smaller elements are needed. A maximum frequency of 10000Hz exceeds the main excitation frequencies of the loading forces. The procedure aims to create six elements per wavelength of sound in air with 340 m/s (speed of sound in air) divided by 5000Hz for an allowed element length of up to 68mm.

By combining the structural and acoustic models, the coupled FEM/BEM equation is shown in

$$\begin{bmatrix} K_s + j\omega C_s - \omega^2 M_s & L_C & 0 \\ \rho_0 \omega^2 B_{11} T_s & A_{11} & A_{12} \\ \rho_0 \omega^2 B_{21} T_s & A_{21} & A_{22} \end{bmatrix} \begin{Bmatrix} w_i \\ \hat{p}_{i1} \\ \hat{p}_{i2} \end{Bmatrix} = \begin{Bmatrix} F_s \\ F_{a1} \\ F_{a2} \end{Bmatrix} \tag{3.6}$$

Where the A and B are terms of the nodal degrees of freedom of the acoustic model.

The interaction of the structure surface vibrations with the acoustic environment allows for the calculation of radiated sound power.

A more detailed flow chart of the model process is shown in Figure 3.3.

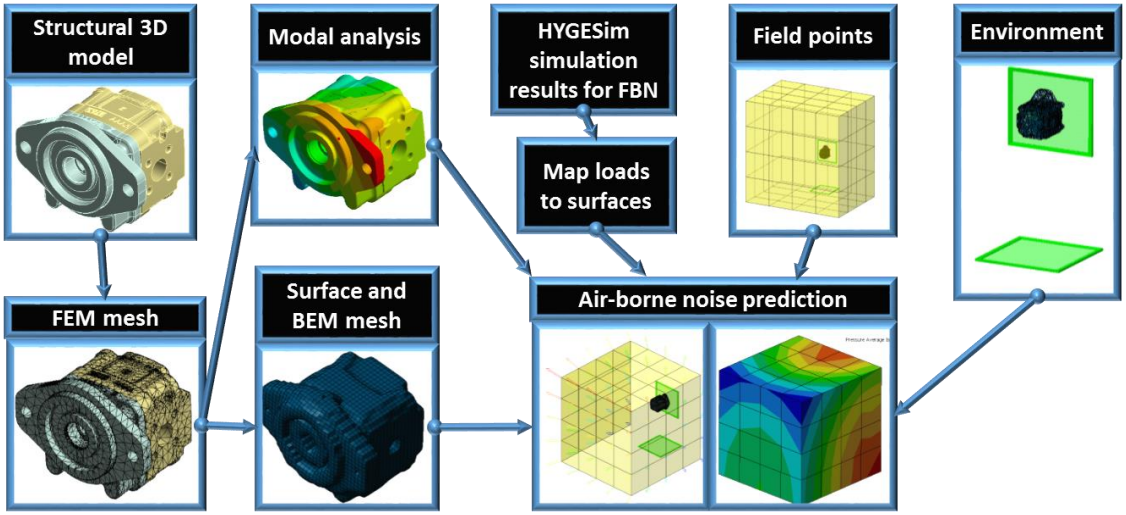

Figure 3.3: Block diagram schematic of acoustic model solving steps.

3.2 Model of Internal Noise Sources

The key physical phenomena for noise sources need to be modeled and understood in order to use them as loading conditions for an acoustic model. The basic assumption is made that all forces internal to the pump must pass through the pump casing in order to radiate out to the surroundings, or they must pass into the attached hydraulic system. This simplification neglects the influence of forces transmitting through the drive gear and coupling into the electric motor or other prime mover. The advantage of this assumption is that if the forces on the interior of the casing separating the interior moving parts from the casing can be accurately modeled, then the moving parts can be removed from the acoustic simulation and be replaced by the equivalent forcing functions. The main components are shown in Figure 3.4 for Reference Pump #1.

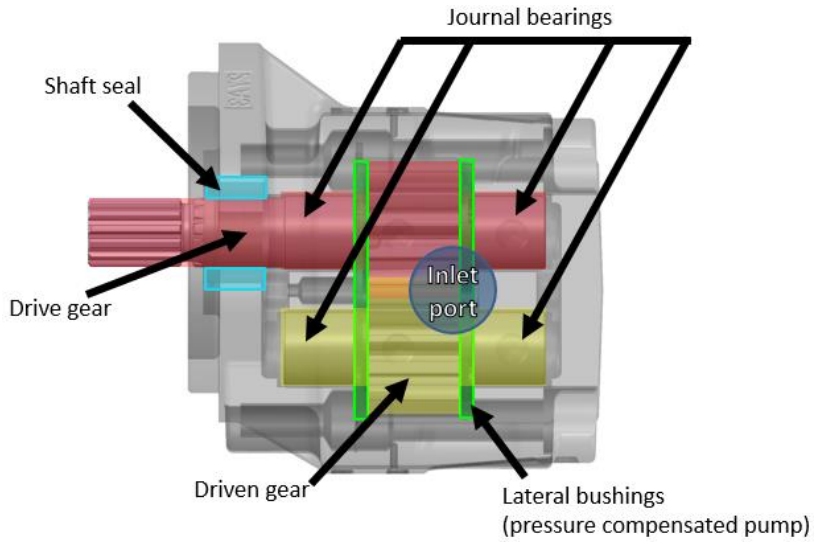

Figure 3.4 Pump geometry for acoustic simulation.

First, to account for forces on the lateral bushings, the force on the balance side of the bushing must be modeled. This is accomplished through calculating the effective area and center of force application for both the high pressure and low pressure balance areas as shown in the following figure. Note that the seal area dividing the balance side of the pressure plates is not colored red for clarity, but it is included in the high pressure area calculation.

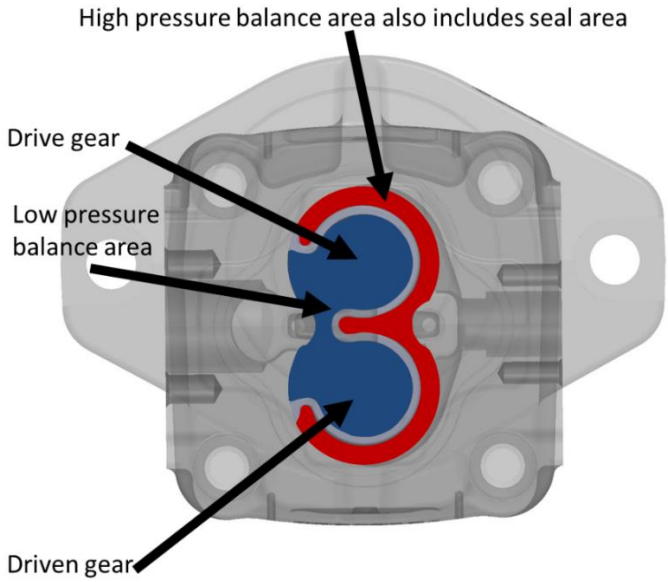

Figure 3.5 Balance areas on case side of lateral bushings.

The behavior on the balance side of the lateral bushings opposes the forces applied in the lateral gap. According to our simplifying assumption, only the forces applied on the case directly need to be considered, so the forces in the lateral gap are only considered based on the effect they have on the balance area forces. The full areas of application for the high and low pressure are shown in profile view in Figure 3.6.

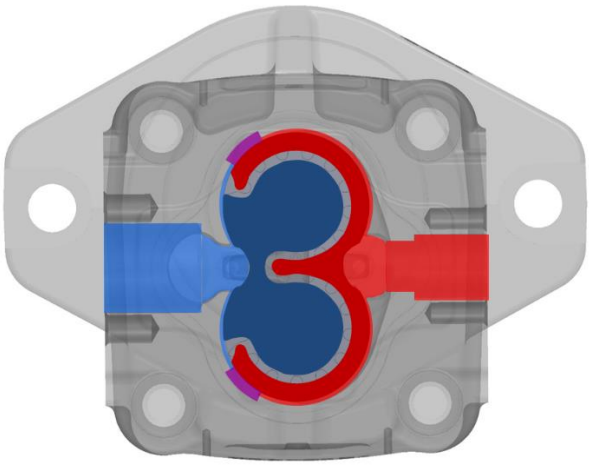

Figure 3.6 Load areas for high and low pressure.

The areas of case contact with the outlet pressure are shown in red and occur at the outlet port, around case radius of the gears according to the backflow (high-speed) groove, and the high pressure balance area on lateral bushing. This load pressure is shown in the following figures along with the frequency spectra which is computed to use as a forcing function. Pressures were converted to a total dynamic force by the total area of application derived from the pump physical geometry. The inlet pressure ripple area of application is also shown in Figure 3.6 in blue. This again includes the port area, the case around the gear, and the balance area around the lateral pressure plate and journal bearing.

A summary of the force locations for one half of the pump is shown in Figure 3.7. In particular, the inlet load is shown in blue, the outlet load in red, four different transition region vectors in purple, and the journal bearing load in black. One of the main topics of study in previous optimization efforts is the pressure peak and depressurization in the meshing region. However, in order for the forces to propagate out of the body of the pump they must transmit either through the gears and into the journal bearings, or into the lateral pressure plates which are balanced with fluid pressure. Since the journal bearings and

lateral plate balance pressures are considered in the acoustic model, the pressurization in the TSV during meshing is already accounted for as long as the floating bearing assumption holds.

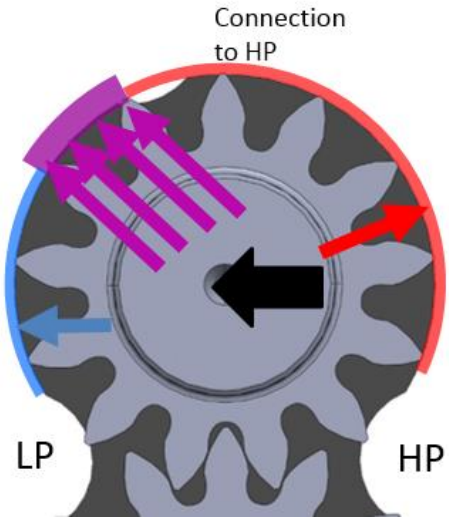

Figure 3.7 The location of noise source loads inside the pump case.

First, there is the region influenced by the inlet region. The pressure load is simplified to a single force vector through the area of application specified from the geometry for Reference Pump #1. The time domain and frequency spectra are shown in the Figure 3.8 and Figure 3.9.

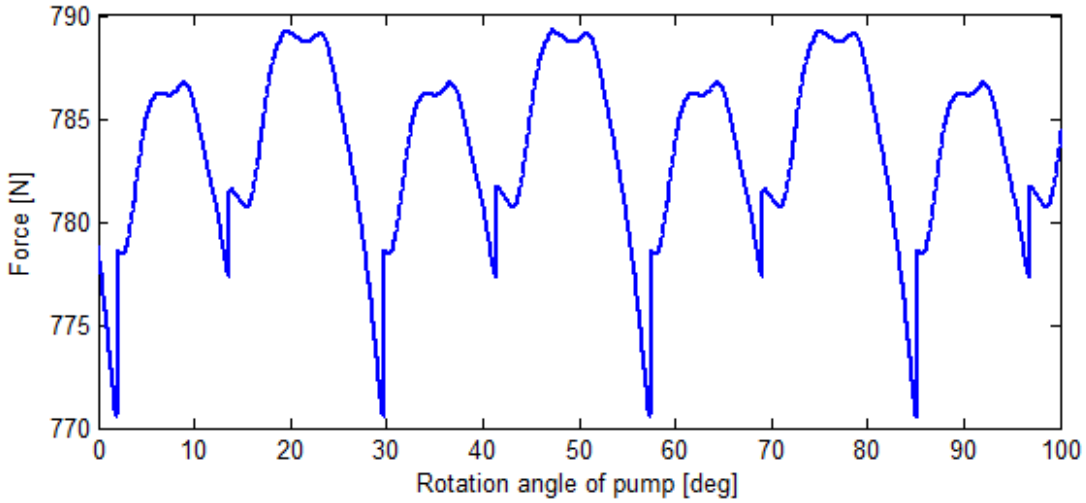

Figure 3.8: Inlet pressure ripple total force 1000 rpm 100 bar.

Note that this is for the operating condition of 1000 rpm shaft speed and 100 bar outlet pressure where inlet is drawing through a simulated line from a tank at atmospheric pressure. Other operating conditions also considered for the acoustic model are 1000 rpm 200 bar, 2000 rpm 100 bar, and 2000 rpm 200 bar.

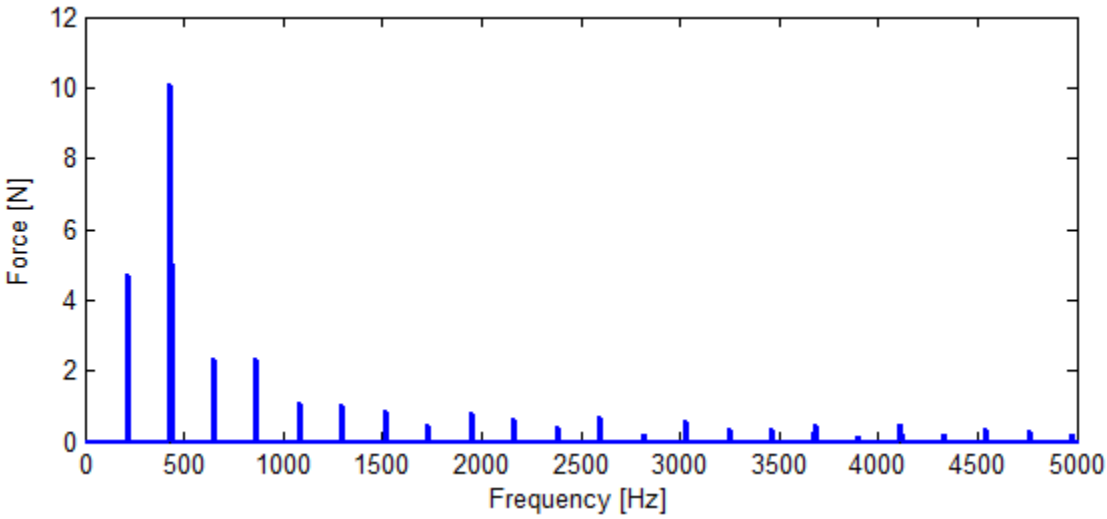

Figure 3.9: Inlet pressure ripple total force summed FFT 1000 rpm 100 bar.

Again, this is the total force applied via the inlet pressure, converted to force through the geometrical area calculation, and then converted via FFT into a frequency spectra. It should be noted that the inlet ripple has a very small dynamic component as predicted by the model.

Likewise, the outlet pressure ripple can be converted to a dynamic force using the total area of application which is 1.4 times larger than the area of application of the inlet ripple. This difference in area is emphasized in Figure 3.6.

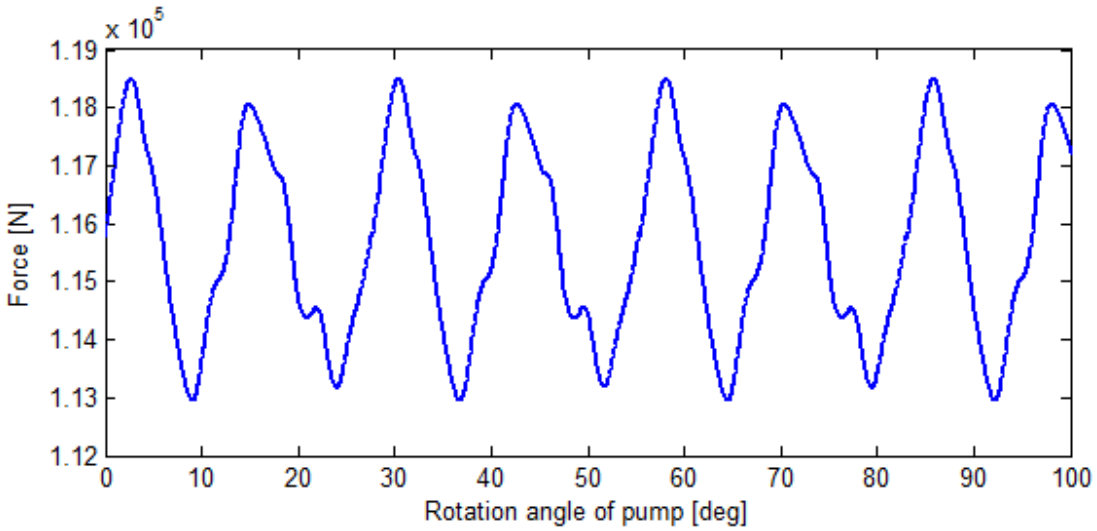

Figure 3.10: Outlet pressure ripple total force summed 1000 rpm 100 bar.

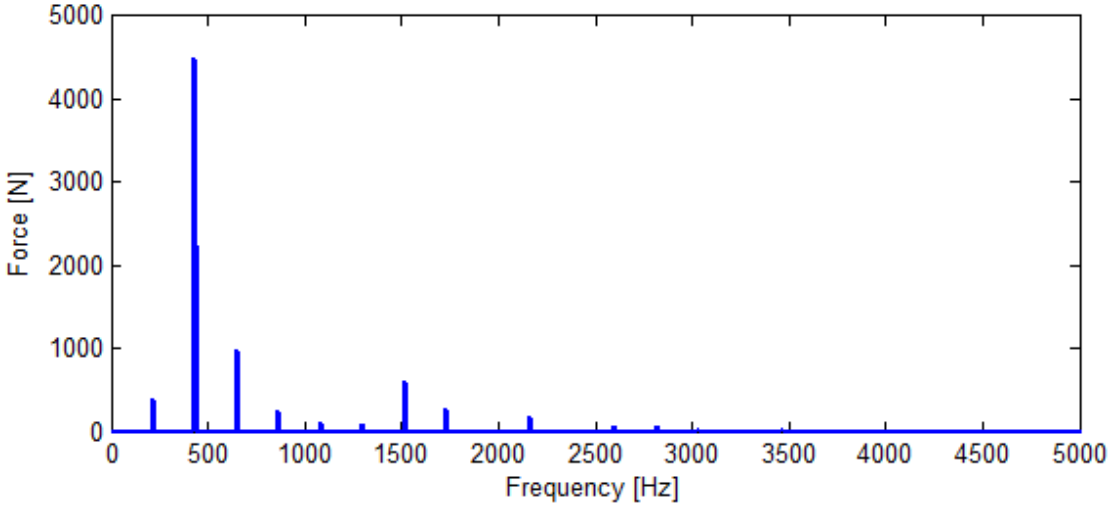

Figure 3.11: Outlet pressure ripple total force summed FFT 1000 rpm 100 bar.

The transition region where the pressurization happens is shown in purple in Figure 3.6. The pressurization occurs at every 360º rotation of the pump for each TSV. An example simulated TSV pressure for a simulated revolution is shown at 1180º in Figure 3.12 which is showing the pressure over one revolution of the pump.

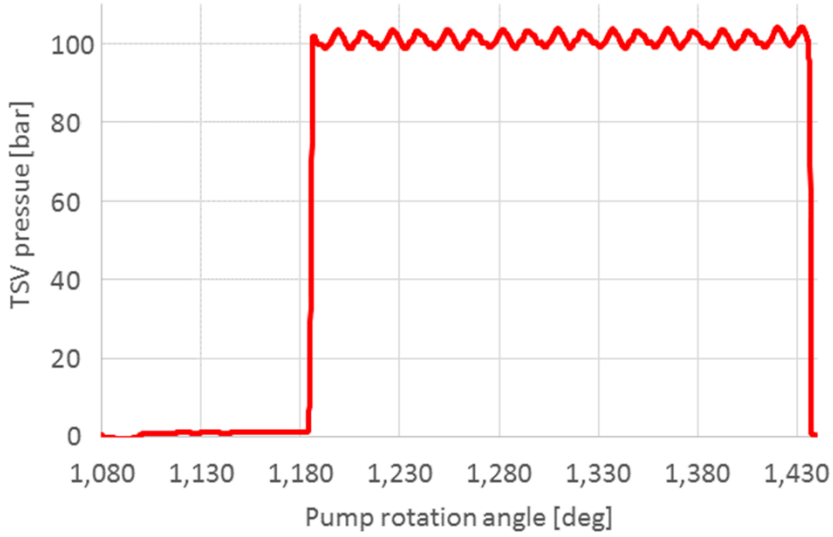

Figure 3.12: TSV pressure profile for Reference Pump #1.

The transition region affects an angle along the casing equivalent to the arc length of one TSV back from the start of the backflow groove. As each chamber rapidly pressurizes, the pump case inside the current TSV sees a hammering effect from the rapidly changing pressure. To better understand and discretize this effect, the transition region was divided into 4 equal areas and considering the force applied by the fluid pressure on the center of each area as normal to the surface of the casing at the center of each of the four areas. These four areas help approximate the hammering effect of the fluid in the TSV pulsing from inlet to outlet pressures over time. These vectors are shown in purple in Figure 3.7 and the following eight figures show the dynamic force profile at each point shown by the purple vectors.

First, the point closest to the inlet remains at inlet pressure for approximately 87% of the time as each TSV rotates past the fixed location on the case. This percentage is defined by the fact that each equivalent area is 25% of the length of one TSV and the fixed point being considered is at the center of each quarter of the TSV angle. This time profile is shown in Figure 3.13.

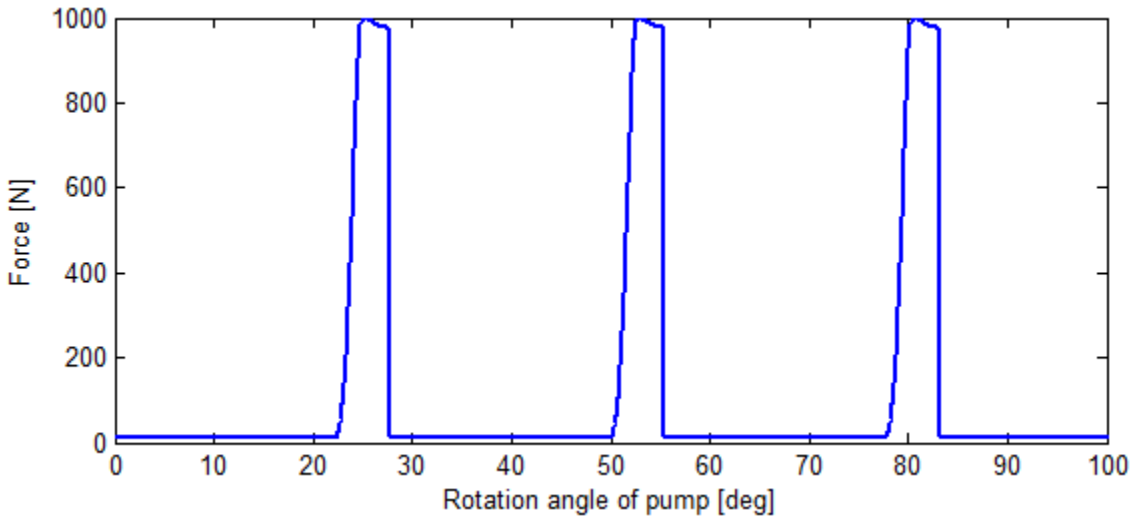

Figure 3.13: Gear 1 position 1 of TSV transition zone force 1000 rpm 100 bar.

The frequency spectra is shown in Figure 3.14 which demonstrates that there are some high magnitude components and high frequency components in the force applied on the casing in the transition region.

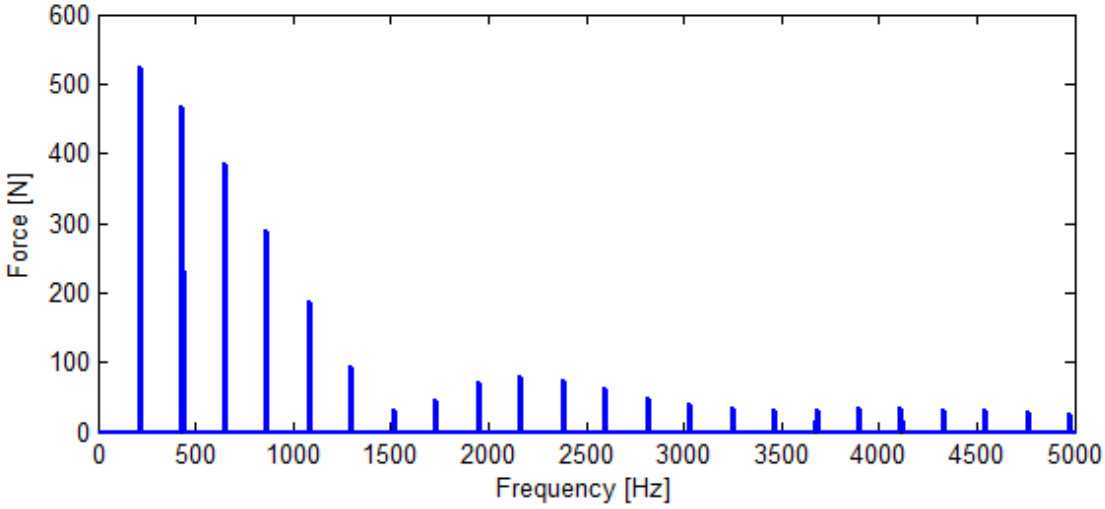

Figure 3.14: Gear 1 position 1 of TSV transition zone force FFT 1000 rpm 100 bar.

The second point on the case in the transition region shows a balance of inlet to outlet pressure of approximately 63% to 37% respectively as explained for the previous point on the case. This is shown in Figure 3.15.

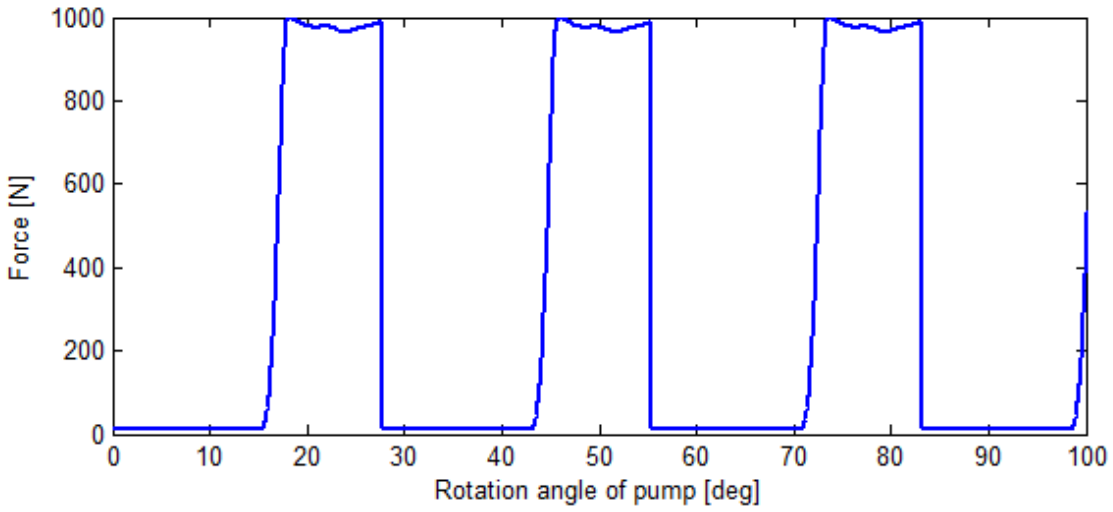

Figure 3.15: Gear 1 position 2 of TSV transition zone force 1000 rpm 100 bar.

Likewise, the frequency spectra of the force is shown in Figure 3.16 which is now on the same order of magnitude of the outlet pressure ripple force. This consideration shows that the transition region is a significant contributor to the total dynamic noise sources in the pump.

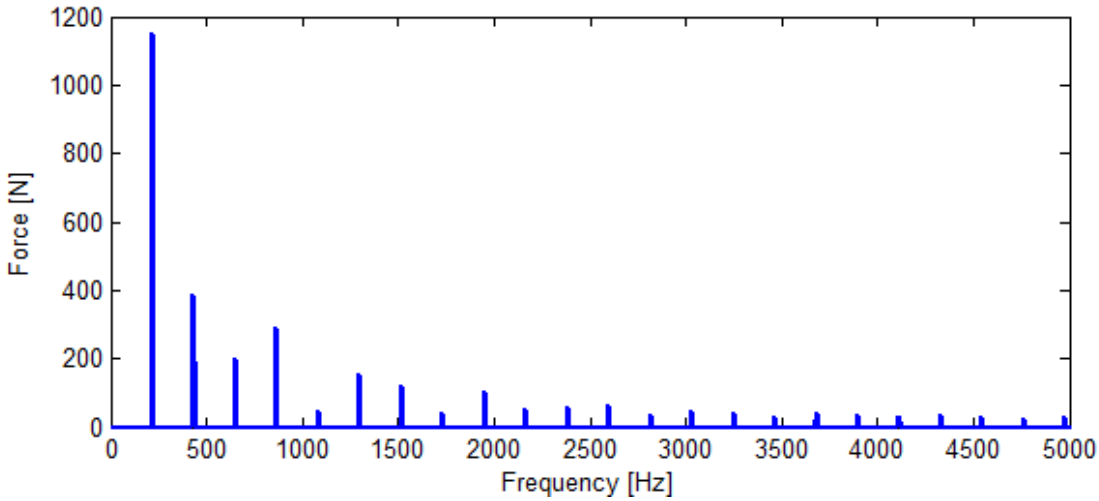

Figure 3.16: Gear 1 position 2 of TSV transition zone force FFT 1000 rpm 100 bar.

The third position on the case in the transition region is shown in Figure 3.17. This is nearly an inverted image of Figure 3.15 since its position on the case is a reflection over the centerline of the transition region from the previous point.

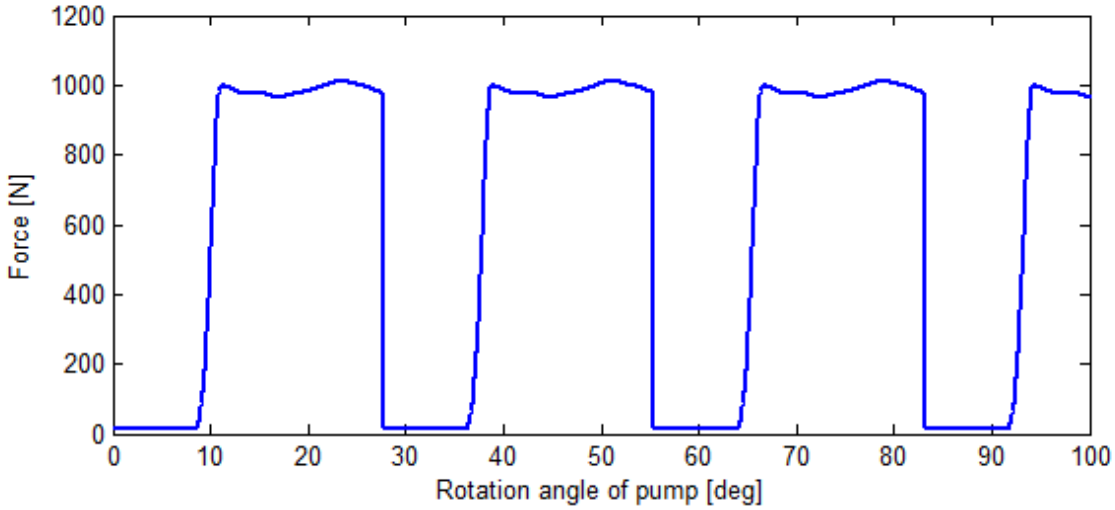

Figure 3.17: Gear 1 position 3 of TSV transition zone force 1000 rpm 100 bar.

The very similar transition region frequency profile is shown in Figure 3.18.

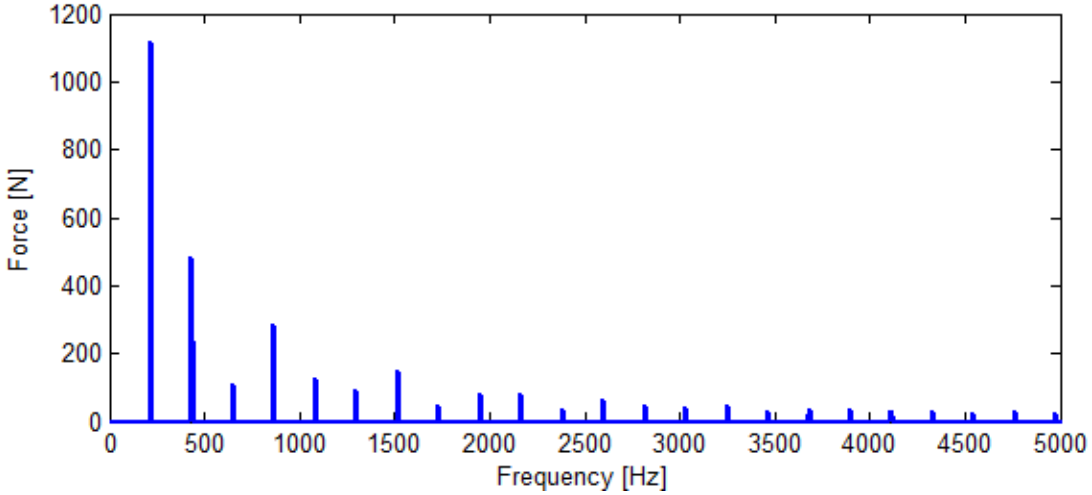

Figure 3.18: Gear 1 position 3 of TSV transition zone force FFT 1000 rpm 100 bar.

Finally, the fourth point in the transition region is shown in Figure 3.19. This position is a reflection over the TSV arc angle centerline of the position for the force profile shown in Figure 3.13 which shows that the four points selected are a reasonable and fair estimate of the changing dynamic force loads in the transition region.

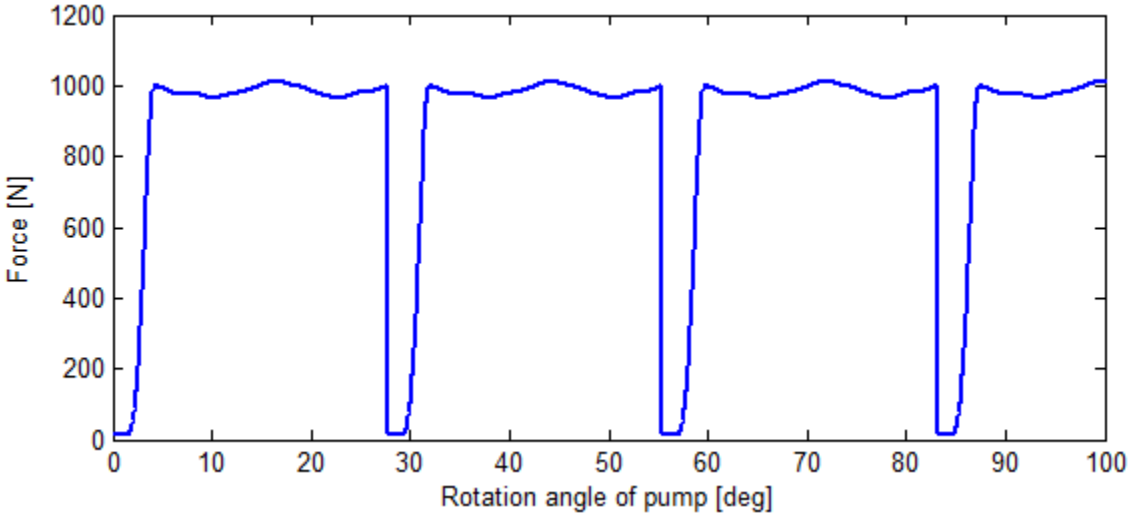

Figure 3.19: Gear 1 position 4 of TSV transition zone force 1000 rpm 100 bar.

The frequency spectra for the fourth point on the case in the transition region is shown in Figure 3.20.

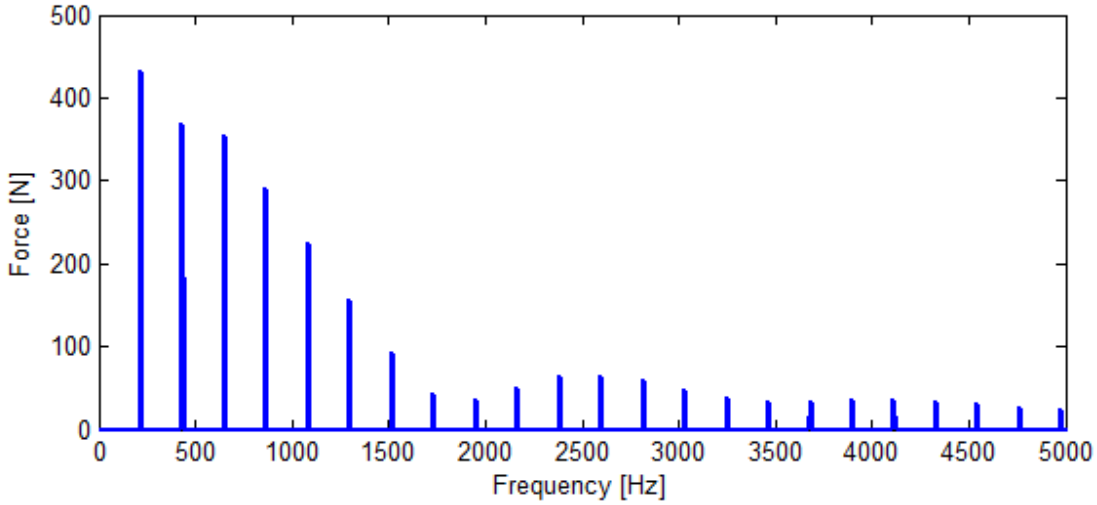

Figure 3.20: Gear 1 position 4 of TSV transition zone force FFT 1000 rpm 100 bar.

Different numbers of points and areas were evaluated for the transition region and they showed that the four points are sufficient for capturing the dynamic behavior of the force load in the transition region. For greater definition, a similar method to the area subdivision shown in the previous eight figures could be used for the entirety of the pump, but that would excessively complicate setting up the simulation.

Similar loading forces were evaluated for the driven gear transition region, but they are effectively identical to the load conditions for the drive gear since the pressurization timing for the pump is symmetric between gear 1 and gear 2. For the sake of space, the forces for the transition region on gear 2 are omitted.

The final loads considered are those calculated by the total force on the journal bearings in the pump. The total load of the bearing is converted to a single force vector as shown in Chapter 2 and this net force on each bearing is shown in black in Figure 3.7. The time transient force on the gear is the summation of the net pressure loads on the gear for gear 1 and is shown in Figure 3.21.

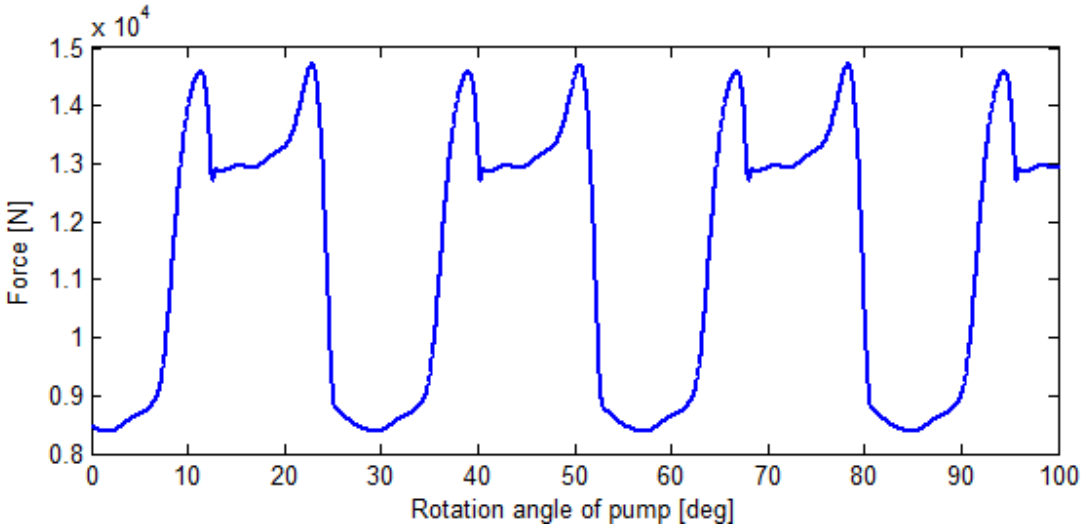

Figure 3.21: Gear 1 total bearing force summed 1000 rpm 100 bar.

The frequency spectra for the gear 1 total bearing load is shown in Figure 3.22 which shows a magnitude comparable to the total force applied by the outlet ripple.

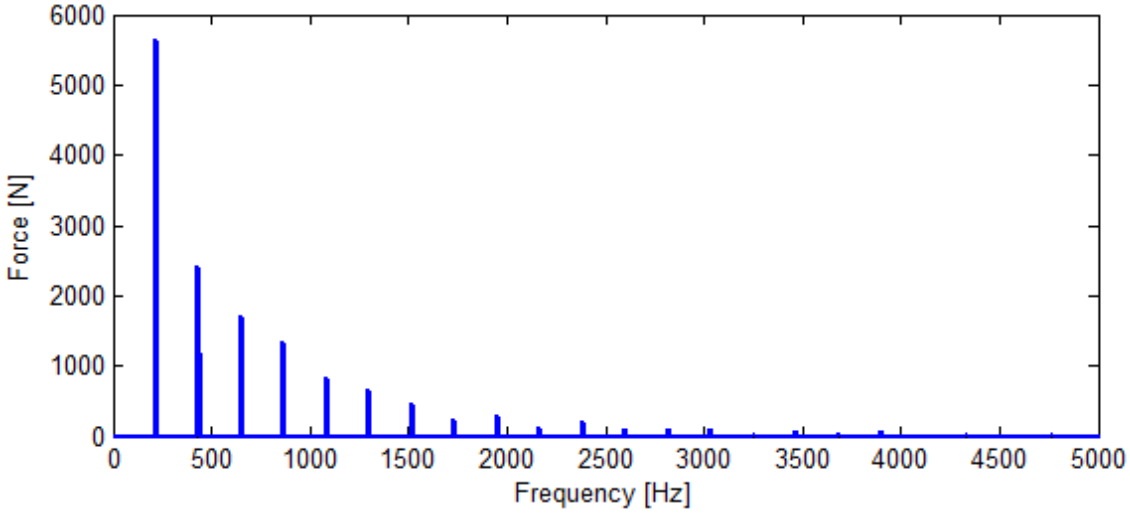

Figure 3.22: Gear 1 total bearing force summed FFT 1000 rpm 100 bar.

Gear 2 is the driven gear, which is also reacting the force transmitted through the contact points between the gears. This results in a higher required bearing force than the driven gear as shown in Figure 3.23.

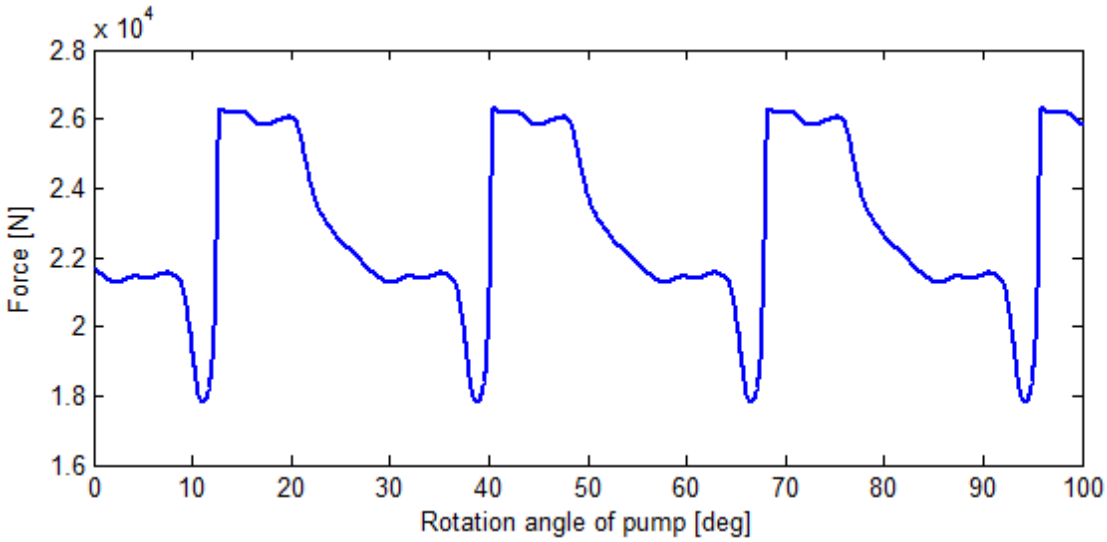

Figure 3.23: Gear 2 total bearing force summed 1000 rpm 100 bar.

This also results in the frequency spectra shown in Figure 3.24.

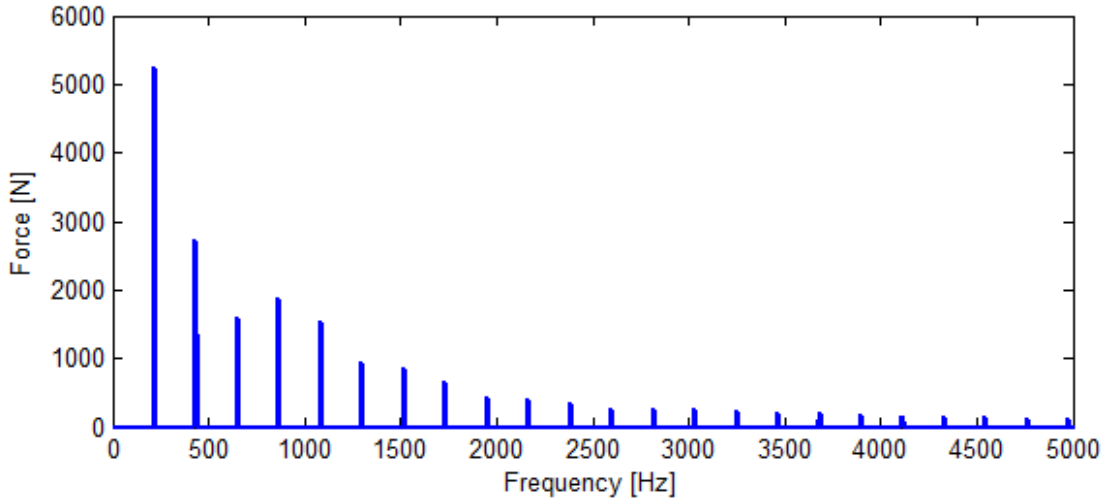

Figure 3.24: Gear 2 total bearing force summed FFT 1000 rpm 100 bar.

The bearing forces are then split in half assuming a symmetric loading of the journals at either end of the gear shafts.

Summarizing the previous figures and also showing the load conditions for all four operating points are shown in Figure 3.25.

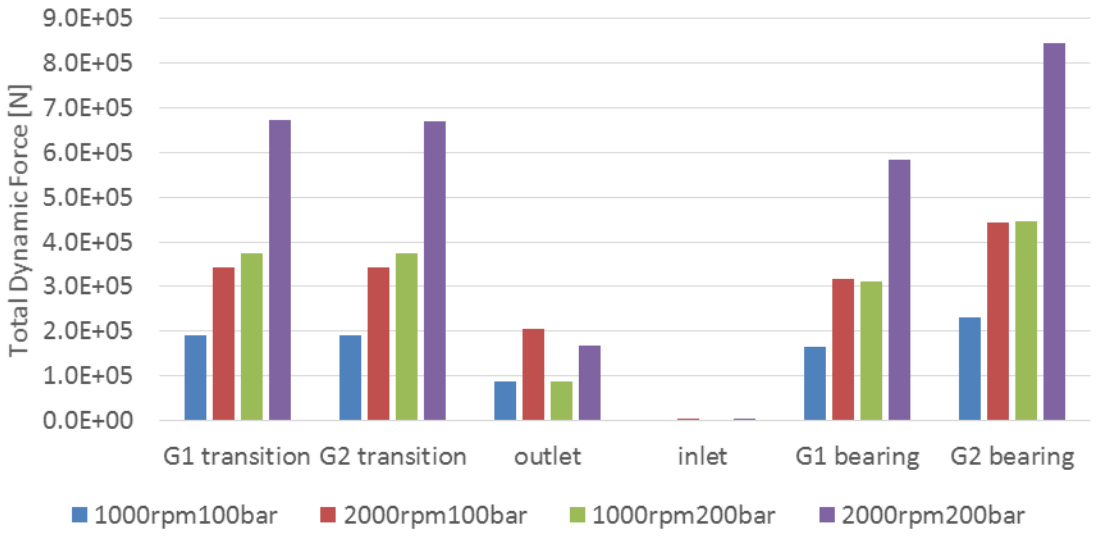

Figure 3.25: Summary of loading forces

This emphasizes that the transition regions where the pressurization happens and the SBN source of the bearing load are large sources of noise inside the system and when only the body of the pump is considered, the outlet ripple is actually smaller than the other loads. However, if hydraulic lines are also included, the contribution of the outlet load will

increase with respect to the total noise generation. More so, compared to the outlet ripple, the other sources of noise predicted by the model have much larger high-frequency components which are likely to interact with the structural resonances of the solid body of the pump while the outlet pressure ripple is more likely to interact with the much lower resonances of other components in the system as is discussed in following sections. The main loads of the pump increase with both an increase in speed and also with an increase in outlet pressure. It should be noted that increasing the pressure in the pump model does not increase the dynamic component of the predicted outlet pressure ripple. So the total dynamic force on the outlet region of the pump does not actually change with increasing the outlet pressure for this specific pump design and attached lines. Increasing the pump speed not only increases the respective pressure derivative terms, but it also increase the number of pump oscillations in a predetermined time period. These two terms are interrelated and drive the linear increase in dynamic loading forces with speed.

3.3 Structural Model and Load Attachment

A structural model of the pump is required for determining the potential resonant behavior of the pump under operating loads. For the acoustic model, the body of the pump is assembled in ANSYS as shown in Figure 3.26. The internal components are neglected for the current stage of the model. This study was done for Reference Pump #1 which is made of a cast iron body.

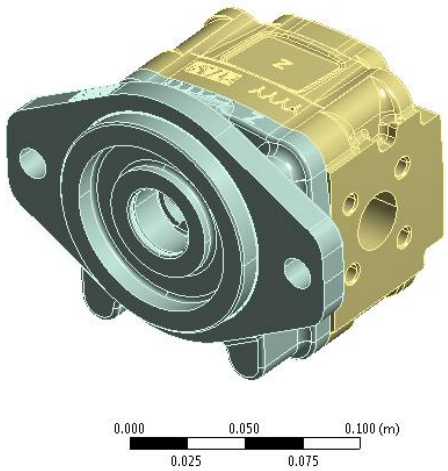

Figure 3.26: Body case assembled for meshing.

Before meshing, the two bodies are merged along contact surface, the openings in the model are blocked with 1cm of solid material, and the small surface details shown in the previous figure are removed to end up with the mesh shown in Figure 3.27.

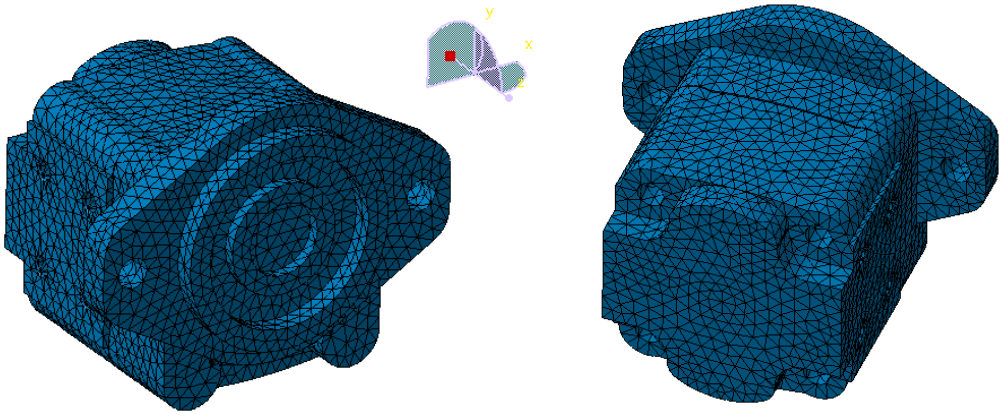

Figure 3.27: FEM mesh for example reference pump.

The goals for the FEM mesh are to accurately model the modal harmonics and the surface vibration of the pump body.

From the FEM model, the mode shapes and modal resonant frequencies can be calculated. Various refinements of the meshing parameters were studied until convergence in the predicted modal frequencies was reached. A FEM analysis of the reference pump body shows that all of the constrained modal frequencies of the body are predicted to be above 5000Hz. A first step interpretation of the FEM results predicts that the structural resonances have a minimal interaction with the excitation frequencies since the excitation frequencies in the FBN are dominated by frequencies below 5000 Hz. Since the excitation frequencies are far below the main resonances of the structure, a simple model may also be considered for the case of the particular reference external gear machine with structural resonances similar to as shown. However, for the general case, the full model is more suitable and robust for current and future work.

After evaluating the full mesh, a simplified pump body was also considered for more efficient computation during more case studies. This mesh is shown in cross-sectional view in Figure 3.28. This simplified mesh preserves the same geometrical dimensions of the original body while simplifying the amount of elements needed and hence the

simulation time by an order of magnitude. The material maximum frequency for the simplified geometry is 10 kHz.

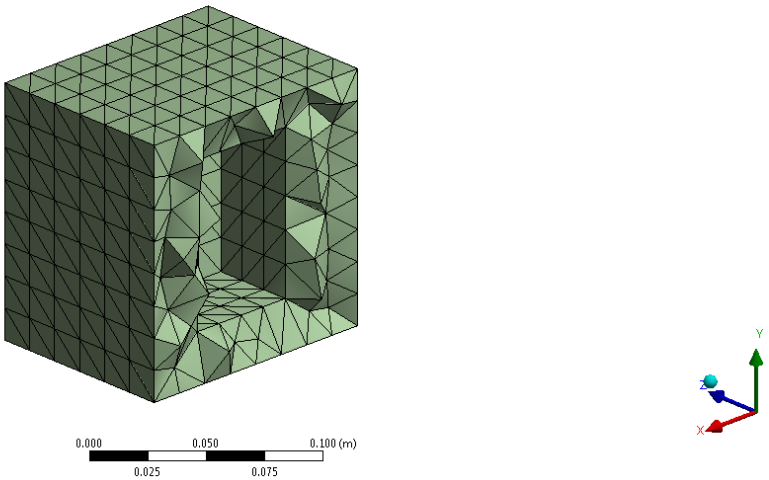

Figure 3.28: FEM mesh for simplified pump geometry.

The simplified mesh had attributes of 9954 elements including 5616 QUAD4, 956 TRIA6, and 3382 TETRA10 elements. The loads were attached to the simplified mesh as shown in Figure 3.29. One side of the mesh was constrained along the edge where the pump flange is usually located. The inlet and transition regions were applied to the interior surface facing the inlet side as shown in Figure 3.29 in purple, while the outlet force was applied on the opposite side, and the four bearing forces were applied to the lateral interior faces.

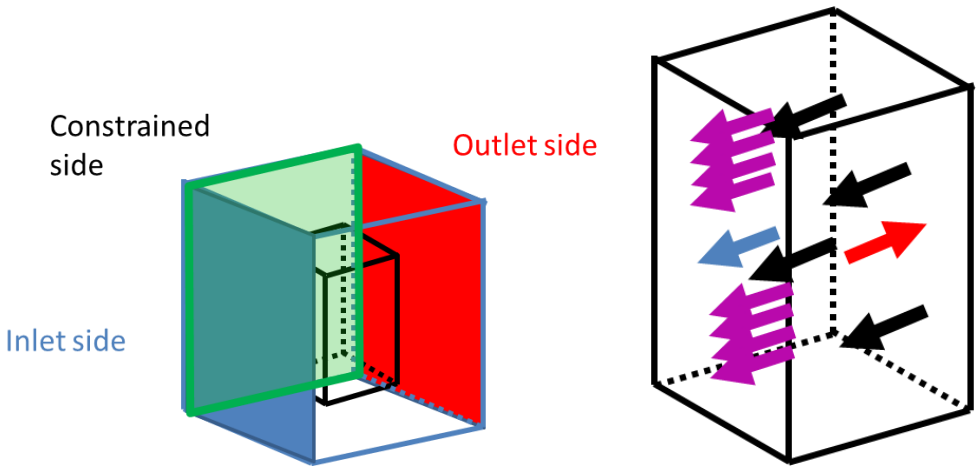

Figure 3.29: Simplified internal geometry

The load point node selection on the mesh of the real pump geometry is shown in Figure 3.30 where the outlet of the pump is shown in red on the right, the inlet in blue on the left, the transition region forces in a purple arc, and the bearing loads in orange. The node selection cannot be perfect on a real mesh, so the nearest suitable node was selected for each force.

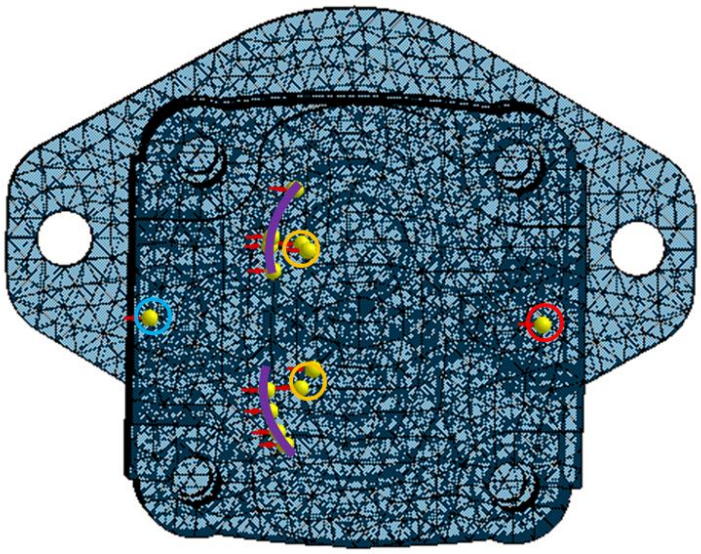

Figure 3.30: Location of force vector application on pump mesh

Modal frequencies are the frequencies that structural components will react at most strongly if the structure is excited periodically. Mode shapes are the forms the structure will take when it vibrates at a modal frequency. The first six modes are called free body modes, which displacements and rotations around the primary orthogonal XYZ axes. Several example mode shapes from higher frequencies are shown in Figure 3.31 for the unconstrained pump body. The magnitude of the modal response is dependent on the magnitude of the exciting force, so the scale of deflection is arbitrary. The red regions indicate areas of more deflection, while the blue areas indicate regions of low deflection. In practice, the vibration of the pump geometrically at a particular frequency will see the areas of high and low deflection exchange places in one cycle of vibration.

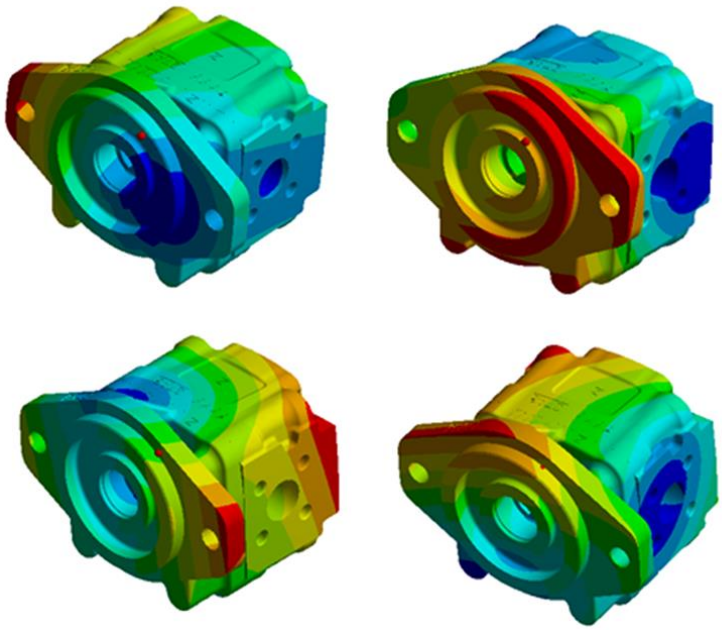

Figure 3.31: Four example mode shapes.

The simplified geometry must be compared to the original geometry in terms of resonance frequencies. Both geometries were meshed as shown in the following figure.

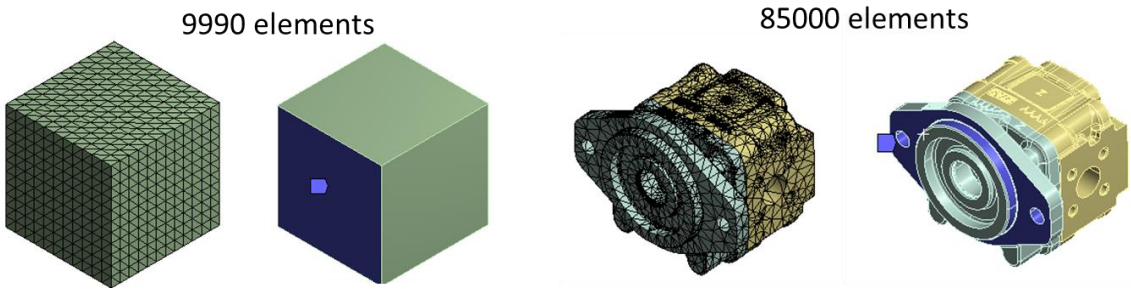

Figure 3.32 Meshed and constrained geometries.

The geometries were tested with and without constraints and with different mesh types. The selected mesh and constraint is shown in the previous figure with the blue areas constrained to ground. These meshes are shown as the light blue (constrained standard) and light red dots (constrained simplified cube) in the Figure 3.33.

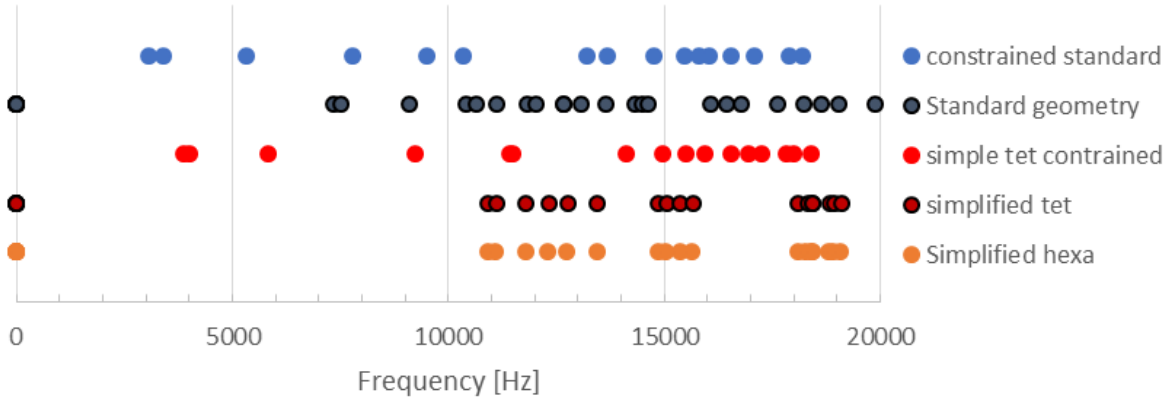

Figure 3.33 Predicted resonant frequencies.

Constraining the mesh moves all frequencies up in magnitude due to increased stiffness of the system. The free body modes now act in response to the constrained points and act at non-zero frequencies. The first three free-body modes are shown in Figure 3.34 for both the simplified and the full mesh after constraining the bodies. As can be seen, the simplified mesh follows the same general deflection shapes as the full pump geometry.

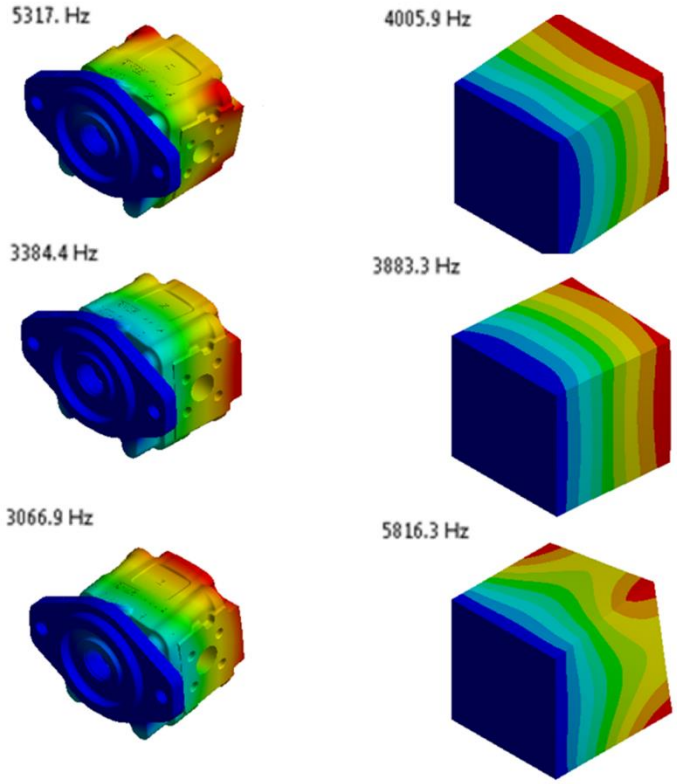

Figure 3.34 Comparing free-body modes.

Again, the magnitude of the modal response is dependent on the magnitude of the exciting force, so the scale of deflection is arbitrary. The red regions indicate areas of more deflection, while the blue areas indicate regions of low deflection since they occur in the constrained part of the pump. In the constrained modal analysis, the rest of the pump body can only move relative to the constraint. The standard geometry is nearly cubic in shape, while the simplified geometry is exactly cubic. The simplified geometry therefore has an increased concentration of degenerate modes due to the symmetry of the system. Breaking up the symmetry and using a more intermediate simplification is likely a useful extension of the work in order to examine the influence of having multiple resonant modes centered on narrow bands of frequency in the simplified model.

In order to better investigate structural effects, a deeper examination of modal harmonic modeling was considered. In the modal analysis, constraint study, the impact of applying constraints to the body during the modal analysis was investigated. The resonant frequencies of the simplified body are very close to those of the regular mesh. Even more, the location in the frequency domain of the first several resonant frequencies is highly dependent on the stiffness of the constraint that is chosen. From this, it is concluded that the simplified geometry is sufficient for various case studies to be completed using the loading conditions for Reference Pump #1. Modal damping was set to 2% for all modes which is the recommended value and also similar to the experimental values between 0.89% and 4.11% for the first 4 modes on an axial piston motor measured by Schleihs (2014).

The final steps to the acoustic model are the boundary element surface mesh shown in Figure 3.35. For the simplified geometry, using the external surface elements of the simplified rectangular volume as the BEM mesh is sufficient, while for the more complex geometry, the boundary element method is advantageous for computation.

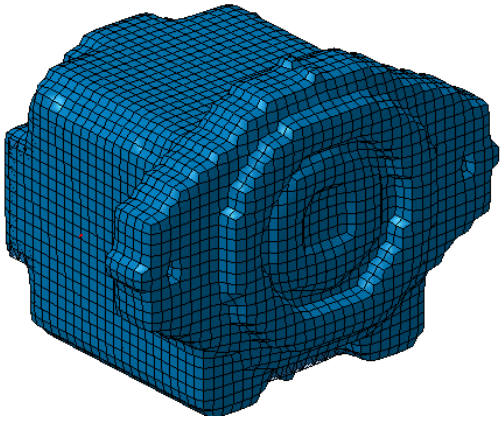

Figure 3.35 Boundary element surface mesh.

The BEM mesh size is chosen to 5mm maximum element size in order to achieve a material maximum frequency above 10 kHz.

Note that the acoustic model treats a reflecting plane (the wall or floor) the same way as a symmetry line. Instead of actually calculating the reflection at a surface, it places a mirror image of the model on the opposite side of the plane and in this way achieves the same effect. The field point mesh can be similar to the microphone grid on the real test chamber, or much finer for a close look at noise features that are infeasible to experimentally measure due to the time it would take. A standard ISO sound power mesh of a 1m radius sphere centered at the pump was chosen for ease of analyzing directionality in the results.

3.4 Potential for Structural Resonance in the Attached System

The internal dynamic forces in the pump are the main driving sources of noise in the system. However, the attachment of the pump to the system is a key determining factor in how the noise propagates out to the environment. The three dimensional structural harmonics of the attached pipe structures have an impact on the vibration and acoustic radiation from the system. A FEM model of a 1m steel pipe was developed based on the pipe geometry shown in Figure 3.36 in order to investigate what that influence might be. This pipe was selected as it is the same as used in the pressure ripple experimental validation shown in Chapter 2.

With a better understanding of the fluid harmonics described in Chapter 2, focus can now be placed on the interaction between the fluid and the structure of the steel pipe. The main structure exhibits sinusoidal geometric behavior at its own modal frequencies similarly to the pump structure. The shape is affected by both the geometry and material properties of the pipe as well as how it is constrained to the pump or other structures.

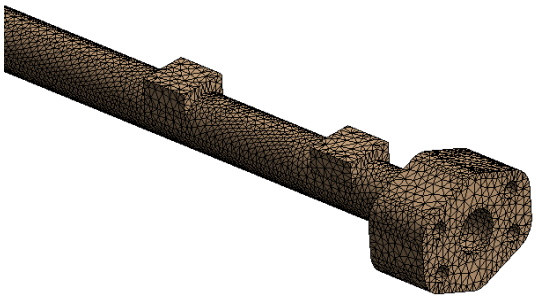

Figure 3.36 FEM model of the pipe with results.

With the 3D model, it is difficult to balance number of elements with sufficient elements across the pipe wall thickness due to the high length/diameter ratio of the pipe. Several example mode shapes are shown in Figure 3.37.

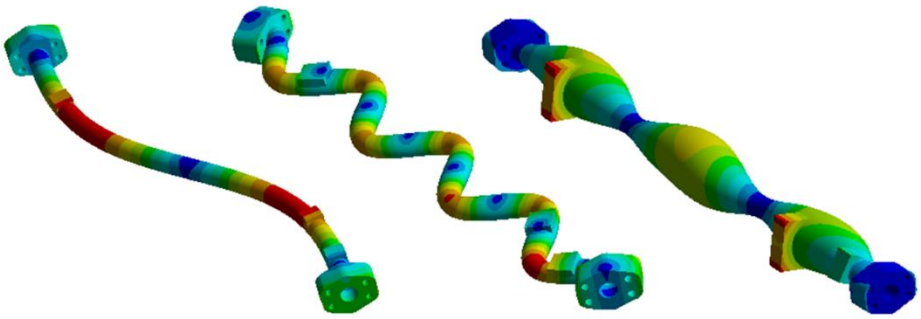

Figure 3.37 Higher order mode shapes for steel pipe.

Again, they take on the form of sine and cosine waves in the various geometric directions.

The present work considers the effects of the lines on the total noise radiation. As shown in Figure 3.38, the steel pipe is predicted to have more interacting harmonic behavior between the excitation frequencies and the structural modes due to the presence of structural harmonics in the lower frequency range. This leads to the conclusion that the

lines are very important acoustically and selection of line lengths and materials should be a primary design criteria for quiet hydraulic systems.

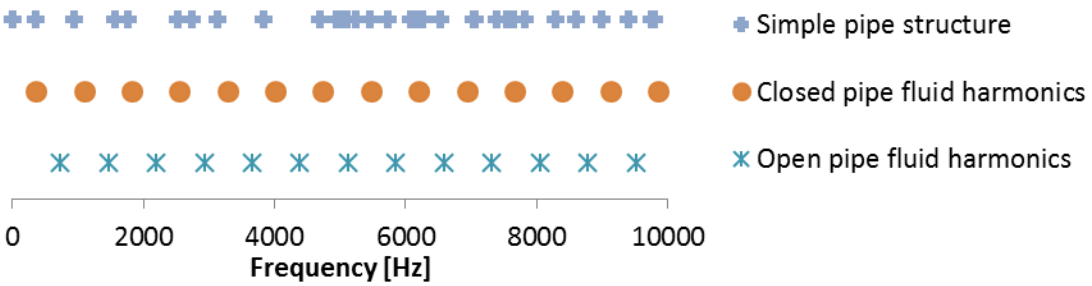

Figure 3.38 Simulated modes of fluid and pipe resonant frequencies

Due to the time constraints of the current study and the stated focus of the work on the displacement machines, the contribution of the attached lines should be noted for further study and used for comparison. However, it will not be under consideration for the main acoustic model of the pump. Likewise, the pump coupling via flange to a test bed or working machine is another potential path of noise propagation through solid structures as described in Chapter 1. However these also are left from the current considerations and are a potential path for future work on the topic. Several details from a similar methodology considering a test bed frame were shown by Schleihs and Murrenhoff (2015).

3.5 Acoustic model results

The acoustic model considers the interaction of the loads with the predicted resonances of the structures. For radiated sound power, sound intensity is the multiplication of sound pressure and the velocity field where:

$$I = \hat{p}\hat{v}_n \tag{3.7}$$

The frequency function as applied to the structure and the resulting radiated sound power is shown in Figure 3.39. This was calculated every 10.8 Hz between 0 Hz and the top frequency threshold of 20 kHz. This margin was set in the loading functions to achieve a balance between number of frequencies and simulation time. However, the accuracy of the simulation decreases above 10 kHz due to mesh size limitations. The noise floor between pump frequencies is below -200 dB and hence is not shown in the results for focus on the main peaks. For further optimization of the simulation, the frequency points in between load frequencies can even be removed from the acoustic calculation. The

difference between considering all loads as described in section 3.2 and considering the outlet load only in the calculation is shown.

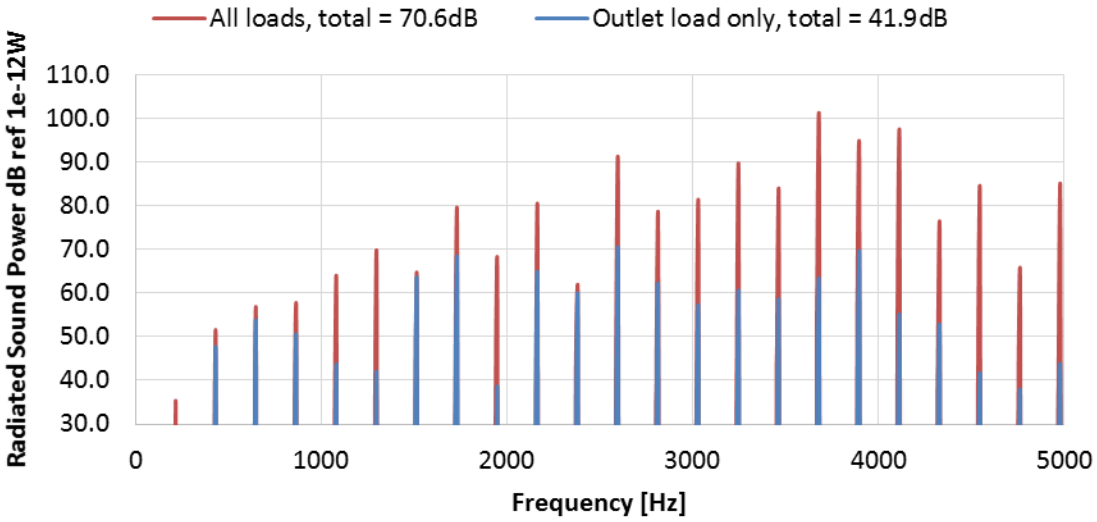

Figure 3.39 Simulated sound power of total loads vs outlet only

This shows a strong dependence in the acoustic radiation prediction on the source loads. Also, the first resonance of the simplified structure occurs at approximately 4kHz, so the structure begins to radiate more efficiently as that frequency is approached. Furthermore, the total sound power prediction is in a resonable range only when all of the load conditions are considered. When only the outlet load is considered, the predicted sound power is unreasonable in magnitude which indicates the importance of including all internal noise sources.

The sound pressure on the field point sphere centered on the pump is shown in Figure 3.40 for the first pump frequency at 216 Hz. Note that the positive X direction is the inlet of the pump, the negative X is the outlet of the pump, and the positive Z direction is the contrained surface. The elements are shrunk so that the sound pressure on the back side of the sphere can be observed.

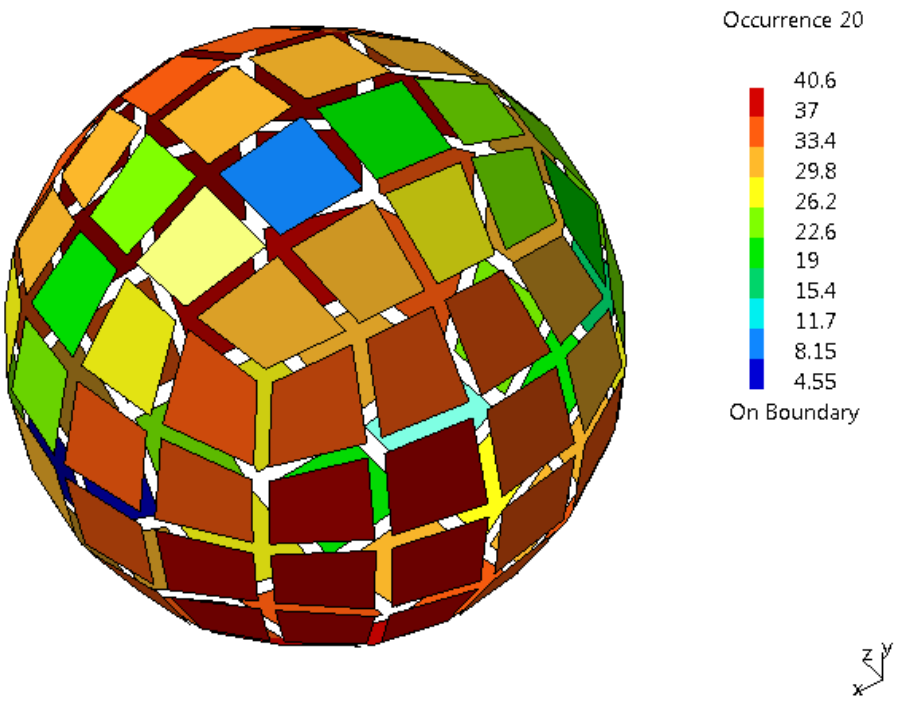

Figure 3.40: First load frequency 216 Hz at 1000 rpm 100 bar.

The sound pressure predicted shows a bias towards the inlet side of the pump, which is expected due to the higher point forces applied on the inlet side of the geometry. Also, since the modes that are being excited are the lowest resonant frequencies around 4000 Hz, the radiation of the pump resembles the motion of the pump body according to translation in the x direction resulting in the sound pressure resembling an acoustic dipole. The second and third pump forcing frequencies are shown in Figure 3.41 and Figure 3.42.

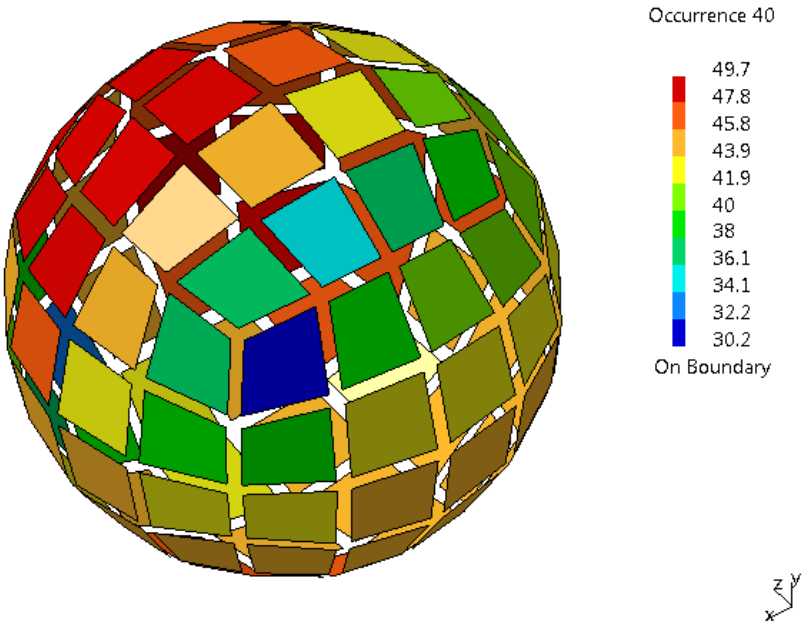

Figure 3.41: Second load frequency 433 Hz at 1000 rpm 100 bar

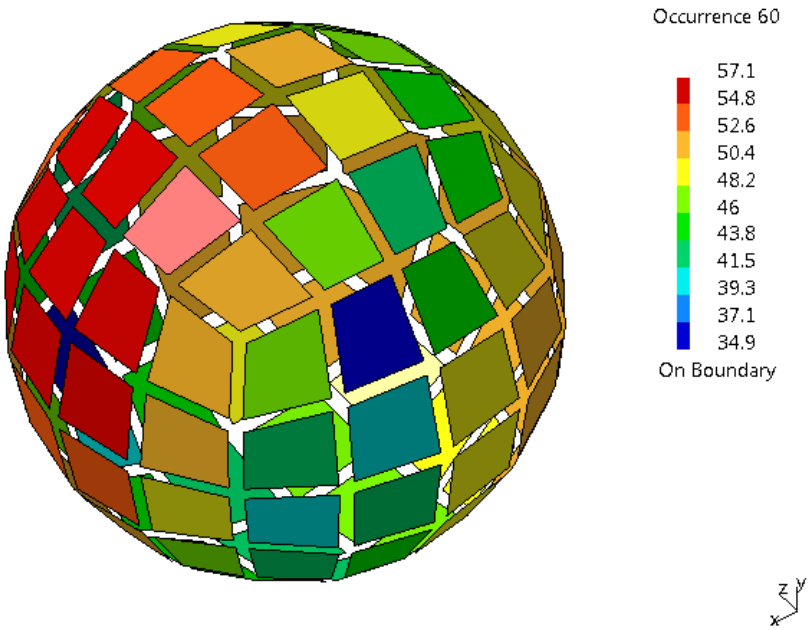

Figure 3.42: Third load frequency 649 Hz at 1000 rpm 100 bar

A higher fidelity sound power field points was also considered. The result for the third load frequency is shown in Figure 3.43 for the same orientation of the pump. Again this shows the trend towards higher sound pressure and sound power for the inlet surface of the pump.

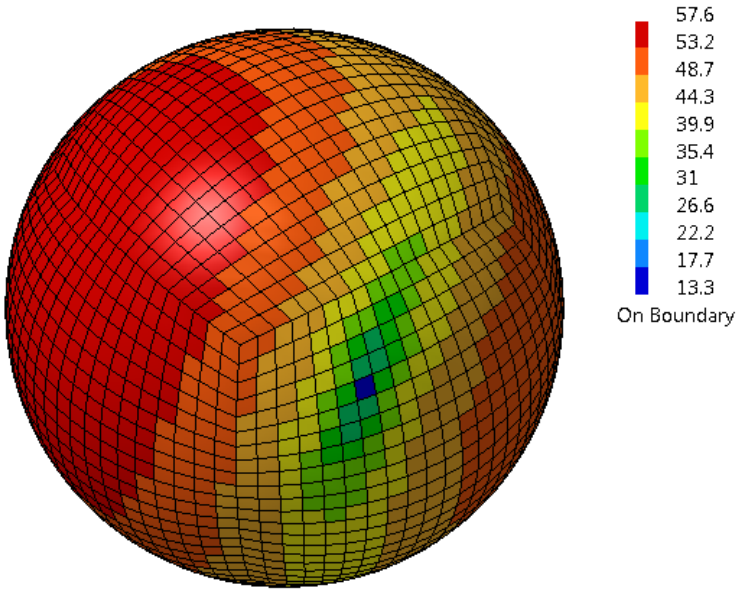

Figure 3.43: Third load frequency 649 Hz at 1000 rpm 100 bar finer mesh.

Comparing other operating conditions to the all loads 1000 rpm 100 bar case are shown in Table 3.1. This indicates the corresponding increase in radiated sound power at each of the four operating conditions considered.

Table 3.1 Acoustic model results

	1000 rpm 100 bar	2000 rpm 100 bar	1000 rpm 200 bar	2000 rpm 200 bar
Simulated SWL for Reference Pump #1	67.6 dB	69.9 dB	71.8 dB	79.0 dB
Simulated dB change	ref	+2.3 dB	+4.2 dB	+11.4 dB

Experimental measurements for sound power on similar units saw a measured SWL of +4 dB at 2000 rpm 100bar, +2 dB at 1000rpm 200bar, and +7 dB at 2000rpm 200bar. A similar trend has also been seen in measured sound pressure level for a variety of pumps where there is a larger increase in measured sound radiation for an increase in speed compared to the simulation which is predicting the larger increase from an increase in pressure. Both simulation and experimental agree that there is a non-linear increase in radiated sound power when both speed and pressure are increased.

A hypothesis for why the model under predicts the increase in SWL when speed is increased is that at high speeds the pump operation becomes more dependent on the interaction of the pump with the prime mover. This effect is not present in the acoustic model, which leads to the decreased accuracy of the model prediction.

A second conclusion would be that the experimental data includes radiation from the hydraulic lines and pressure. These components are in deep contact with the lower frequency components of the outlet and inlet pressure ripple.

The model is very useful for understanding the impedance of the structural elements and allows for further development of acoustic models that can be used as a transfer function for noise from internal sources out to the environment. Also, it indicates the importance of including features which are difficult to model including internal part motion and mounting techniques. These features can have a large impact on the experimental setup while not affecting the acoustic model of the pump body.

Through acoustic modeling, a greater understanding of the phenomena of noise generation in EGMs can be found. The potentials of the research include applying new knowledge to improving gear pump designs through structural modifications, targeted quiet speed ranges, and general noise performance improvement. An additional benefit is in predicting noise improvements for prototypes designs before production. The primary goals of the continued research are to validate numerical noise predictions in each domain of fluid, structure, and air by comparing to experimental data.

The previous work on fluid-borne noise included optimized designs of prototypes with internal additional volumes or internal holes connected to TSVs and ports. Also there were efforts for reduction of flow and pressure pulsations at outlet while still maintain efficiency and performance. The acoustic performance of the new designs can now be predicted before prototypes are produced. More investigation is needed including comparing experimental results to simulation and gaining a better understanding of phenomena to relate force pulsations in different areas in the pump to noise.

3.6 Impact of modal damping

A final consideration is the impact of modal damping on the predicted acoustic radiation. The modal damping is applied individually on each resonant mode of the structure and this method is useful for both fast computation as well as evaluating the different effects of damping on a mode-by-mode basis as opposed to general Rayleigh damping as shown by Bianchi (2010). Schleihs (2014) measured modal damping of between 0.89% and 4.11% for the first 4 modes on an axial piston motor. This indicates a reasonable range of values for similar stiff structures. However, Schleihs measurements were completed with a case drained of oil, so an additional modal damping percentage of 10% was also considered and tested using the acoustic model. The spectra for these results are very similar as shown in Figure 3.44, with the only difference coming near the first resonant frequency of the pump structure at 4000 Hz.

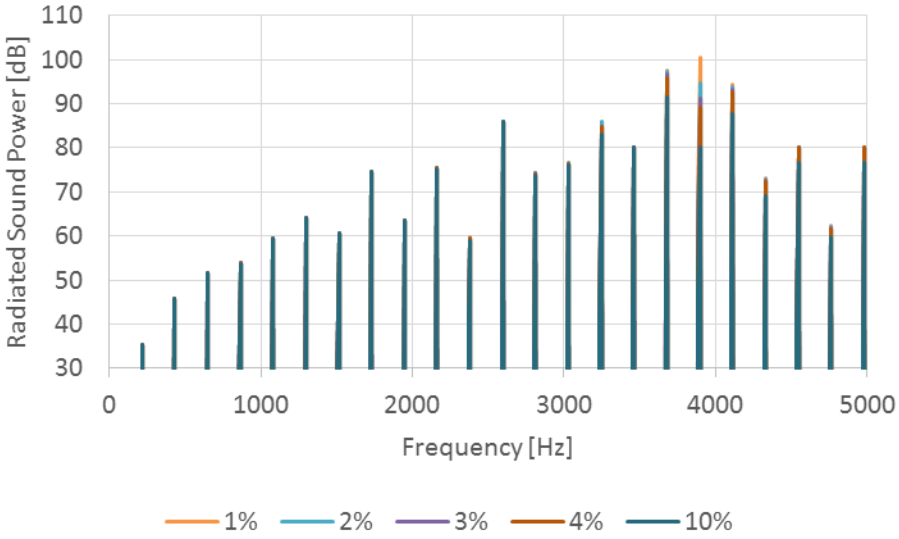

Figure 3.44: Radiated sound power spectra depending on modal damping.

The summary of the predicted sound power as a function of modal damping is shown in Figure 3.45. This shows a decaying of the sound power as damping increases. While the modal damping for every mode is not the same, the reasonable range of values investigated here shows the range that the true physical pump might operate in while running.

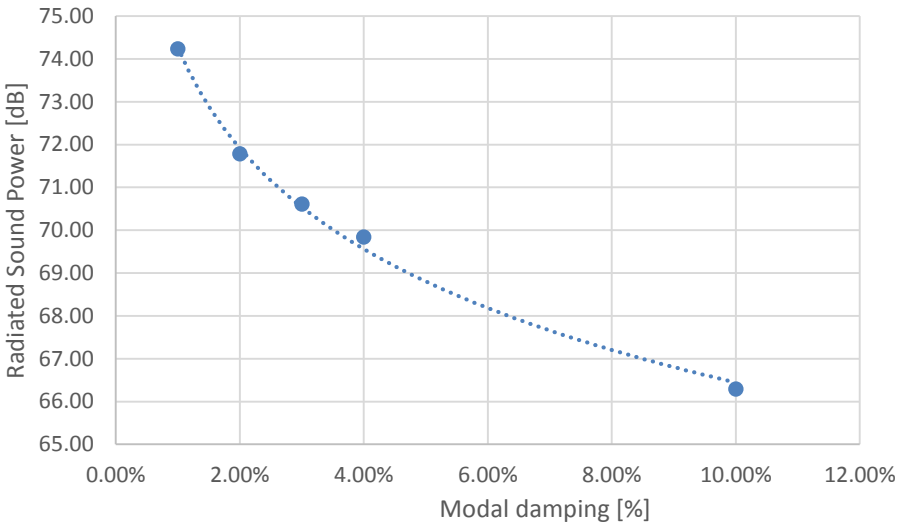

Figure 3.45: Radiated sound power depending on modal damping.

Experimental observations show that the higher frequency components and smaller than the first few pump frequencies as measured in the ABN. The original hypotheses were that this was due to the presence of strong high frequency sources in the pump body. Since the hydraulic lines are not included in the simulation, the lower frequency components would be reduced in the simulation. An additional conclusion from the modal damping sensitivity study is that it is possible that high damping the pump body is also acting to reduce the sound power radiation at high frequencies.

4. EXPERIMENTAL INVESTIGATION OF AIR-BORNE NOISE

The goal of the experimental investigation test the ISO standards for sound power and simple noise measurements and to develop new experimental methods and analyses in order to determine the underlying phenomena behind the noise propagation through the system. This addresses the goal of driving improvements both in modeling and in design of new quieter displacement machines. The Reference Pump #2 was tested in order to determine the noise performance. A goal of the noise experiments was to compare the average sound power of several of the reference pumps to examine the differences due to manufacturing tolerances and small changes in the system. A new design for the lateral plates for Reference Pump #2 was also implemented with the housing and gear kit of the reference pump which was designed according to the optimization procedure presented by Vassena (2010) with a focus on lower outlet pressure ripple. This new pump is referred to as prototype 12 and is compared to the Reference Pump #2. This chapter introduces the test rig used for total sound power, discusses the measured results, and explores the effect operating condition has on the frequencies radiated by the pump.

4.1 Anechoic Chamber Test Rig

The first aim is to quantify the noise created by the reference external gear pump and the modified prototype pump and to study the effect different operating conditions have on the noise performance in terms of sound pressure and total sound power using ISO International Standards (1989, 1999, 2001, and 2003).

The anechoic chamber hydraulic test rig circuit developed for this study is similar to the setup used in the pressure ripple experiments on the MPTR. The main difference is that the MPTR operates in an open circuit fashion. That is, the oil is drawn directly from

the tank. The anechoic room test rig is located some distance from the supply tank and thus has the fluid delivered to the inlet via a delivery pump. The main challenge involved in this is the integrity of the open circuit pump running on such a circuit. For stable operation of the relief valve and reliable delivery of oil to the test pump a supply pressure of 20 bar is chosen. A proportional orifice is used to realize a pressure drop from the supplied delivery pump down to near ambient pressure <1 bar. A proportional/integral closed loop feedback control system was built in order to realize the pressure drop from the approximately 20 bar supply pressure down to 1 bar for safe pump operation. The circuit is shown in Figure 4.1.

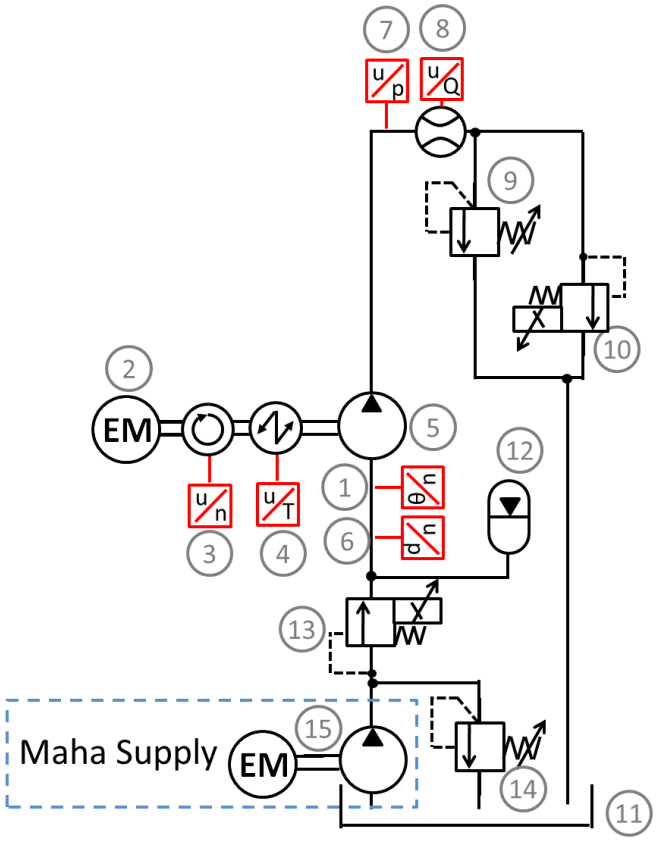

Figure 4.1: Anechoic chamber test rig hydraulic schematic.

A description of the components is shown in Table 4.1.

Table 4.1: Details of test rig components.

#	Description	Details
1	Inlet temperature sensor	Omega K-type resistive thermocouple, range 0-120° C, accuracy 1% FS
2	Electric motor	SSB, 500 Nm, speed +/-3000 rpm
3	Shaft speed sensor	HBM MC60, max 5000rpm, 0.05 Accuracy class
4	Shaft torque sensor	HBM MC60, scale 0-500Nm, 0.05 Accuracy class
5	Test pump	Reference pump #2 external gear machine
6	Inlet pressure sensor	WIKA, 0-100 bar, accuracy 0.25% FS
7	Line pressure sensor	WIKA, 0-400 bar, accuracy 0.25% FS
8	Flow meter	VS 4 by VSE, gear type, 0-400 L/min, accuracy 1% FS
9	Pressure relief valve	Safety feature only, set to 300 bar.
10	Proportional valve	Hydraforce TS10-26A-8T-N-12DR proportional orifice
11	Oil tank	Shell Tellus 32 oil, held to 52° C for 20 cSt
12	Hydraulic accumulator	2 L accumulator to damp inlet, no added precharge
13	Proportional valve	Hydraforce TS10-26C-8T-N-12DR proportional orifice for pressure reducing to 1 bar
14	Pressure relief valve	For setting inlet line pressure from delivery pump
15	Maha hydraulic supply	Delivery unit, 80 cc/rev, 1185 rpm axial piston machine

This test setup measures temperature at inlet, pressure upstream and downstream of pump, and flow rate downstream in the pressurized zone. Shaft speed and torque requirement for the pump was also measured. The outputs of sensors (6) and (7) are shown in Figure 4.2 for an example operating condition of 1000 rpm 100 bar. The operating conditions considered were from 500-2500 rpm and 50-250 bar.

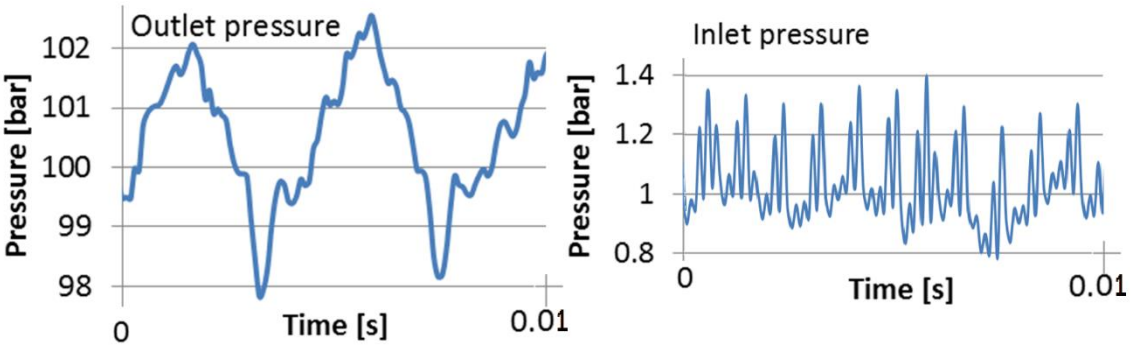

Figure 4.2 Pressure ripple measured during 1000 rpm 100 bar testing.

The complicated inlet pressure ripple which is caused by an interaction of the delivery pump (15) with the proportional valve (13) and the inlet accumulator (12). The primary frequencies are 110 Hz and its fourth multiple 440 Hz. The magnitude of the inlet ripple is very small with respect to the outlet ripple.

4.2 Acoustic Measurements

The sound pressure and sound intensity are calculated in the same manner as Klop and Ivantysynova (2011) and use the same equipment shown in Table 4.2.

Table 4.2: Description of noise measurement equipment.

Item Type	Description
Sound intensity probe	GRAS, three microphones Type 40A0 – Sensitivity 0.2 dB ref 2·10-5 Pa, ½“ diameter
Pre-amplifier	GRAS, Type 26CB, ¼“ diameter
Signal acquisition module	NI 9234, 4 channels, 51.2 kS/s per-channel maximum sampling rate, ±5 V input
High speed USB Carrier	NI USB 9162 – bus powered carrier for portability
Sound power source	B&K type 4205; SWL range 40-100 dB ref 10-12 W, frequency range 100 Hz to 10000 Hz.

The sound intensity probe used is shown in Figure 4.3. The noise measurements were made using two sets of microphone pairs. The two microphone pairs (three microphones total) for increased frequency range with reduced error in calculating sound

power. The blue padding around the third microphone pre-amplifier is for increased stability in clamping the probe at specific locations on the microphone grid. One pair is used for frequencies above 500Hz, and the pair farther apart is used for frequencies lower than 500Hz for greater accuracy. The measurements are made on a virtual surface enclosing the pump, and the entire setup is placed inside the semi-anechoic space.

Figure 4.3: GRAS three microphone intensity probe.

Figure 4.4 shows a two dimensional view of the principle of measuring sound power. All noise generated by the source must leave the virtual boundary exactly once. The directionality of the sound is found by the phase lag between microphone pairs since the pairs are oriented perpendicular to the measuring surface. Moreover, the surrounding anechoic space does not allow reflections of sound back to the source so some characteristics of the measured sound field directionality can be used to observe the acoustic performance of the pump at discrete points.

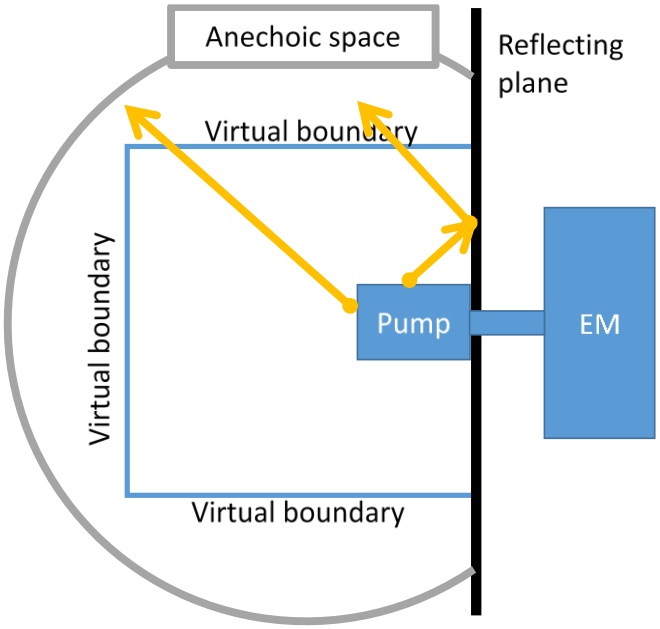

Figure 4.4: Measuring sound leaving the virtual boundary.

The primary phenomenon measured by the microphones is the sound pressure fluctuations. From this, the root-mean-square (rms) pressure can be found

$$p_{rms} = \sqrt{\frac{{p_1}^2+{p_2}^2+\cdots+{p_n}^2}{n}}. \tag{4.1}$$

Where n is the number of terms. According to the standard reference pressure p_{ref} = 20 µPa = pressure oscillation on the threshold of human hearing, the sound pressure level is

$$L_p = 10log_{10}\left(\frac{p_{rms}}{p_{ref}}\right)^2 dB \tag{4.2}$$

Where 1 Pa oscillation = 94 dB is considered a loud sound, hearing damage can start at 85 dB over long-term exposure. Note: 6 dB is a doubling of sound pressure oscillation level, (e.g. 2 Pa is 100 dB). The sound intensity is found from

$$I = \hat{p}\hat{v}_n = \frac{Im(G_{xy})}{\omega\rho_0\Delta r} \tag{4.3}$$

Which is pressure times velocity, which is found based on the phase lag between the two microphones in the pair through the cross-spectral density term G. Sound power through the surface (positive if leaving) can be found by summing the intensity over the surface areas such that the total sound power is given by

$$W = \sum_{i=1}^{N}(I_{ni}S_i) \qquad W_{[dB]} = 10log_{10}\left(\frac{W}{W_{ref}}\right) \tag{4.4}$$

The reference sound power level is W_{ref} = 1e-12 Watts. The measurements are completed according to ISO 16902-1 (2003) standard for measuring sound intensity and deriving sound power of pumps and motors. This allows for mappings of Sound Pressure Level (SPL) and Sound Power Level (SWL) as demonstrated in the following image made during a test setup calibration experiment. This was made from 62 total measurements on four planes shown in Figure 4.5 with data taken at 50 kHz sampling for 4 second periods.

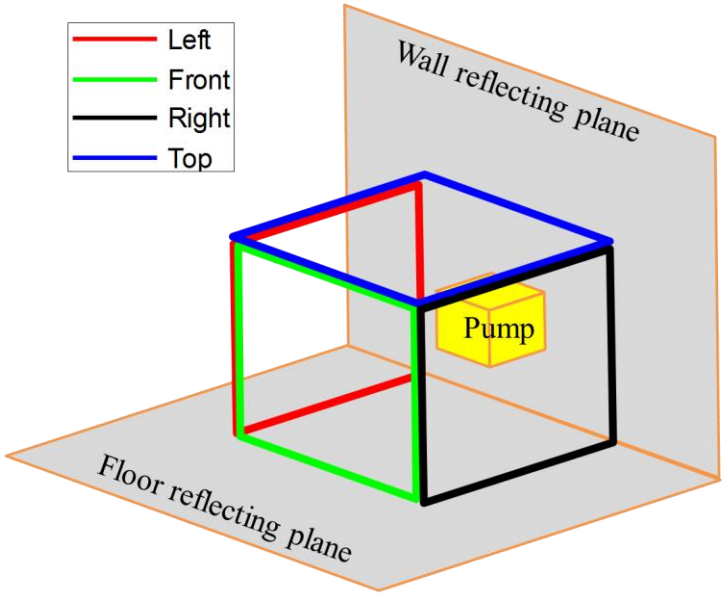

Figure 4.5 Locations of four measurement surfaces.

The advantage of this method is that the total sound power of the pump can be accurately measured without an impact of the structures and equipment outside of the grid volume. The main disadvantage is the time required for each operating condition when using a single intensity probe and manual movement of the microphones. This leads to a very coarse grid of operating points which is not good for spotting spatial trends related to changing speed or pressure and introduces more uncertainty into the measurements.

4.3 Acoustical Testing Results

The following are the results of many noise measurements completed on the reference pump. Four identical pumps of were acquired for a comparison of the consistency

with respect to manufacturing tolerances. The representative pump was tested. The SPL mapping shows the general location of the highest sound pressure levels, while the SWL mapping shows where the most energy is leaving the surface. An example operating point is shown in Figure 4.6.

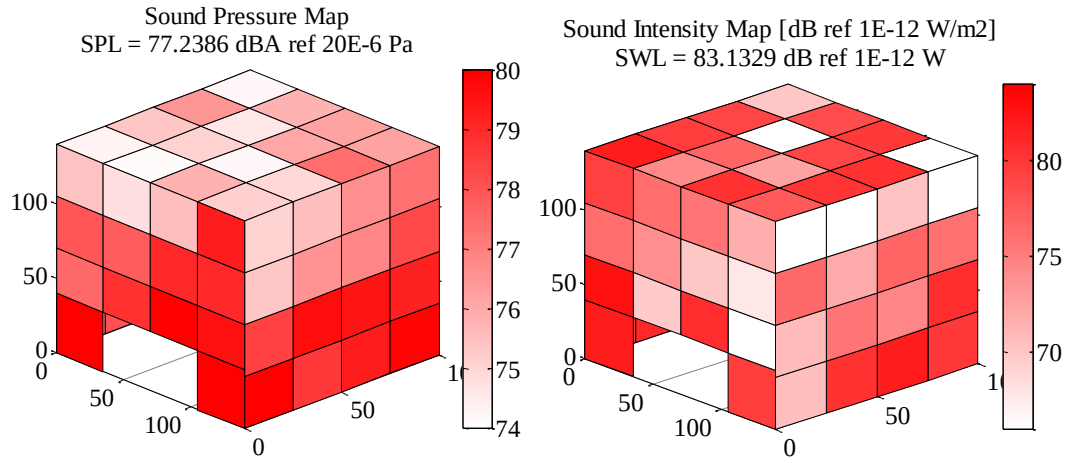

Figure 4.6: Noise measurements, reference pump 1000 rpm, 50 bar.

The high SPL near the edges is due to a concentration of sound pressure leaving the surface near the boundary due to reflections from nearby surfaces inside of the boundary. The SWL map shows a sum value (83.1 dB in the above case) which can be used as a characteristic descriptor of the total pump noise generated. The rough distribution of the sound intensity plot shows why understanding the energy leaving the pump through measurements is very difficult since there are pockets of high intensity next to pockets of low intensity scattered over the virtual surface.

A goal of the noise experiments was to compare the average sound power of several of the reference pumps to examine the differences due to manufacturing tolerances and small changes in the system. Figure 4.7 shows the total sound power of four different manufacture Reference Pump #2 under the same set of operating conditions. This is to test the robustness of the test setup and repeatability of the pump design and manufacturing with respect to noise performance. Two speeds and two outlet pressures were selected so that the impact of changing speed or pressure can be observed independently. Also shown is the result for the new prototype pressure plate pump where the only modification from

the base design for Reference Pump #2 is the geometry of the grooves on the lateral plates similar to what is shown in Figure 1.7.

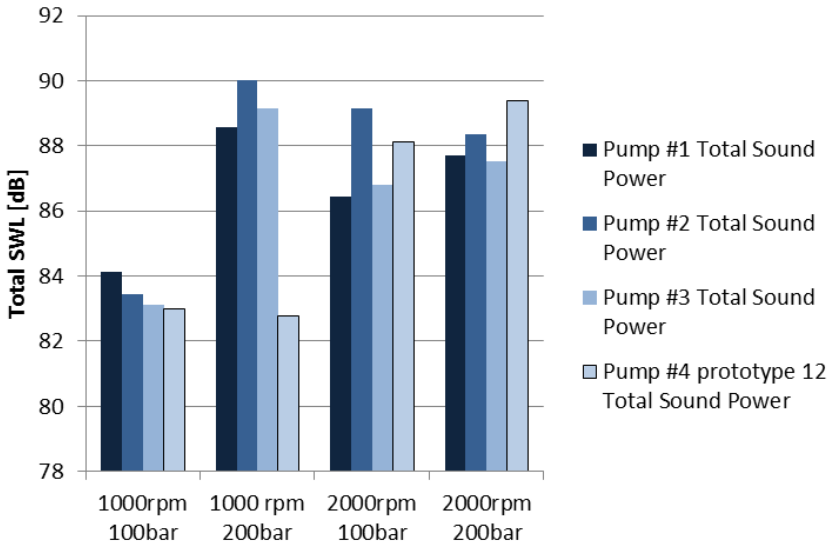

Figure 4.7: Variation in SWL across different pumps.

The first three pumps performed very similarly in terms of sound power across all measurements, as well as the test at 1000 rpm and 100 bar for pump four to test for consistency with the prototypes. The average SPL in Figure 4.8 shows a similar trend to the sound power in that the standard pumps is very similar and the prototype pump is less at the 1000 pm 200 bar operating condition.

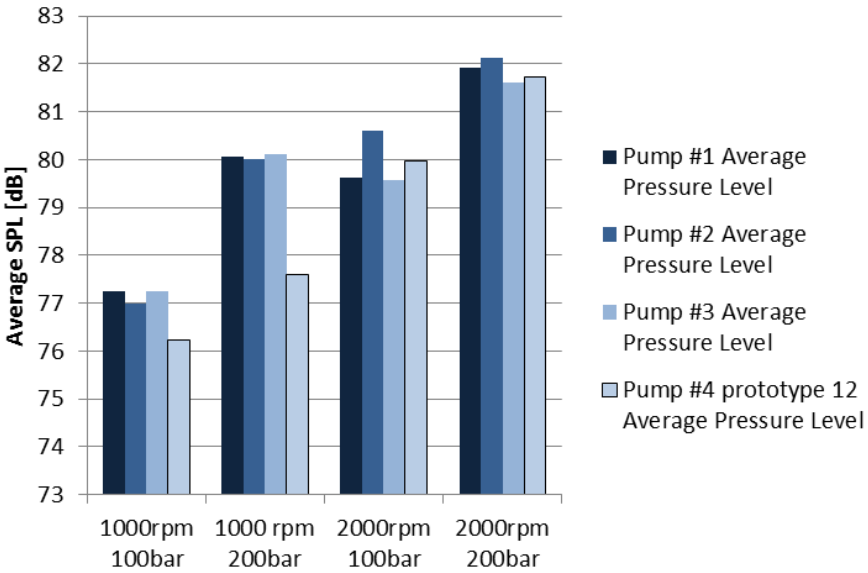

Figure 4.8: Variation in average sound pressure level across different pumps.

This is a very good result showing a large improvement of the prototype pump where the only change made was introducing the new lateral pressure plates. The mean value and standard deviation of the standard pump is shown in Table 4.3 to compare the statistical significance of the prototype measurements according to an expected normal distribution from accumulation of manufacturing tolerance and acoustic measurement errors. The 1000 rpm 100 bar and 2000 rpm 100 bar operating conditions for the prototype are shaded gray to indicate that there is very insignificant change from the standard pump. The 2000 rpm 200 bar condition is shaded light red to indicate that there may be slight increases in the sound power at this condition with respect to the standard deviation. The 1000 rpm 200 bar operating condition is shaded green to indicate the large improvement in the sound power at that operating condition.

Table 4.3: Comparison of total sound power for standard and prototype EGPs.

Operating point	SWL average of Reference Pump #2 [dB]	SWL standard deviation [dB]	Prototype design for Reference Pump #2 pump SWL [dB]
1000 rpm 100 bar	83.8	0.6	83.0
1000 rpm 200 bar	89.2	0.7	82.8
2000 rpm 100 bar	87.5	1.5	88.1
2000 rpm 200 bar	87.9	0.4	89.4

The table shows that for 1000 rpm 100 bar and 2000 rpm 100 bar, the prototype 12 sound power falls within the first standard deviation of the mean value of the standard pump. This leads to the conclusion that statistically, the prototype pump is very similar to the standard pump at these operating conditions considering manufacturing tolerances. However, at 2000 rpm 200 bar, the prototype has actually slightly higher total sound power, which is 3.4 standard deviations away from the standard pump and is statistically very likely that it generates slightly more noise than the standard pump. This result is less significant because the standard deviation of the standard pumps is the smallest at this operating condition. If the average standard deviation was used, it would fall just outside

of one standard deviation from the mean. The best result among these four operating conditions occurs at 1000 rpm 200 bar. For this operating condition, the prototype pump created 6.4 dB less total sound power compared to the average and significantly lower amounts of noise than the standard pump. This amount of improvement is statistically significant and presents an interesting case to focus on to explain the difference between the SWL at various operating points.

A comparison of the average SPL and total SWL for the standard and prototype pump at 1000 rpm 200 bar are shown in Figure 4.9 and Figure 4.10.

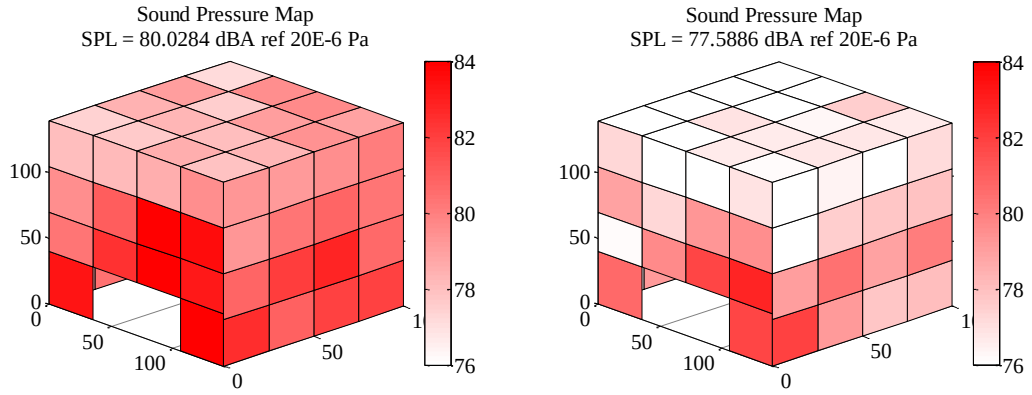

Figure 4.9: Sound pressure maps for standard (left) and prototype (right).

The SPL shows an overall depression in the sound pressure across the grid.

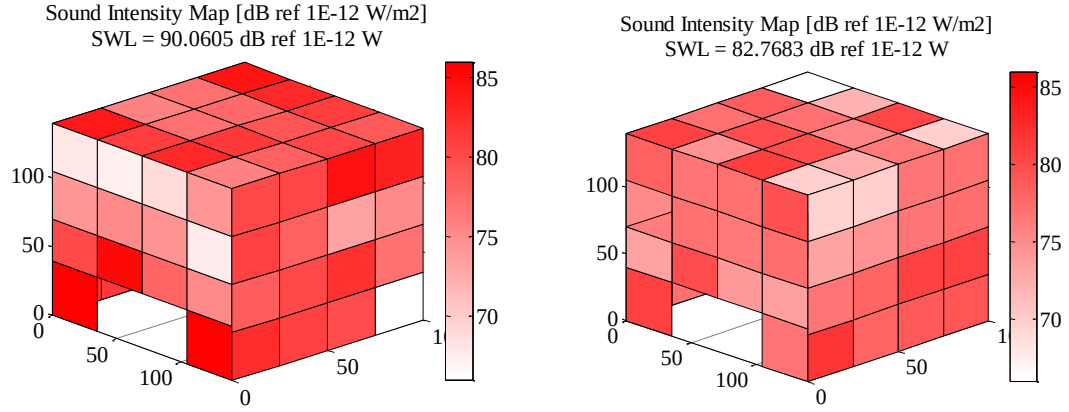

Figure 4.10: Sound power maps for standard (left) and prototype (right).

The results from the acoustic model did not have a favorable magnitude comparison to experimental sound power measurements due mainly to the differences between the idealized model boundary conditions compared to the real experimental setup. The main

differences include the presence of hydraulic lines, the attached electric motor, and the frame of the test rig. These structures contribute to both noise generation and noise propagation.

In the case of increasing the outlet pressure, typically the magnitude of the pressure ripple increases and thus the noise does also. For the case of increasing speed, the pump also becomes louder. The hypothesis was made that the noise generation between two of the measured points in Figure 4.13 is not linear with increasing speed or pressure. To test this, additional data at a finer resolution of pressure and speed points was taken at the single representative microphone location shown in the following section.

4.4 Representative Point Comparisons

Since the prototype pump only showed an improvement in the SWL at one of the four operating conditions, further studies were made to gain a deeper understanding of the noise characteristics. In order to make comparisons at a finer set of operating points, a single representative point is chose that reflects the average value of sound pressure level (SPL) at many points as shown in Figure 4.10. Taking measurements of noise on the 62 point grid is time consuming due to the manual movement of the microphone, so this experiment was chosen in order to gain a good understanding of the pump noise performance at a large variety of operating conditions.

The location of the point was chosen according to the following requirements. First, it must be far away from any features that could affect the microphone near field. Second, it must accurately reflect the average values of both the sound intensity plots and also the sound pressure plots for nearly all the available operating conditions. At the time that the representative point was chosen, sound measurements had been completed at twelve different operating conditions with at least four points repeated for three different pumps. According to these results, the point at X=1 Y=3, Z=0 was chosen according to the grid and shown in Figure 4.11. For the representative point, the magnitudes of the sound pressure cannot be reliably used for characterizing the total pump performance, but the frequency content can be analyzed on a finer set of operating points due to the increased speed of measurements when taking a single point instead of the entire 62 point grid.

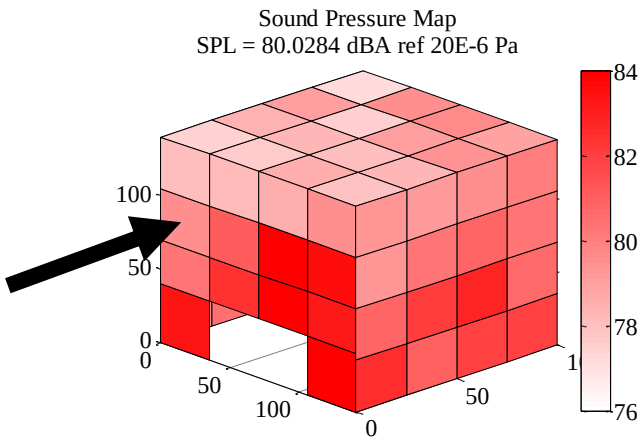

Figure 4.11: Representative point location on noise measurement grid.

A set of measurements was completed at 50 bar outlet pressure with speeds changing from 500 to 2500 rpm, and the other set was completed at 2500 rpm changing pressure from 30 to 200 bar. Figure 4.12 shows the data taken with all three microphones for two separate pumps at the same representative point. Since there is good agreement, we can make the conclusion that the pumps under consideration perform within reasonable variation of the same acoustic profile taking into account manufacturing and assembly tolerances. In this case, the measurements for one pump can be considered as descriptive of trends for the pump in general. The six lines in the figure represent each of the three microphones used in the measurement with two colors of each line because the experiment was repeated for two different pumps. The figure is an interesting result since it shows the pump as it passes through different frequency regimes of the components as the pump speed increases and there is excellent agreement between the two pumps. This will be explored in more detail in this section and the next chapter.

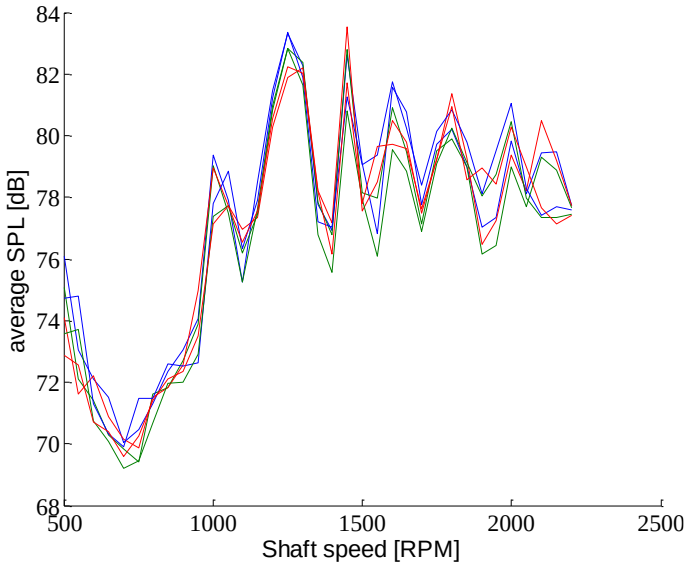

Figure 4.12: Average SPL for three microphones for two different pumps.

At constant pressure (50 bar), and varied RPM (from 500 rpm to 2500 rpm). There is a relatively coarse resolution in pump speed (every 50 rpm), and a very fine resolution in frequency due to the high sampling rate and long measurement period (Fs=50 kHz, T=~4 s). Figure 4.13 highlights the frequency content that appears at multiples of the primary pressure ripple in the form of angled lines on the graph. Lines perpendicular to the frequency axis on the graph show frequency content present at all operating speeds. These lines are due to system and structure that appear regardless of excitation frequencies.

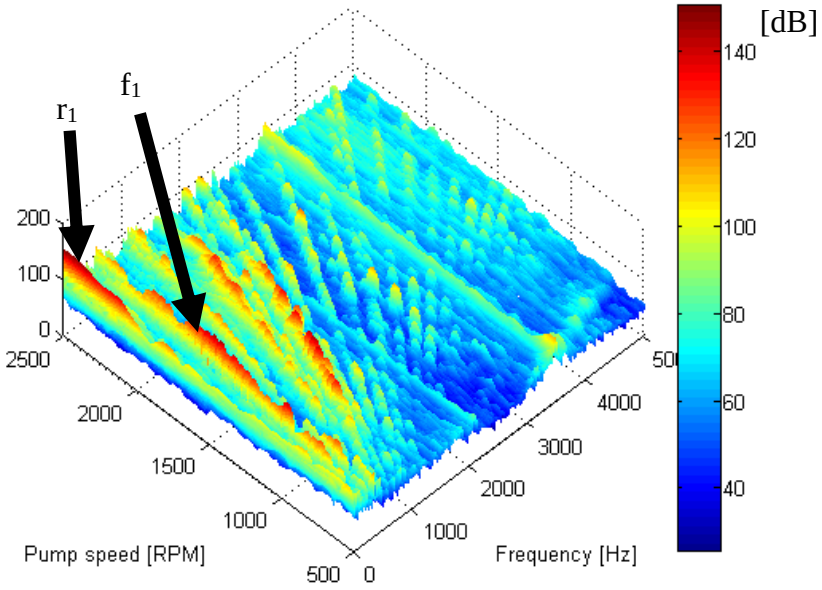

Figure 4.13: Speed-dependent PSD of ABN with 50 bar outlet pressure

A higher resolution (every 10 rpm from 500 rpm to 2500 rpm) of measurements at the representative point were recorded for the prototype pump with the same outlet pressure of 50 bar which is shown in Figure 4.14.

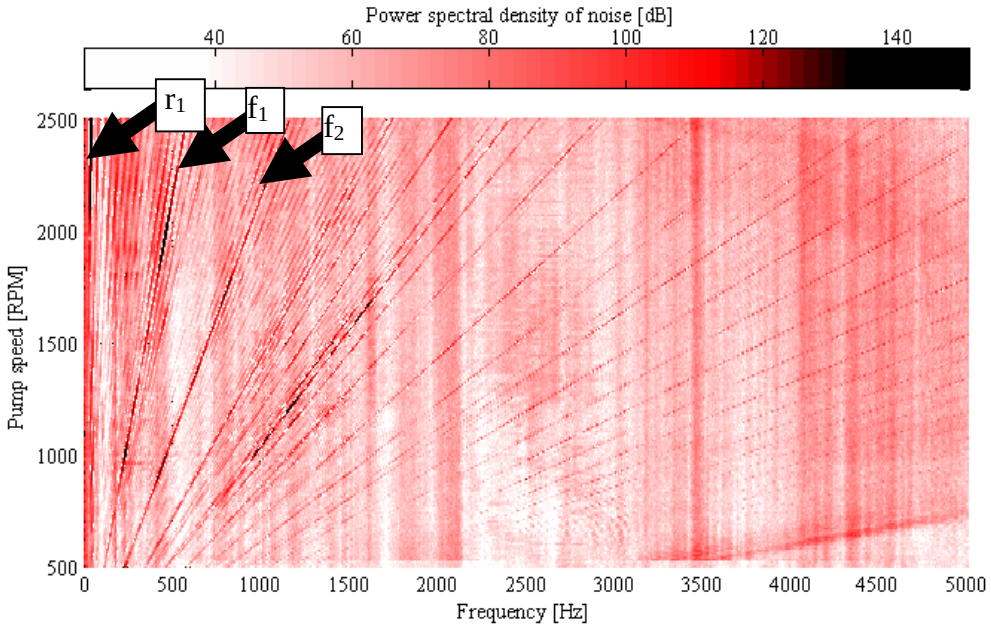

Figure 4.14. PSD of measured ABN at representative point for prototype

The frequency features due to the speed of the pump shaft and due to the number of teeth can be clearly seen. The vast majority of the energy is located at the multiples of the shaft frequency and the frequency of the teeth rotating past the outlet.

In order to better understand the dominating frequency features, the PSD is summed across frequency from left to right. This is shown in Figure 4.15. The total value can be seen from the value reached at the right-most edge of the graph. The peak levels occur at 1000rpm, 1250rpm, and 2000rpm. For speeds from 1000rpm through 2000rpm, the dominating frequencies in the ABN noise closely match those in the outlet FBN. For speeds above 2100rpm, the first frequency of the shaft becomes the dominant frequency. Hypotheses about pump performance can be made from this result. Mainly, the pump undergoes several regime changes when speed is increased. This leads to different

dominant frequencies at different speeds. Furthermore, the shaft frequency plays a large role in the noise at higher speeds above 2000rpm.

The presence of shaft frequencies is consistent with results presented by Bonanno (2008) and points toward further study into the effect of the journal bearing and shaft load on ABN at higher speeds.

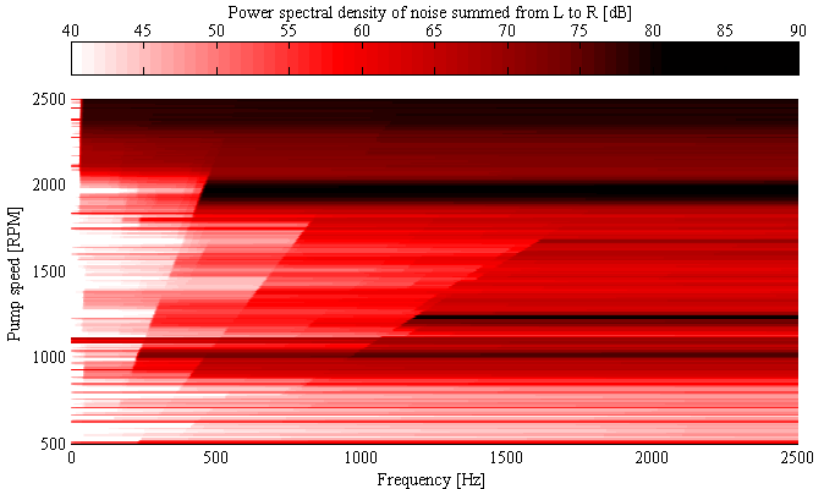

Figure 4.15. PSD summed over the frequency domain from left to right.

The comparison of the SPL for the reference and prototype pumps is shown in Figure 4.16. The SWL is also shown where the sound intensity is considered as representative for the measurement grid through the single element.

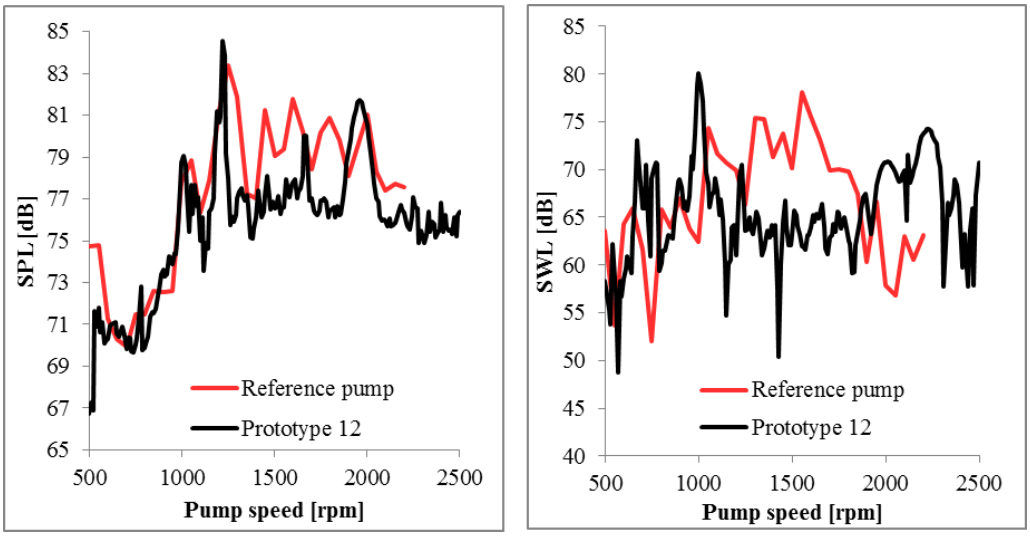

Figure 4.16. Comparison of measured SPL and SWL for representative point.

The SPL follows the same trend for both pumps, with small reductions in the overall value for the pump at speed 2 ranges from 1200rpm to 1800rpm where the FBN frequencies were dominant. The sound power was approximated from the single measurement point taken and shows that the prototype performed more poorly at speeds of below 700rpm and above 2000rpm. Nearly the exact frequencies of the FBN are the dominating effect in the ABN at the speed range from 1300rpm to 1800rpm.

To summarize, the reduced pressure ripple in the prototype pump was very effective at reducing the output power over a range of speeds from 1200rpm to 1800rpm where multiple peaks in the FBN are the dominating effect in the ABN. This result validates the initial assumption of the contribution of FBN in the ABN at those frequencies. However, at speeds where the pump frequencies are not dominating the radiated noise, improvements for the prototype were not seen.

Another trend is shown that the prototype pump generates more sound power at the representative point at the key speeds of 1000 and 2000rpm while generating less sound power at most other speeds over the entire grid. This shows the danger of measuring sound power at a few discrete operating conditions, since improvements to the sound power are very dependent on the excitation frequencies.

It is likely that at some speeds, the prototype plates provide for as much as 10dB improvement in sound power. In the range of 1200 rpm to1800 rpm, the optimization for low pressure ripple of the pump results in a significant reduction in the measured sound power. At other speeds, which includes the reference speeds of 1000 rpm and 2000 rpm, the prototype pump may perform equally to, or worse than the standard pump. To summarize, the reduction of pressure ripple due to the optimization was very effective at reducing the output power of the pump over a range of speeds from 1200 rpm to 1800 rpm where multiple peaks in the FBN are the dominating effect in the ABN. However, at speeds where the other effects dominate the noise, the optimization was not as effective.

Another experimental exploration was done with a fixed pump speed of 2500 rpm and variation of outlet pressure with the standard pump. The previous figures showed the changes due to different features of the structure and system transmitting energy more

readily under differing excitation frequencies, but there are also changes that are due to increasing pressure while holding constant speed.

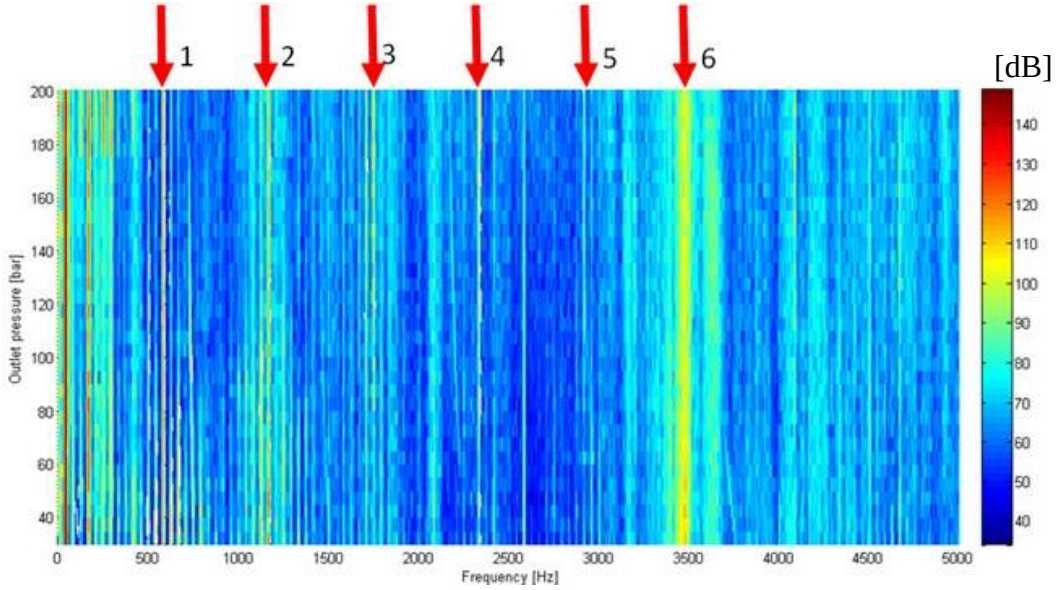

Figure 4.17: Frequency distribution of noise pressure as a function of outlet pressure.

The primary pump frequency features show up as vertical lines in this graph since the excitation frequencies are fixed with constant speed. The main conclusion that can be made from the figure is that the largest component of the noise at 2500 rpm is made up of low frequency content caused by the shaft oscillations. There is a mainly linear trend in Figure 4.17 of the power spectral density of the sound pressure slowly increasing as the pump outlet pressure increases as shown in Figure 4.18.

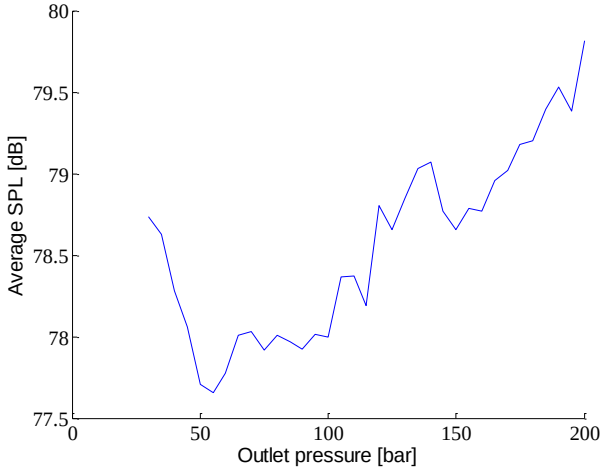

Figure 4.18 Average SPL as a function of outlet pressure at 2500rpm

This trend is expected since the excitation force is increasing but the frequencies that are being excited are not changing. An interesting note is the higher SPL at very low pressures. The main hypothesis for this behavior is that the balance of the gears inside the case was designed for high pressure use, and hence is slightly less stable at extremely low pressures. Also that the increase in overall noise rises nearly linearly with increasing outlet pressure, but "turning on or off" of some frequencies at certain pressures can result in breaks from that trend when the operating regime of the pump changes under different loads. Predicting this distribution is less interesting in general than the variation of speeds case, and it is also more difficult since changes in performance due to pressure increase are less noticeable in the model than changes to speed.

4.5 Conclusions of Noise Measurements

The measured SPL and SWL is very consistent between the four reference pumps. This demonstrates the repeatability of the measurements and also the repeatability of manufacturing with respect to noise generation. Surface plots of total SPL and SWL across multiple operating conditions should be taken as discrete points and evidence towards overall trends, but linearity between the points on a lightly populated surface cannot be assumed as was demonstrated with the representative point measurements. The representative point measurements show that the true behaviour is not linear between varying speeds or pressure and that discrete noise graphs should be evaluated carefully. The results found allowed for a greater understanding of the noise characteristics of EGPs.

To highlight the comparison to the model as discussed in the previous section. The model predicted no increase in SWL for increasing the outlet pressure from 100 bar to 200 bar with both simulations at 1000 rpm. The experimental data averaged over multiple measurements show that the total SWL increases by 3.5 dB by measuring the entire sound grid at the same two operating conditions. Experiments were also completed increasing the speed to 2000 rpm and a 4 dB increase in SWL was measured over the 1000 rpm operating condition with the outlet pressure set to 100 bar for both experiments, which is less than what was predicted by the simulations. First, this shows that the model still has much room to improve in order to better match the trends seen in the experiments. Second while

comparing the trends is useful, the experimental setup is influenced by much more than just the pump body. The SWL measured includes influences from the attached electric motor and hydraulic lines present in the real system even though the measurement technique is designed to limit this influence. This means that the absolute SWL value for the measurements and simulations cannot directly be compared to simplified model predictions. This also motivates deeper experimental studies in order to better understand the features of the pump and the system as they respond to changing operating condition.

5. MULTI-DOMAIN NOISE PROPAGATION EXPERIMENTS

This chapter documents the research efforts towards better understanding the different noise components present in an experimental system. This experimental analysis attempts to leverage all the previous measurements and modeling information in order to investigate the interaction of the system and structures with the sources of noise. The need for new methods for identification of noise sources and transmission is evident in order to direct future modeling and experimental efforts aimed at reducing noise emissions of current fluid power machines. This goal is accomplished through the formulation of noise functions used to identify contributions and transfer paths from different components of the system including Reference Pump #1.

5.1 Background

A new approach for evaluating the noise of external gear pumps was developed. This method is similar to the transfer path analysis approach used by Plunt and by Citarella (2005) both in experimental and in modeling applications, where they focused mainly on automotive applications instead of EGMs and the goal was to determine correlations and influences between one part of a complex system and another. One established application of a transfer path approach has been implemented by Siemens PLM (2015) software evaluating similarities in frequency content between different parts of a complex system. In hydraulic applications, frequencies that are present in one domain such as the FBN may not propagate into the structure very strongly and hence may not be important factors in the SBN or ABN. Likewise, the resonant frequencies of structures and geometry of the system (such as fluid volume harmonics) may play a large role in the total ABN radiated due to resonant behavior. The present work seeks to build on those efforts and combine

with techniques previously presented in order to gain a cohesive picture of noise propagation using standard instrumentation and new data processing methods. This allows for a simple and fast analysis to extract more detailed information about the performance of the system than typically used methods.

The experimental method for noise transfer path analysis was developed and tested on a simple hydraulic system composed of reference external gear pump #1, attached lines, and loading valve. Pressure oscillations in the working fluid are measured at the outlet of the pump. Surface vibrations are measured at multiple locations on the pump and connected system. Finally, the radiated air-borne noise is measured at a fixed distance from the pump. A post-processing algorithm was developed to identify key frequency features present in each domain as well as the transmission between different physical domains. The main outcomes of this research consists of a method to separate the contributions of fluid-borne noise or structure-borne noise to the overall air-borne noise emissions of the unit or system. The method developed for EGMs has general applicability to many different fields, and results allow for separation of the different noise contributions and better understanding of the overall noise emissions.

Measuring noise sources and transmission in the domains of the fluid, structure, and air can give deeper insight. The change in frequency content as the sound propagates through the system can then be better understood. The three domains are on different scales and units. On the fluid side, the oscillations are on the order of 1 bar, or 10^5 Pa. The structural vibrations range up to 20 m/s^2 while the measured air pressure oscillations range up to only 2 Pa.

As part of the work previously shown, the modal frequencies can be estimated using finite element solvers or analytical methods. Also, from previous research, the system and structural harmonics of the pump and the attached system can be estimated. An analytical estimation of the delivery fluid volume harmonics and the structural response of the attached lines on the outlet was calculated and shown in Figure 3.38. Predicted resonant frequencies for the Reference Pump #1 geometry such as the internal plates for pressure compensation, the gears, and the pump body itself are also shown in Figure 3.33.

The pressure and force loading due to the pump operation applied on the external system occur in an oscillatory way most strongly in the low frequency range below 2 kHz from multiples of the shaft speed and the number of pumping chambers. However for Reference Pump #1, the structural resonances of the body of the pump and the internal components are not expected to have a large effect until frequencies above 4 kHz. The simple system attached to the pump including the fluid in a 1m pipe and the structure of the steel pipe do resonate at frequencies close to the excitation frequencies and are expected to have a large effect on the result.

The excitation of the system and structures occurs in two primary ways. First, the modal interaction between the forces and the natural modes of the system and structures at their resonant frequencies. The second is the forced response where the system is responding at the forcing frequencies according to the impedance of the structures. This study attempts to simplify the investigation of the system performance by analyzing the measured frequency response in different physical domains according to the expected response. This includes comparing the measured results both to the expected excitation frequencies coming out of the oscillatory performance of the machine, and also comparing to the expected resonant response of different parts of the system.

The investigation of these effects allows for quantitative definition of what frequencies in the FBN, SBN and ABN strongly correlate to each other, as well as what frequencies do not strongly correlate across domains. This makes analysis of the contribution and separation of different noise effects possible.

5.2 Data Processing Approach

The approach is directed at the motivation for the research, to better understand the sound generation and propagation from sources to the environment. This is accomplished by data processing methods on noise measured in each domain. The main idea of the approach is dividing each iBN frequency component of the measured noise in the working fluid, structure, or air domains (that is, the FBN, SBN, or ABN) with the corresponding frequency components in a different domain in order to better understand correlations and anti-correlations between noise and vibration across different physical domains. The

experiments are described in the next section, but the main detail of the measurements includes the Reference Pump #1 along with an attached steel pipe at the delivery side. Measurements representative of the FBN, SBN and ABN were taken of the fluid pressure at the outlet, the structural surface vibration on the pump and lines surfaces, and the radiated sound pressure. These were recorded for a large range of operating conditions on the reference test circuit.

The recorded analog voltages were scaled according to the specified sensitivity of each equipment which resulted in pressure and acceleration ripples with approximate ranges of 0 to 10 bar for the FBN, 0 to 20 m/s^2 for the SBN, and 0 to 2 Pa for the ABN. The data is processed in several ways according to the following steps.

5.2.1 Fourier transform

For comparing between results, one second of data x_{iraw} is taken for each set iBN which stands for a measurement in either the FBN, SBN, or ABN domains used in the fast Fourier transform (FFT). Since there are three different sampling rates FS, taking the same period of data for all three domains yields the same amount of signal energy for the Fourier transform.

Each time domain signal is centered on a mean value of zero.

$$x_i = x_{raw} - mean(x_{raw}) \tag{5.1}$$

The FFT is accomplished in MATLAB® without zero padding in order to control the output frequency resolution to the required specification. No windowing was included as the signal is highly periodic and the period is of sufficient length to minimize end effects. The amplitude was calculated as the absolute value of the FFT divided by the length of the signal vector.

$$A_{iBN} = \left|\frac{fft(x_i)}{NFFT_i}\right| \tag{5.2}$$

The frequency vector can also be easily calculated as

$$f_{iBN} = \frac{FS_i}{2} linspace\left(0,1,\frac{NFFT_i}{2}+1\right) \tag{5.3}$$

Which is a linear frequency vector between zero and the Nyquist frequency at a frequency resolution of the Nyquist frequency divided by the number of points in the time

vector. When this is done for the period T time samples, this calculates the magnitude of the frequency vector at 1/T resolution with the same scaling for all three different domain measurements, even though they were recorded at different sample rates. Since small differences in sample rate can occur between different experimental setups despite system design, this is overcome by reading the data, calculating the sampling frequency from an average of the time domain increments, and then using the calculated sample frequency to define the length of one second of data.

5.2.2 Power spectral density

For displaying the results and calculating signal power more accurately, Welch's power spectral density (PSD) estimate can also be used. In this case, the time domain signal was segmented into eight partitions zero padded out to next higher power of two with 50% overlap. A symmetric hamming window of the segment length is applied to each partition before zero padding. This was accomplished using the MATLAB® according to the recommended parameters. The same frequency function is equivalent to the autocorrelation function of the Fourier transform of the signal.

$$P_{iBN} = A_{iBN}A^*{}_{iBN} \tag{5.4}$$

The PSD is then converted into decibel form

$$P_{iBN,dB} = 20log\left(\frac{P_{iBN}}{{p_{ref}}^2}\right) \tag{5.5}$$

Where the values are scaled according to a chosen value for reference power.

5.2.3 Cross-correlation

The cross-correlation function demonstrates the similarity in noise frequency between the internal pressure ripples, structural vibrations, and airborne noise for hydraulic units. Using the frequency spectra calculated using the Fourier transform, the similarity of the two spectra can be found using the MATLAB® cross-correlation function on the spectra.

$$Pcorr_{iBN,jBN} = xcorr(A_{iBN}, A_{jBN}) \tag{5.6}$$

Only frequency content that is shared between both signals will be strongly present in the cross-correlation.

5.2.4 Anti-correlation

The previous step attempts to emphasize the influence of shared frequency content between two signals, but additional knowledge can be gained by instead removing the shared frequency content. This step seeks to create a function in frequency that is independent of the shared frequency content between two signals. For example, to remove those frequencies from the ABN which are being directly driven by the FBN frequencies in the pump.

The different frequency spectra calculated by the FFT are scaled to the same relative magnitudes. The same frequency resolution was forced, and a chosen frequency band can be taken across all the data to decrease the resolution of the result if desired. This has the positive effect by reducing the influence small mismatches in frequency have on the scaled results when comparing two different measurements. The transfer equation simply takes the band averaged frequency spectra Ab_{iBN} and divides by the spectra from a different domain measurement.

$$Tp_{i/j} = \frac{Ab_{iBN}}{Ab_{jBN}} \tag{5.7}$$

This allows for reducing the impact of shared frequency content between the two domains. Essentially calculating an averaged anti-correlation function between the two signal's frequency spectra. This simplified approach has the negative result of negating the phase-dependent aspects of the compared frequency spectra. However, the goal of the paper is to investigate the similarities and differences between physical domains, and the simplified anti-correlation approach allows for separation of the potential paths for energy to propagate out of the system as noise. The remaining calculated frequency content is that which is not strongly correlated between the two domains, and a sum of this function across multiple operating conditions is used to determine the influence of different components in the system on the transfer path of noise.

5.3 Experimental Setup

The experiments were completed on the Multi-Purpose Test Rig at Purdue's Maha Fluid Power Research Center. The hydraulic schematic circuit and locations of sensors are shown in Figure 5.1. The Multi-Purpose Test Rig allows for easier testing of more operation conditions for open circuit designs.

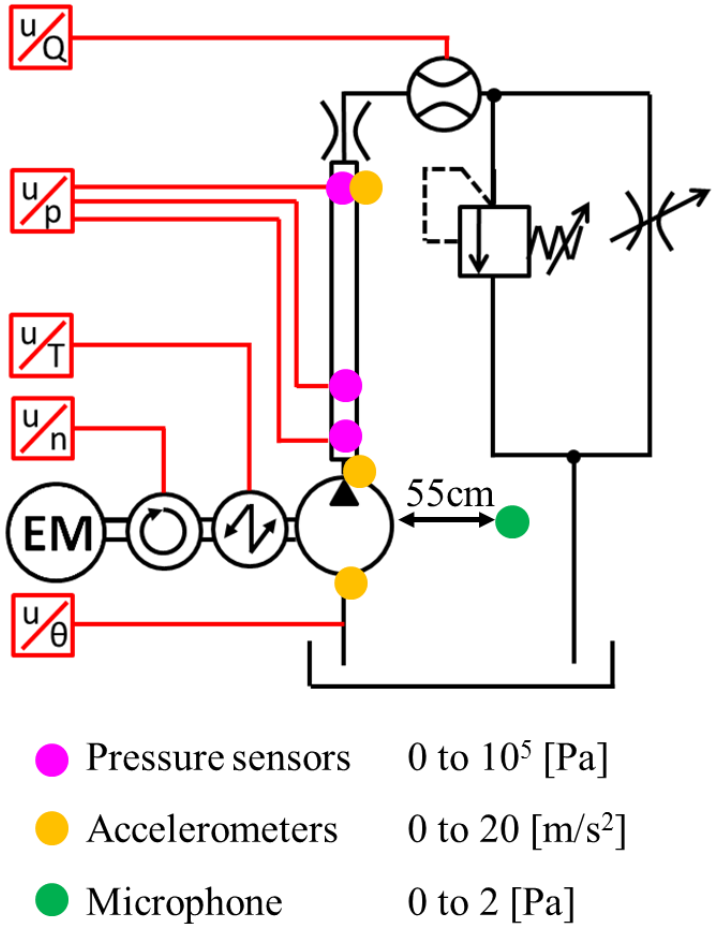

Figure 5.1 Experimental test schematic

A picture of the test setup with the pressure sensors, accelerometers, and microphone locations highlighted is shown in Figure 5.2.

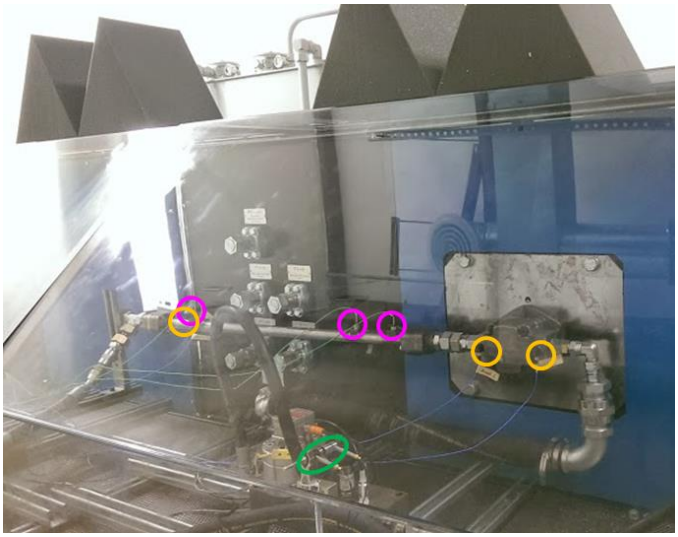

Figure 5.2 Experimental test setup

There are three pressure sensors in the steel pipe; an accelerometer on the pump body near the inlet, outlet, and at the end of the attached steel pipe; and a microphone at 55 cm from the pump. The frequency content was measured during a range of operation with a 100 bar outlet pressure in the steel pipe. The measured values from the different sensors is shown in the following figures.

The test setup is highly flexible and allows for rapid testing of different pump prototypes and system architectures. The test setup shown here is used for quantifying pump performance for comparison to model results predicting the outlet pressure ripple of the pump. Initially, total sound power measurements were completed in the semi-anechoic chamber as discussed in Chapter 4. Those measurements indicated that a single microphone measurement was sufficient for analyzing the frequency content of the radiated ABN. Measuring the ABN at a single location in a reverberant space limits the analysis that completed using the data due to the large contributions of the room geometry. The location directly pointed at the pump at 55 cm distance was chosen as it is as far away from the nearfield of the pump as allowed by the enclosure without being in close proximity to other components. However, comparisons between ABN measurements in the semi-anechoic space compared to the reverberant space showed good agreement in terms of frequency content. The ease of measuring the large number of operation conditions allowed by the single-location microphone was compared as a trade-off allowing the reduced robustness

of the ABN measuring methods. Additionally, the pump is now run in the design way drawing fluid directly from the tank, so the effect of the supply system is reduced compared to the experimental setup in Chapter 4. Adding sensors for measuring not only the FBN, but also the SBN and ABN allows for the deeper investigation of transfer paths and frequency-based correlations shown in the following section. The noise in three domains was recorded using the equipment shown in Table 5.1.

Table 5.1: Sound measurement equipment

Item Type	Description
Pressure sensors	Kistler type 603B1, 0-1000 bar, accuracy 1.1%FS Sampled at 15kS/s
Accelerometers	Three locations, 3-axis, PCB model 356A16, sensitivity 10mV/(m/s^2) Sampled at 15kS/s
Sound intensity probe	GRAS, three microphones Type 40A0 – Sensitivity 0.2 dB ref 2·10-5 Pa, ½“ diameter Sampled at 52kS/s GRAS, Type 26CB, ¼“ diameter pre-amplifier

An operating range of 500 rpm to 2100 rpm was considered with 100 bar pressure at the pump outlet set using the variable orifice and fixed orifice plate. The inlet oil temperature was held to 50ºC.

5.4 Measured Results

The FBN time signal is showing the ripple in pressure in the pipe caused by each gear tooth passing into the meshing zone. Show in Figure 5.3, three distinct ripples are shown which corresponds to ¼ of a shaft revolution in 0.015 s for the 13 tooth pump according to:

$$f_n = \frac{n \cdot nc \cdot rpm_{shaft}}{60} \tag{5.8}$$

For n higher multiples of the number of chambers multiplied by the shaft speed. Example time domain measured signals for each measurement of FBN, SBN, and ABN are shown in the following figures for a fixed operating condition of 1000 rpm 100 bar. The time domain signals at the reference operating condition shown below have been scaled to a reference value in each domain according to a fixed root-mean-square value to equalize the different domain signals.

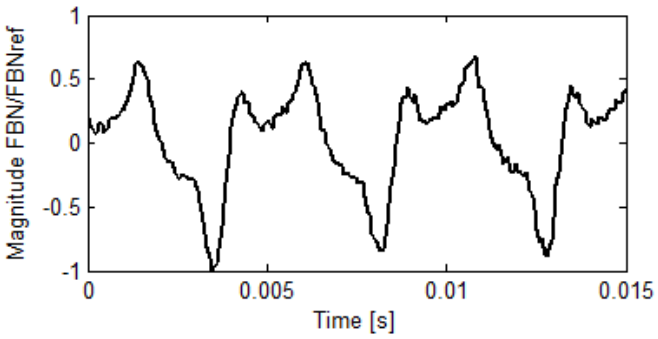

Figure 5.3 FBN time signal

The time domain signal for the same period showing the measured SBN is in Figure 5.4. This signal is dominated by higher frequency signal content such that the FBN frequencies are difficult to see in the time signal.

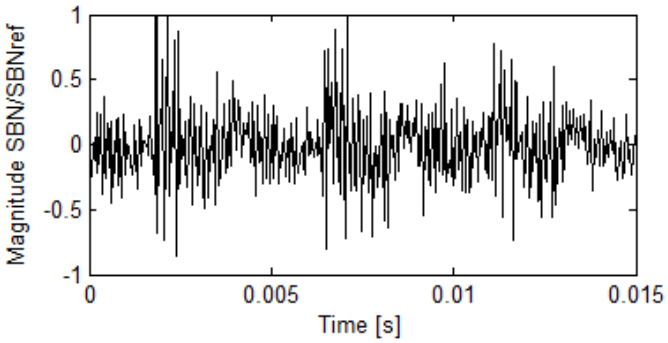

Figure 5.4 SBN time signal

Finally, the measured ABN for the same period is shown in Figure 5.5. The ripple of the main FBN frequency is clearly shown again, but there are many additional frequencies that were not present in the FBN.

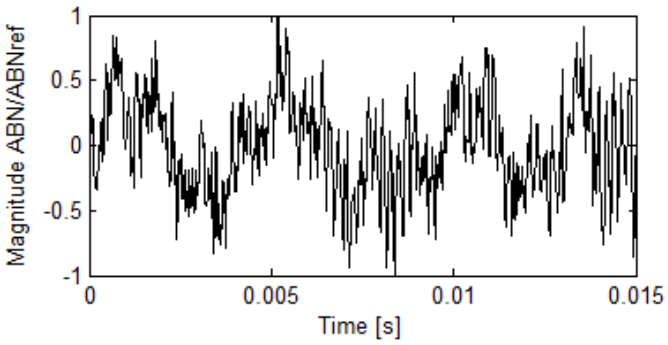

Figure 5.5 ABN time signal

The frequency spectra for one second time samples were found using the FFT as discussed in the previous sections. They are shown after the FFT was applied for the three time domain signals in the three previous example figures.

Again, the FBN signal is the cleanest as expected from the time domain, with sharp peaks in the frequency spectra corresponding to the integer multiples of the pump frequencies. The first peak reaches a value of 0.2 on the magnitude axis. The lower vertical axis range was selected for comparison with the figures following for SBN and ABN.

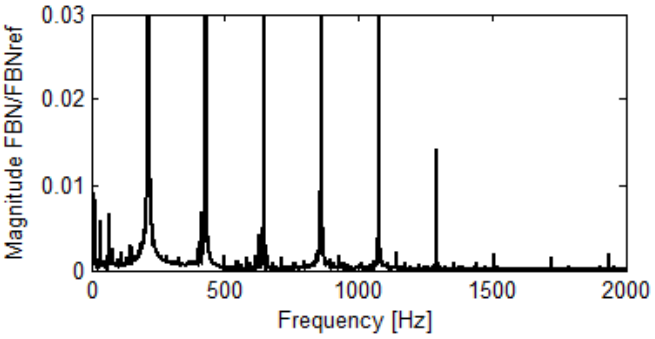

Figure 5.6 FBN frequency spectra

The spectra for the SBN is shown in Figure 5.7. Not shown in Figure 5.7 are the higher frequency contributions >2 kHz that are dominating the time signal in the 5 kHz to 10 kHz range. Even though the time domain in Figure 5.4 was not clearly matching the frequencies of the pump, the frequency spectra shows that the structure of the pump body is also vibrating at the frequencies it is being excited at. That is, mainly the same frequencies of the FBN are present in the SBN. However, the magnitudes of those frequencies compared to each other is different in the structure domain.

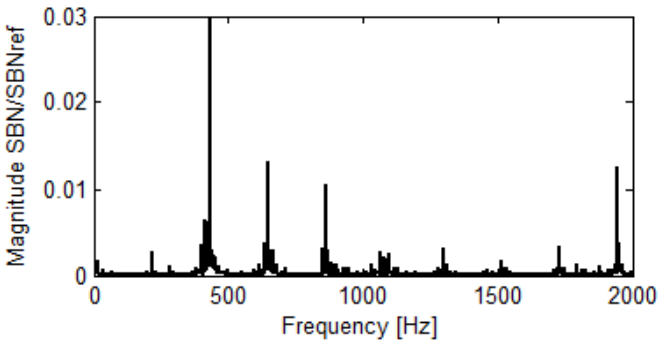

Figure 5.7 SBN frequency spectra

Similar results are shown in the spectra for the measured ABN in Figure 5.8. There are also additional large frequency contributions in the ABN which were not clearly present in the FBN or SBN. Similar to the FBN, the peak at 433 Hz reaches outside the figure bounds to 0.1 but the figure is zoomed in to show detail at lower magnitudes.

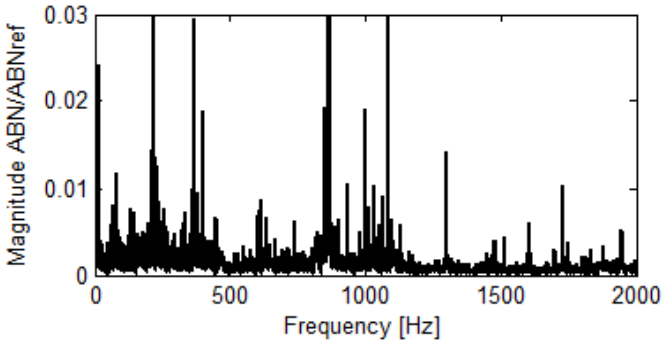

Figure 5.8 ABN frequency spectra

The goal of the following sections is to investigate the correlations between domains across a wide operating range as compared to the FFT shown for a single operating condition in the previous figures.

5.4.1 Power spectral density

As explained in the procedures, power spectral density (PSD) is time domain autocorrelation of each signal to identify repeating patterns and frequencies. At a single operating condition, these are very similar to the frequency spectra as shown in the previous section. However, when a large number of operating conditions, every 10rpm increment from 500rpm to 2100rpm, are combined together, a clearer picture of the overall machine performance can be seen as in Figure 5.9. The variation of speed test was chosen to be

repeated compared to the variation of pressure test which was also evaluated in Chapter 4 due to the interest in phenomena dependent on the variation of pump frequencies. Mainly, the same considerations can apply to different pump pressure levels, but mainly only the magnitude of the sound source is changing with pressure while in the speed variation test, the frequency of excitation is also changing.

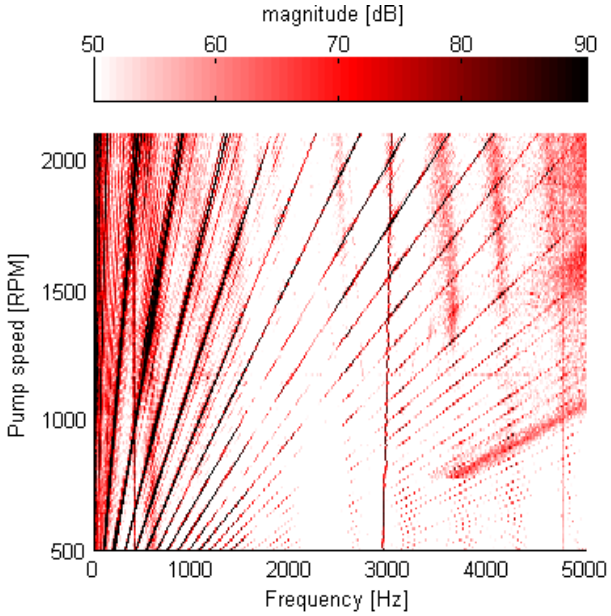

Figure 5.9 FBN PSD

System and structural frequencies can be seen as vertical lines in the measured FBN. Pump and shaft frequencies originate from (0,0) on the plot and are present at multiples of the shaft speed frequency and the number of pumping chambers according to equation 8. These occur as dark black and red angled lines at frequencies and overtones of the main pump frequency. The shaft frequency can now also be clearly seen at the far left of the figure as a dark black band, and overtones of the shaft frequency are also prevalent at all operating conditions. These occur at multiples of the shaft frequency in-between the main pump frequencies. Likewise, the PSD for the SBN is shown in Figure 5.10.

Stronger bands at high frequencies from the beginning of structural resonant modal behavior are shown in Figure 5.10. The figure shows the values from the pump casing accelerometer, but recorded measurements on the steel pipe showed even higher overall magnitudes due to interaction of pump excitation frequencies and pipe structural resonances.

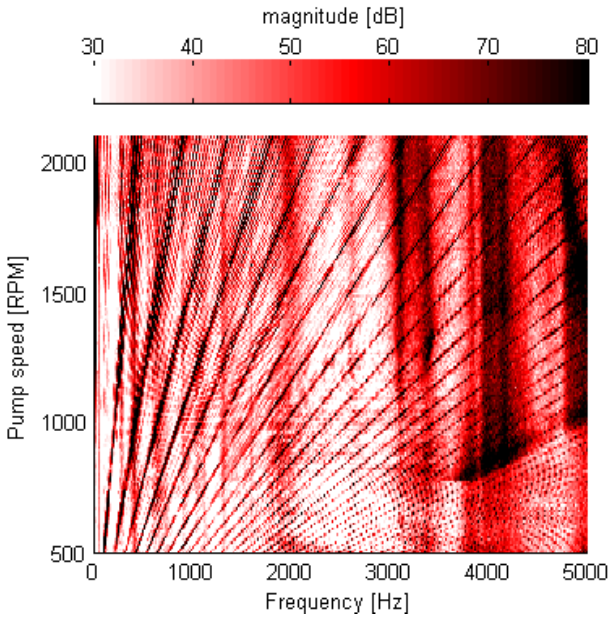

Figure 5.10 SBN PSD outlet accelerometer

The increase in higher frequency content in the SBN agrees with the expectation of structural resonances. The vibration response of the structure is a combination of the forced response due to the high forces exciting at low frequency, and the modal response of the structure at higher frequencies. The ABN PSD is shown in Figure 5.11.

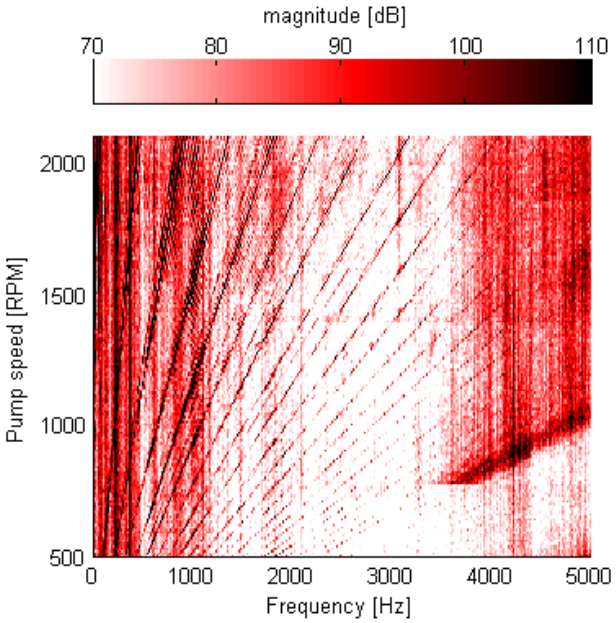

Figure 5.11 ABN PSD

Again, the power spectra of the ABN domain is very similar to the FBN and SBN. There are many more vertical bands present in the ABN than there were in the FBN, which is indicating the impact of the structural transfer path. The total measured response shows the clear impact of both the excitation frequencies and the modal response of the system. Comparing the raw power spectra of the three domains can be done visually, but the present research seeks to quantitatively determine correlations between matching and non-matching frequencies across all three domains.

5.4.2 Cross-correlation

The first step is to emphasize the similarities in frequency spectra using the cross-correlation function as described in the approach section. The cross-correlation compares the similarity in shared frequencies between two spectra from different measured domains. An example of this function at a single operating condition of 1000 rpm 100 bar is applied to the three different combinations of data is shown in Figure 5.12.

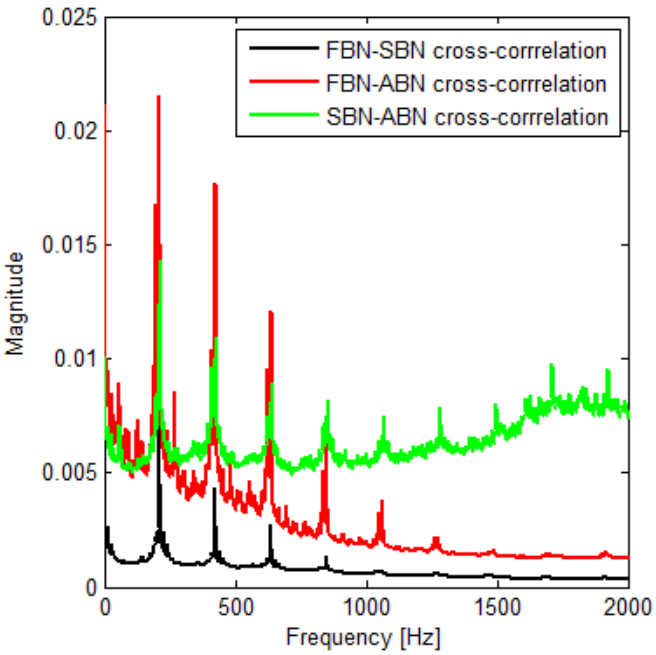

Figure 5.12 Cross-correlation example at 1000rpm

As shown in the figure, there is a very strong correlation between all three combinations of data at the multiples of the pump and shaft frequency every 217Hz. This means that below 2000Hz, the excitation frequencies coming from the pumping action of

the unit are strongly present not only in the working fluid, but also in the structure and radiating to the environment. Note that there is a very weak correlation between the FBN-SBN and FBN-ABN at frequencies higher than 1000Hz. This is because the higher frequency content is not present in the FBN, so there is no strong matching between the FBN and the other two domains at high frequency. Alternatively, there is strong matching of higher frequency noise between the SBN-ABN even at higher frequencies which indicates that higher frequency content in the ABN is correlating well with frequencies that are not present in the FBN. This means that traditional design optimization efforts that seek to minimize the radiated ABN by reducing the FBN alone are potentially failure-prone due to not considering important features in the structures of the system.

Figure 5.12 shows just a slice of the operating range at 1000rpm. Instead, the entire operating range from 500rpm to 2100rpm is shown in the next three figures. A linear comparison was used since a logarithmic display of the data does emphasize the difference in magnitudes when displayed in the following waterfall plots.

The cross-correlation function comparing the FBN and SBN frequency spectra at the entire operating range is shown in Figure 5.13.

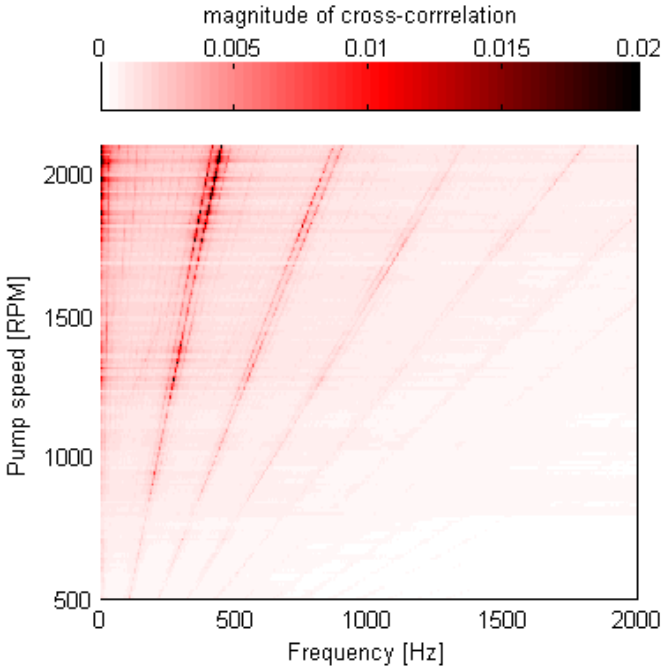

Figure 5.13 FBN-SBN cross-correlation function

As the figure shows and was repeated in the example measurement in Figure 5.12, there is almost no correlation except at the pump frequencies since those are the only frequencies present in the FBN. The correlation between FBN and SBN steeply drops off above 1 kHz. Values below 0.01 correspond to very little correlation in the data between domains.

Likewise, the FBN-ABN comparison shown in Figure 5.14 is nearly identical to the previous figure since the only shared frequencies between the FBN and ABN are those which are directly excited by the pump operation. This reinforces that reducing the pump pressure ripple through design changes will have an effect on the radiated ABN at the frequencies that the pump is excited at since there is a strong correlation between them. However, this picture is still incomplete since it does not consider the influence at other frequencies.

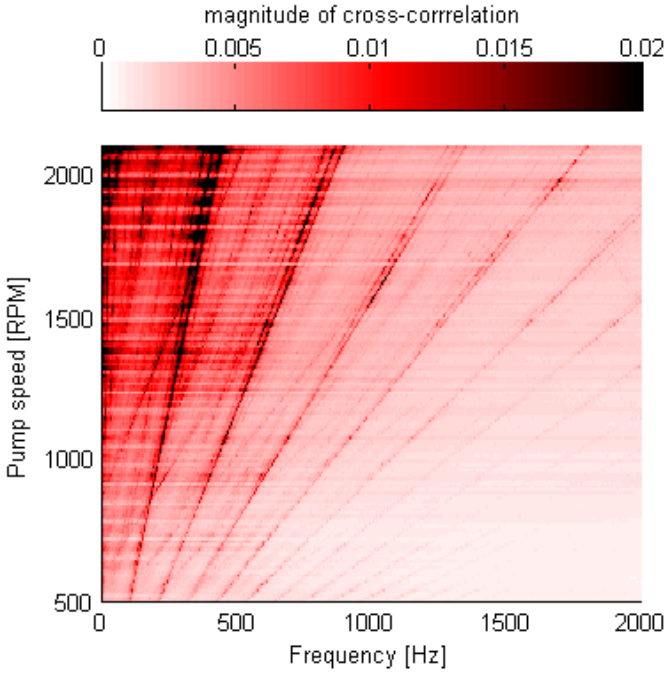

Figure 5.14 FBN-ABN cross-correlation function

Finally, the SBN-ABN correlation function is shown in Figure 5.15. This now shows that there are dark regions of the graph at higher frequencies due to the presence of higher frequency noise in both signals. Unlike the previous two figures, the correlation between SBN and ABN does not decrease as frequency increases. Instead, there is still a

strong correlation between the SBN and ABN at a wide range of frequencies that includes much higher multiples of the shaft and pump frequencies than was seen in Figure 5.13 and Figure 5.14.

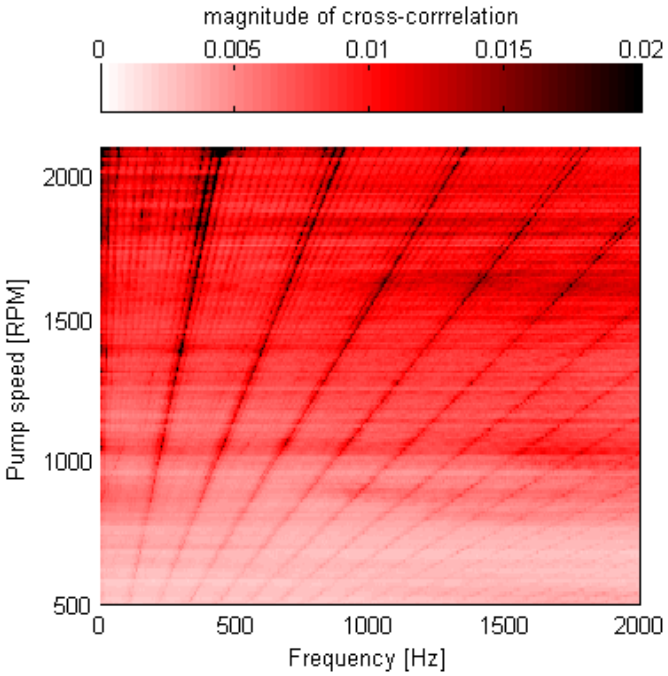

Figure 5.15 SBN-ABN cross-correlation function

The cross-correlation functions emphasize the similarity in noise frequency content between different measured domains. They succeed in removing the extra frequencies which are present in only one domain. The emphasis here is that when considering the FBN domain, the main shared frequencies with either the SBN or ABN domains are only the frequencies coming directly from the pump and shaft speeds. For example if there was a fluid harmonic behavior in the pipe, that would show up as a vertical band in the FBN spectra at all operating speeds. If that harmonic behavior also was exciting the structure, the same vertical band would appear in the SBN or ABN domains. The cross-correlation function would then also exhibit the same frequency behavior. The lack of such vertical bands in the cross-correlation functions indicates that the transmission of noise from the FBN domain to the structure is heavily dominated by the pump frequencies instead on a resonant excitation behavior. On the other side, the presence of higher frequencies in the SBN-ABN correlation shows that a large range of different frequencies and noise paths are now being driven as they transfer through the structures and out to the environment.

5.4.3 Anti-correlation

Removing frequency content through anti-correlation cancelling allows for identification of frequencies that do not correlate across different noise and vibration domains. This is the inverse of the goals of the previous section. The first step is removing the FBN from the ABN frequency spectra using the procedure described in the approach section. The FBN frequency content due to the shaft and pump frequencies are now at a minimum instead of at a peak, and bands appear where there are frequencies in the ABN that do not correlate as strongly with the FBN. This seeks to emphasize frequency features that do not correlate with the pump driving frequencies. The figure is shown only to 2000Hz in order to show more detail in the low frequency range. The algorithm was applied at all the operating conditions and the result is shown in Figure 5.16.

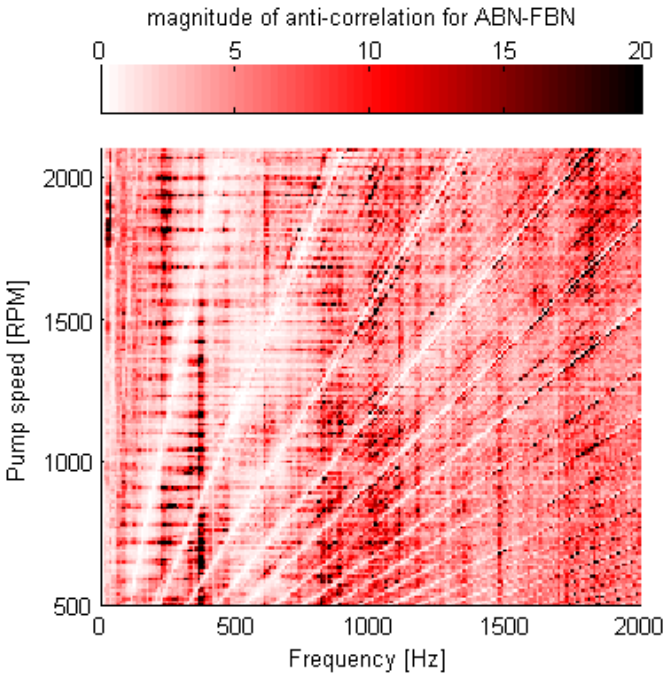

Figure 5.16 ABN with FBN removed

The previous figure shows strong trends in vertical black lines in the plot. Essentially, there is now very little speed-dependent (angled lines) portion of the signal remaining. This component has been removed along with the pump frequencies. The emphasis is now on the non-speed-dependent features present in the measured noise.

Furthermore, most of the remaining frequency features present in Figure 5.16 are present at all operating speeds. The speed dependence can finally be removed by summing along the vertical pump speed axis results in Figure 5.17 to create a single speed-independent function. This function shows a summary of what frequency content in present most strongly in the ABN when the internal loading condition of the FBN removed. The remaining frequencies are broad spectrum noise frequencies. The tallest peaks remaining in the low frequency range were compared with the expected geometry of the measurement space where λ~1 m standing waves in the air which occurs at ~400 Hz.

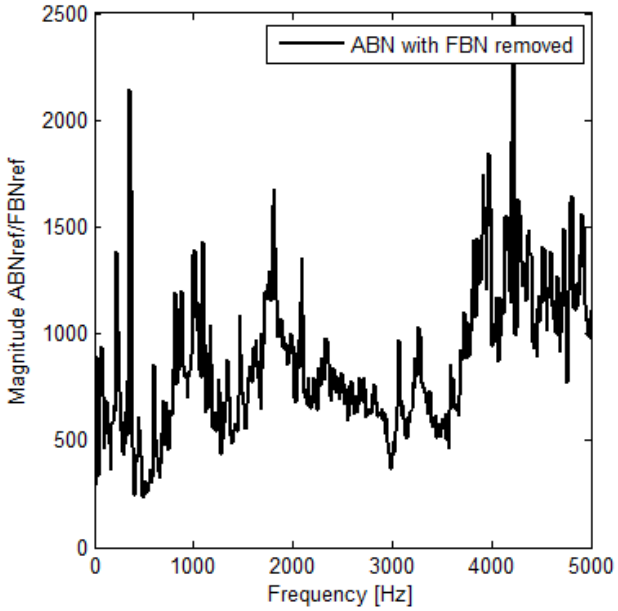

Figure 5.17 ABN with FBN removed

The individual locations of large peaks in the anti-correlation function shows which lower impedance transfer paths are propagating noise from the sources inside the pump out to the environment as well as other system resonances that are being excited.

Likewise, the same method was used to remove the FBN frequencies from the SBN as shown in Figure 5.18.

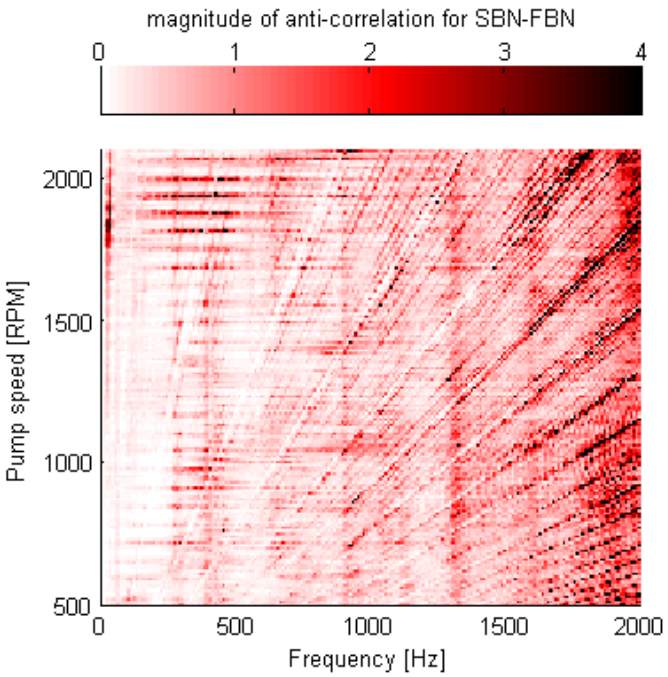

Figure 5.18 SBN with FBN removed

Very strong black vertical bands now appear across the operating range, and again the data can now be summed across the vertical speed axis in order to quantify a speed-independent function of the energy transfer from the internal fluid sources into the structures. Two different accelerometer locations were considered for the summed function shown in Figure 5.19 (the pump case, and on the line).

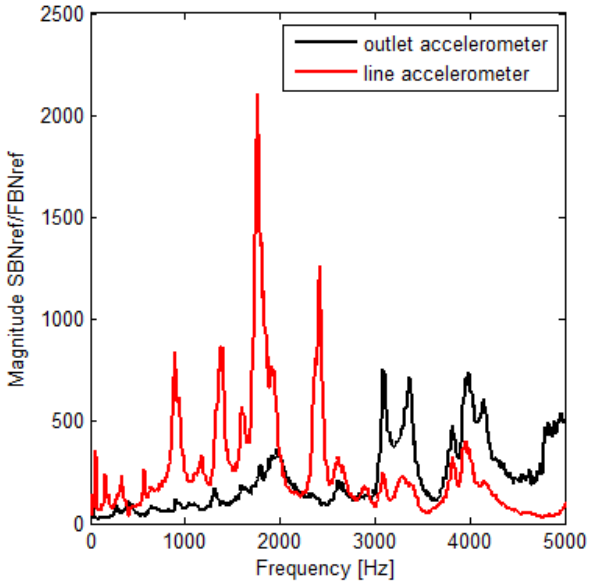

Figure 5.19 SBN with FBN removed

There is very little low frequency content remaining when comparing the case accelerometer data SBN – FBN. Therefore the pump is not dominantly vibrating in a resonant way at low frequencies. However, with the FBN frequencies removed from the accelerometer data taken at the end of the steel pipe, there are very strong peaks that correlate well with the predicted structural resonances of the steel pipe that are shown in Figure 3.38.

The tall peaks in line accelerometer data show that the pipe is vibrating at resonant frequencies which are excited at all operating conditions. The presence of these peaks was not obvious in the raw data, but the anti-correlation function allows for the identification of the path that energy takes from source to receiver as well as identification of which sources and transmission paths are effecting the result the most. This particular result shows that the geometry of the system and lines has a large impact on how noise is transmitting from the sources out to the environment. A noise reduction optimization that does not take into account the effect of the system may not be as effective.

The final comparison is shown in Figure 5.20 for the ABN with the SBN removed considering the same two different accelerometer locations for the SBN. This is showing what frequencies are present in the ABN that do not correlate with measured SBN frequencies.

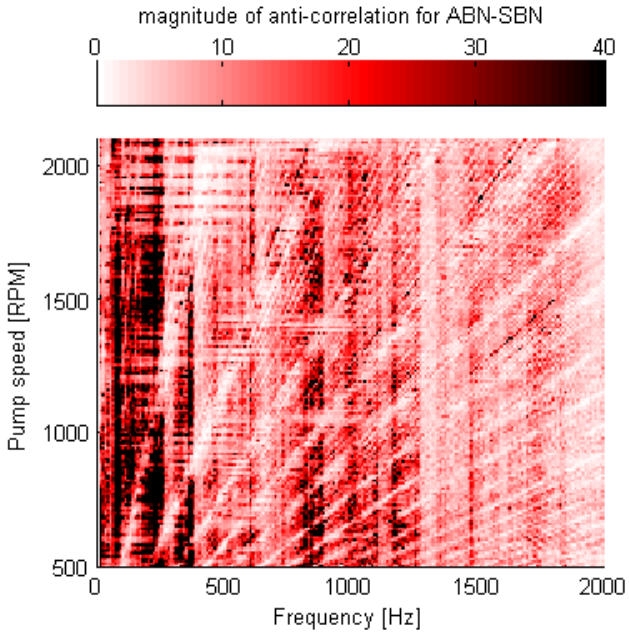

Figure 5.20 ABN with SBN removed

A strong correlation at the low frequencies is shown for the case accelerometer, but as in the summary function in Figure 5.21, the higher frequencies do not have matching for the ABN compared to the line accelerometer data since the steel pipe is strongly vibrating at frequencies near the predicted resonances. The strong correlation between signals results in a small magnitude for the black line in Fig. 23. Since the higher frequencies are present in both the measured ABN as well as the line accelerometer, they are therefore not present in the anti-correlation function. These frequencies are not a large contributors to radiated ABN above 2 kHz while they are one of the highest contributors at frequencies below 1 kHz.

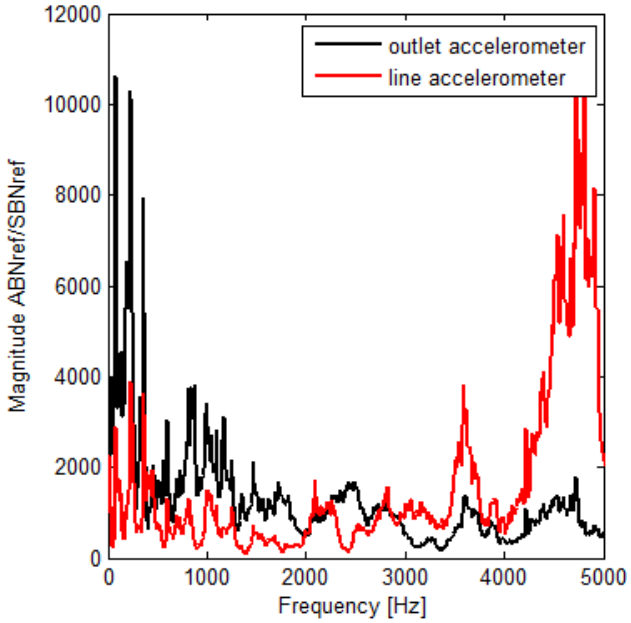

Figure 5.21 ABN with SBN removed

Less high frequency content remains in the ABN-SBN function than in the ABN-FBN anti-correlation. This means that high frequencies waves are present in SBN, but not FBN. From the estimated resonances in Fig. 2, this is the expected result since the pump structure has much higher resonant frequencies due to thickness and size of the structure. Even though the excitation frequencies are mainly below 1 kHz, the higher multiples of the FBN are still exciting higher resonances in the structure of the lines and the pump body which appear in the SBN and ABN measurements.

The cross-correlation functions show how similar the frequency content is across the three measured domains. However, the cancelling anti-correlation algorithm allows for

identification of system and structural influences that are not apparent from the raw data. Summing across a wide range of operating conditions yields a quantitative speed-independent function of the transfer paths for key sources of noise. Comparing the three anti-correlation functions shows that the pipe structure is vibrating strongly in resonance and excited by the pump frequencies. The presence of strong peaks in the SBN-FBN plot and the ABE-FBN plot, but not the ABN-SBN plot shows that there is a strong transfer path between the pipe vibration and the air-borne noise despite this frequency content not directly correlating to the FBN.

5.5 Conclusions on New Data Analysis Methods

Experimental techniques and data processing algorithms were developed for use in identifying important noise features of the hydraulic system. Individually, measuring the pressure ripple generated by the pump under load has previously been used to validate the EGP model developed at Maha Fluid Power Research Center and to aid in design for reducing the sources of FBN in the system. Vibration in the steel pipe used to characterize the FBN according to the ISO standard could be influenced by resonances of both the fluid inside the pipe and the pipe structure. The results show that even if the primary pump frequency magnitude is reduced, higher frequency noise sources may be introduced by this method, the resulting noise propagation through the system will excite higher frequency resonances more strongly and result in overall larger surface vibration and ABN radiation. Measuring the surface vibration of the pump and lines sheds light on the influence structural and system considerations have on the pump operation and radiated noise, and allows for smarter optimization and design of new quieter pumping units. Measuring the radiated sound pressure is used to validate noise models and determine if design changes accomplished the desired goals of quieter systems.

Combining all three domains of measurements gives a more detailed picture than any one domain by itself. The new experimental and data processing techniques point out the direction for models so that the most important noise sources and propagation paths can be simulated more efficiently. The key potential future applications of this methodology is to improve system designs through structural modifications or targeted

operating ranges. It also allows for new more efficient and accurate modeling techniques that would be not be possible without the complementary experimental technique.

Overall, this technique and data processing algorithm expands the idea of transfer-path analysis in a new direction and applies it on hydraulic components and systems. Using this analysis directly aids in the improvement of hydraulic components and similar analysis can be used to better understand the transmission of noise in many different applications.

6. MULTI-DOMAIN NOISE CAVITATION STUDY

An additional case study was investigated comparing the relative magnitudes of pressure ripple on the inlet and outlet sides of the pump using Reference Pump #3 as shown in Figure 6.1. Beyond just the magnitudes, the effect on the pump noise is evaluated.

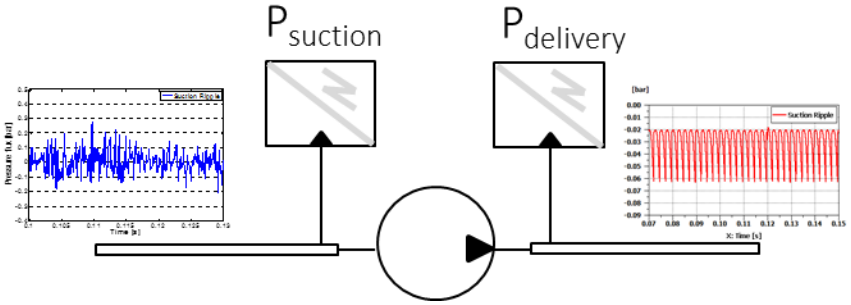

Figure 6.1 Inlet vs outlet ripple comparison

The purpose of this chapter is to answer the following questions. First, how much is it possible to change the inlet pressure ripple through design variations? This is tested through an extreme design change to the lateral grooves shown in Figure 6.2.

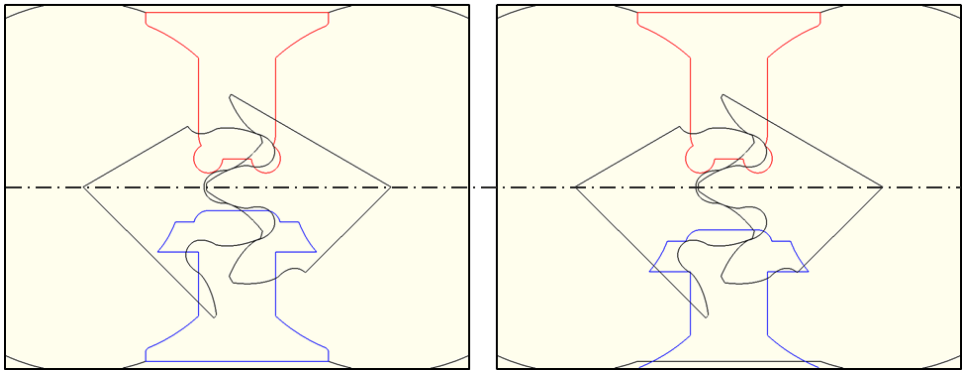

Figure 6.2 Baseline vs design made for increased suction ripple.

This modification to the standard design for Reference Pump #3 moves the inlet-side groove down by an order of 0.001m from the original placement as shown. This

extreme design change was selected in order to evaluate and quantify the performance of all cases between the optimal one and the extreme bad design. Where the bad design is intended to induce localized cavitation as well as greatly increase inlet flow ripple.

The second question to be answer is what is the possible impact that such a variation in the inlet ripple may have on the radiated ABN? And finally, is the model sensitive to the inlet flow ripple and what changes are predicted in the radiated noise for a similar design change.

6.1 Effect of suction groove placement

The suction groove connection timing of the pump, shown in blue in Figure 6.3, while the delivery groove is shown in red.

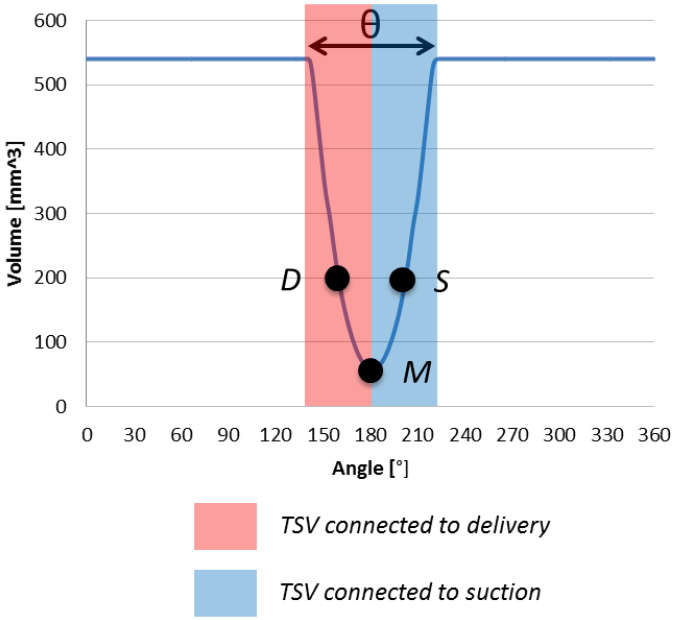

Figure 6.3 Typical groove connection timing for an EGP.

Typically, as found in the standard design for Reference Pump #3, the transition point between the suction and delivery grooves occurs near the minimum point in the TSV during the meshing zone. Instead, the new design of the pump for cavitation and inlet ripple offsets the inlet groove and creates a significant angle where the TSV is changing in volume show in Figure 6.4, but is also trapped, as indicated by points D and S where the gear tooth contact traps the fluid inside the TSV. Since the volume is rapidly changing, the pressure

in the pumping chamber drops rapidly which can create localized cavitation. Also, once the groove does open up to the suction, the current low pressure in the chamber causes fluid to enter the TSV at high velocity thus also inducing higher inlet flow ripple.

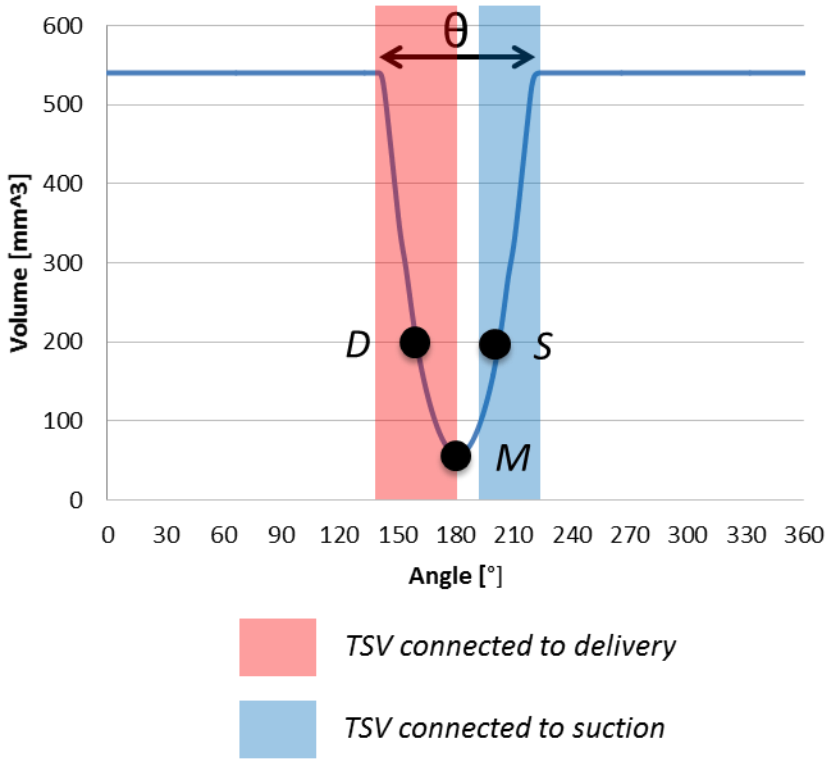

Figure 6.4 Modified groove timing for pump designed for inlet cavitation

Since the modification is limited to the suction side groove, the goal of this design modification is to introduce a large disturbance on the inlet side of the pump while keeping the outlet side of the pump unchanged.

6.2 Experimental setup

The experimental setup was the same with respect to the multi-domain noise propagation study shown in the previous chapter with the addition of one pressure sensor was moved from the outlet pipe to a new 1 meter long steel pipe on the inlet of the pump. This sensor was located at 0.1m from the inlet port of the pump. Also, the pump design was changed from Reference Pump #1 to Reference Pump #3. Please refer to chapter 5 for more details on the experimental setup.

6.3 Measurement results

The measured results for inlet pressure ripple with its mean value removed and its corresponding frequency spectra are shown in Figure 6.5. The pressure shown is taken from an operating condition of 1500 rpm and 200bar outlet pressure.

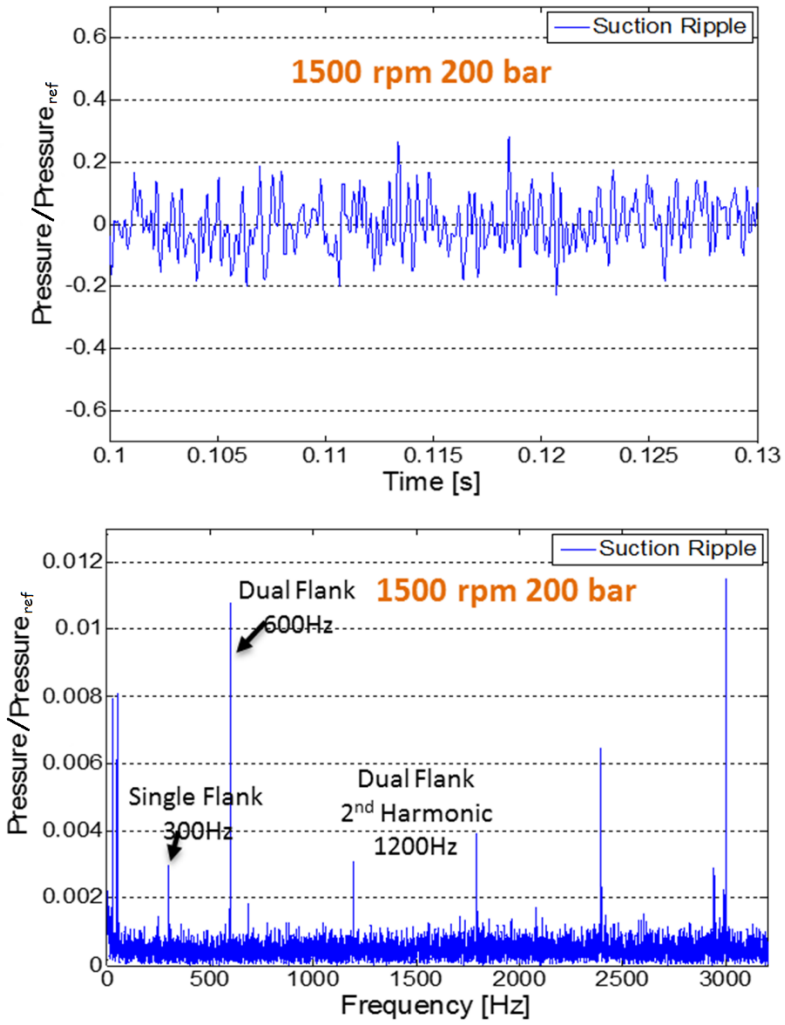

Figure 6.5 Inlet ripple (top) and FFT (bottom) for baseline pump.

There are clearly identifiable frequencies from the pump performance as well as the shaft frequency of the driving electric motor. The new design for Reference Pump #3 with the extreme placement of the suction grooves is shown in Figure 6.6.

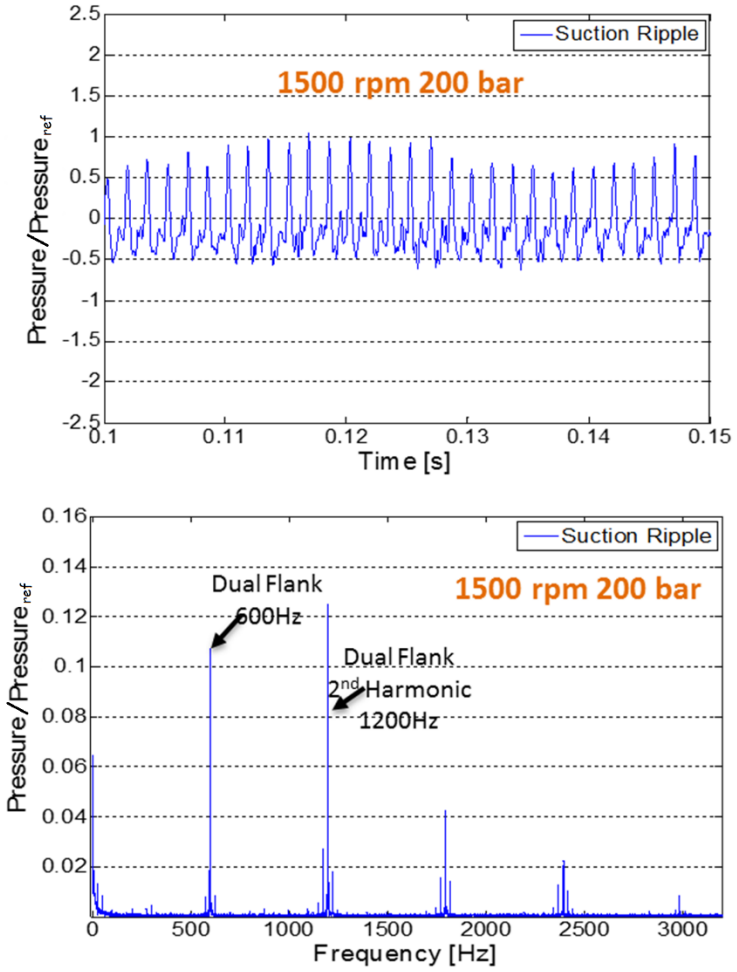

Figure 6.6 Inlet ripple (top) and FFT (bottom) for cavitation pump.

At the listed operating condition of 1500 rpm 200 bar, the inlet pressure ripple was successfully increase by an order of magnitude. The final consideration for whether the design modification was successful is to compare the outlet side pressure ripple as shown in Figure 6.7 for the operating condition of 2000 rpm 200 bar.

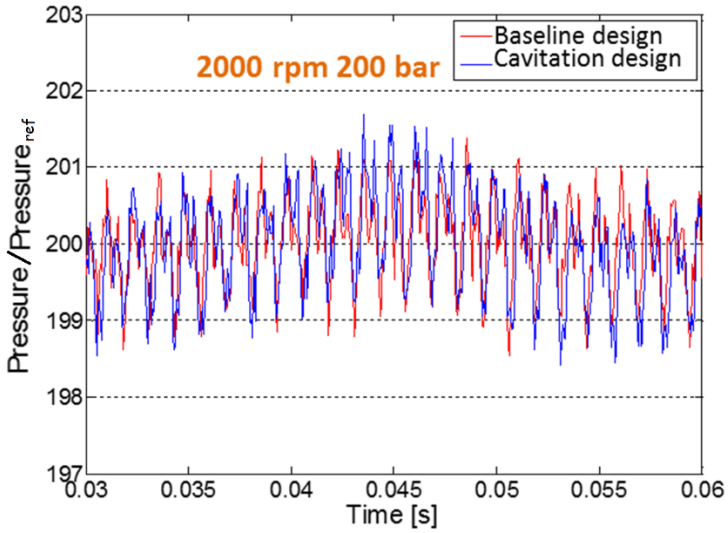

Figure 6.7 Time domain comparison of outlet ripples

This shows that the outlet pressure ripple is very similar between the two designs and that the modification to the suction groove which greatly changed the inlet performance of the pump did not have a large effect on the outlet side. This is confirmed in the frequency spectra shown in Figure 6.8 and Figure 6.9.

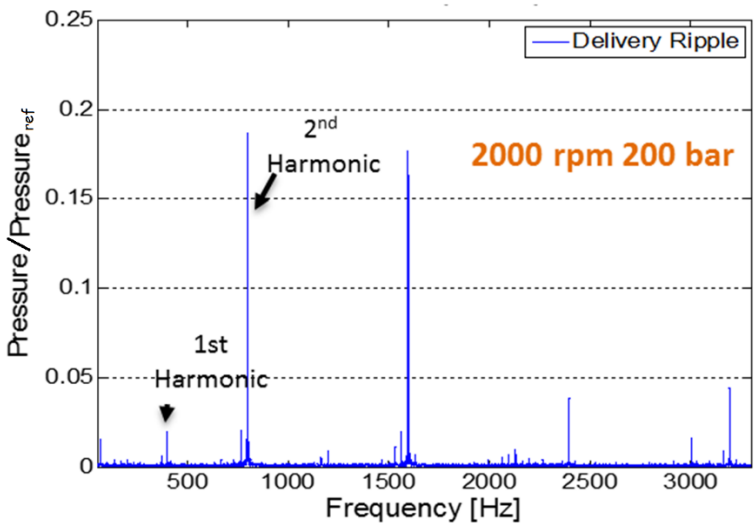

Figure 6.8 Comparison of FFT for outlet ripple for baseline pump.

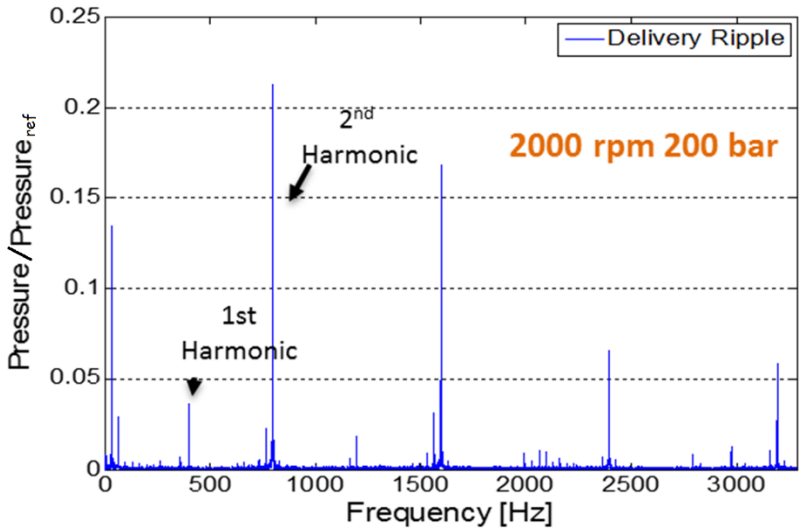

Figure 6.9 Comparison of FFT for outlet ripple for cavitation pump.

The next step is to leverage some of the techniques demonstrated in Chapter 4 and Chapter 5 in order to analyze the noise performance of the two different design in different physical noise domains, that is, the fluid, structure, and air. A fixed outlet pressure of 100 bar was selected, and the pump speed was carried on 50 rpm increments from 500 rpm through 2500 rpm. The comparison of the power spectral density (PSD) for the baseline design and the design with induced inlet flow ripple is shown in Figure 6.10 and Figure 6.11. All scales are taken with reference to the sound power ref of 1e-12 W. However, the fluid pressure data was taken in units of bar and this was preserved through the power spectra. This causes the measured fluid pressure data to be scaled by a factor of 10^5 compared to similar ABN power spectra. The difference is convenient since it places the three different domains on a similar range of decibels, while the important scaling to consider is the difference in decibels between measured signals in the same domain.

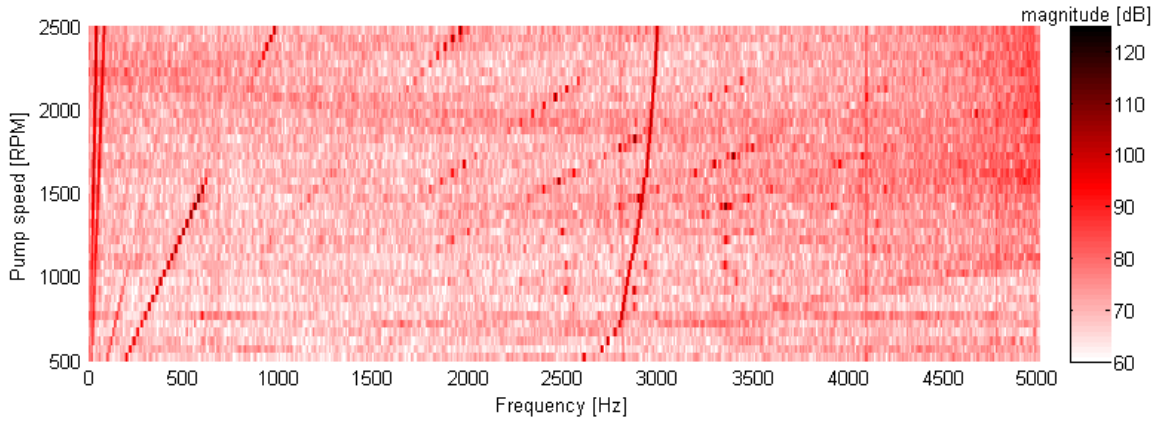

Figure 6.10 Inlet ripple PSD for baseline design

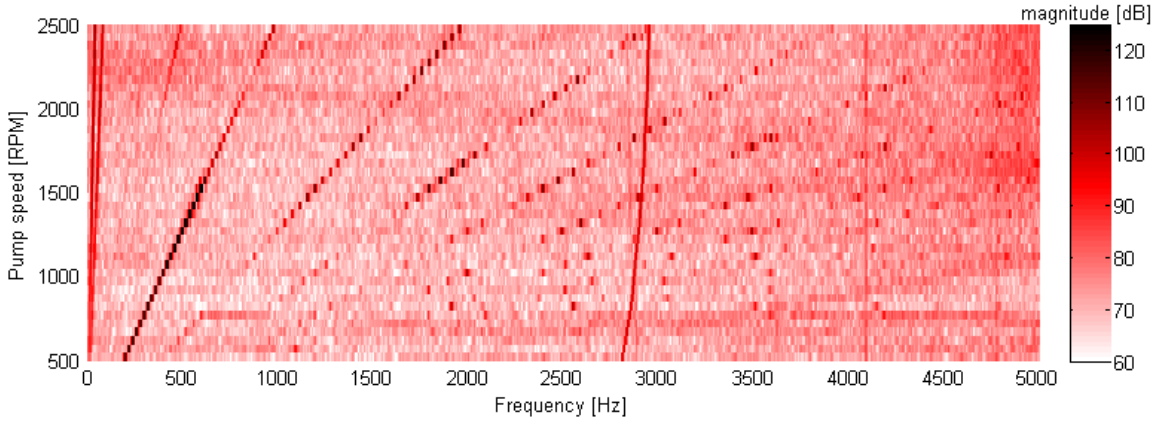

Figure 6.11 Inlet ripple PSD for cavitation design

The cavitation design shows a 30dB increase in inlet ripple for the primary pump frequency (dual flank) at all operating conditions. A very interesting region for the baseline pump is the range around 2000 rpm where the primary frequencies of the pump are not visible in the PSD. This indicates a performance regime where the inlet ripple is small enough to have very little effect on the noise coming from the EGP in operation.

The same plots for the measured outlet pressure ripple are shown in Figure 6.12 and Figure 6.13.

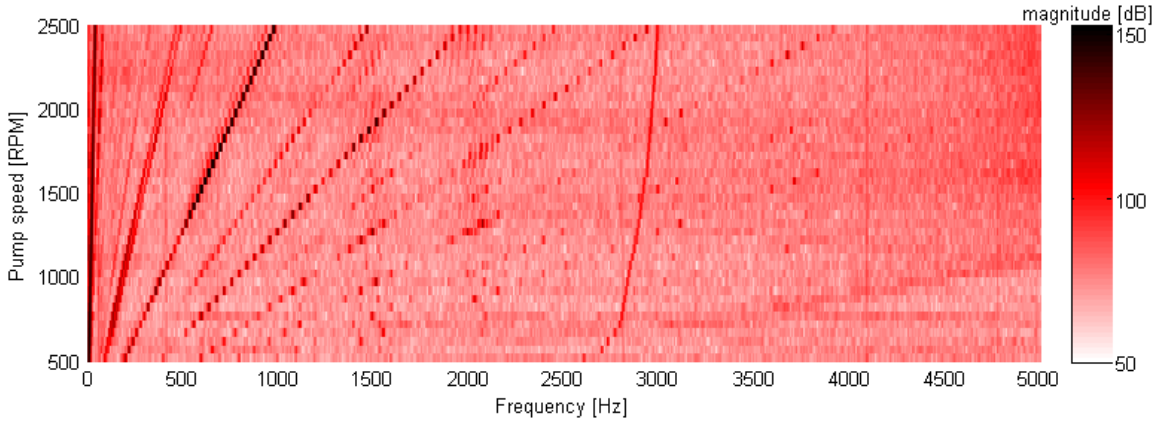

Figure 6.12 Outlet ripple PSD for baseline design.

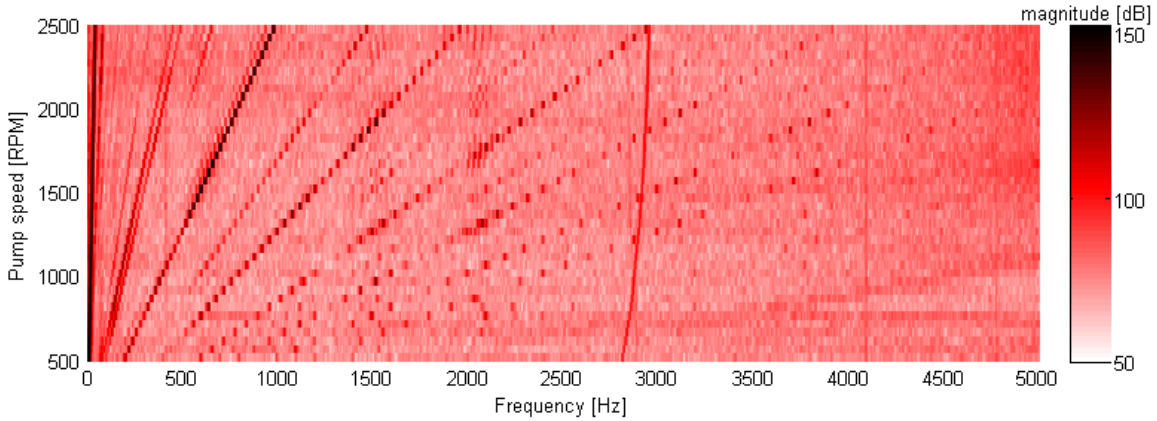

Figure 6.13 Outlet ripple PSD for cavitation design.

As was shown in the earlier figures at a single operating condition, the outlet ripple is very similar between the two designs at most operating conditions. The only significant difference occurs at the shaft frequency, which has a 10 dB larger magnitude for the cavitation design at low pump speeds.

The same power spectral method can also be shown for the measured surface vibration and radiated sound pressure as described in chapter 5. The resulting comparison of the case vibration up to 5 kHz is shown in Figure 6.14 and Figure 6.15.

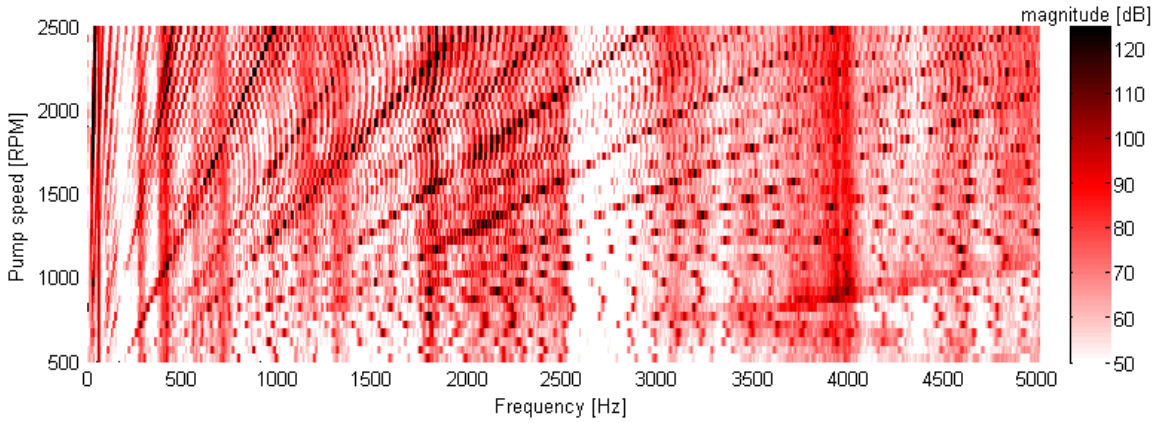

Figure 6.14 Case vibration PSD for baseline design.

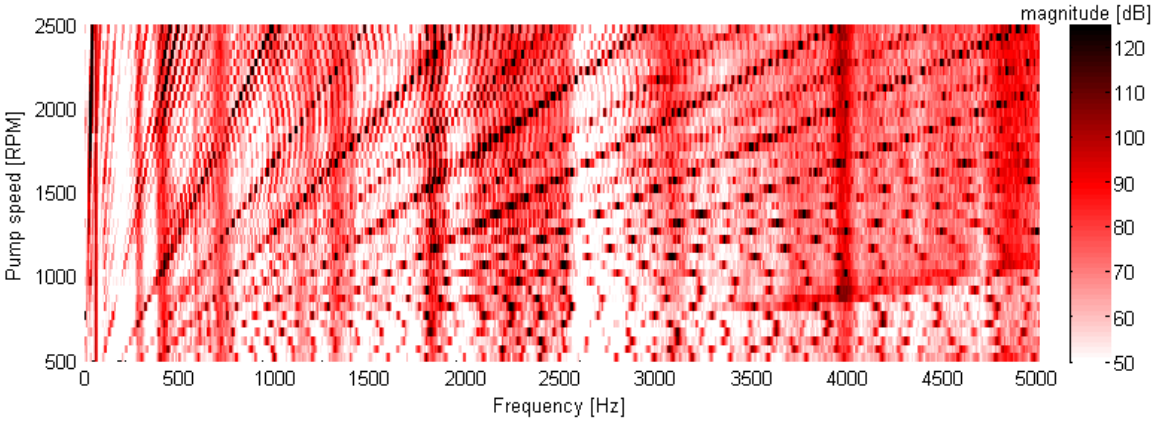

Figure 6.15 Case vibration PSD for cavitation design.

The measured case vibration for the cavitation design shows a tendency for higher magnitude high frequency components showing up as vertical bands. However, the main frequencies measured on the surface acceleration of the two pumps shows very little increase in overall magnitudes of the surface acceleration.

The measured sound pressure power spectra is shown in Figure 6.16 and Figure 6.17.

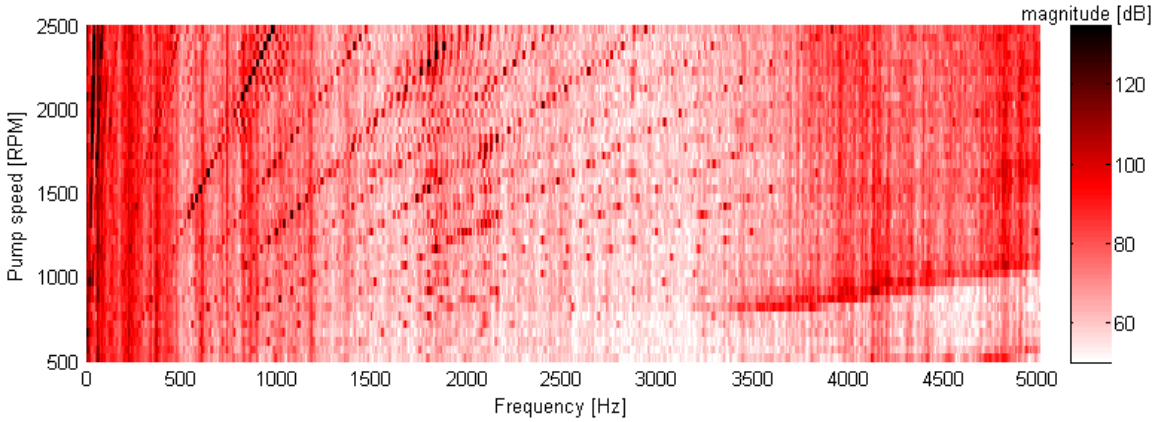

Figure 6.16 Sound pressure PSD for baseline design.

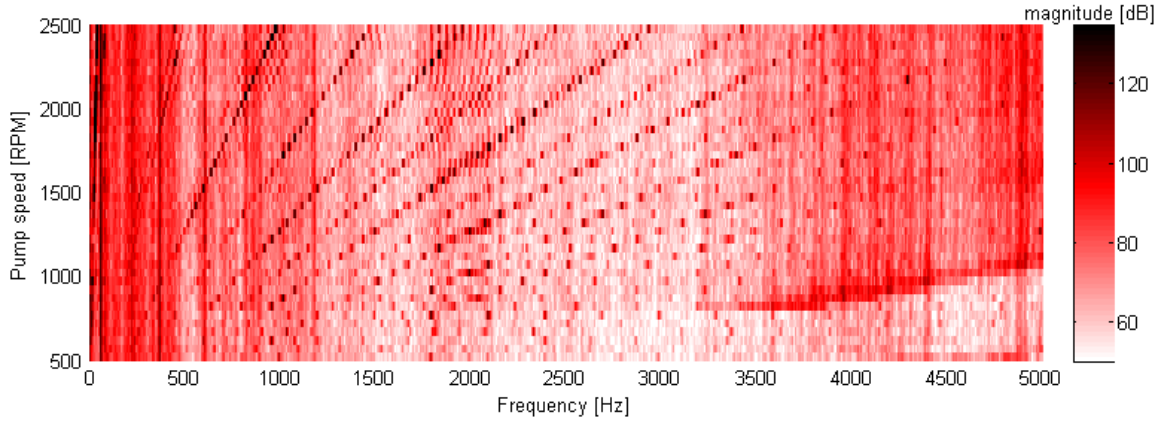

Figure 6.17 Sound pressure PSD for cavitation design.

Similarly to the SBN, the two designs have very similar sound pressures at all frequencies with slightly higher high frequency noise present in the ABN for the cavitation pump. The PSD can be summed across frequency in order to characterize the sound pressure levels at each operating condition. A similar methodology can be used to sum up the measured data in the fluid and structure domains as shown in Figure 6.18. Shown are the results for the baseline standard design and the cavitation design where the grooves are shifted down 2mm. As was explained before, all scales were taken with reference to the sound power ref of 1e-12 W which results in the measured fluid pressure data to be scaled by a factor of 10^5 compared to similar ABN power spectra. The difference is convenient since it places the three different domains on a similar range of decibels, while the important scaling to consider is the difference in decibels between measured signals in the same domain.

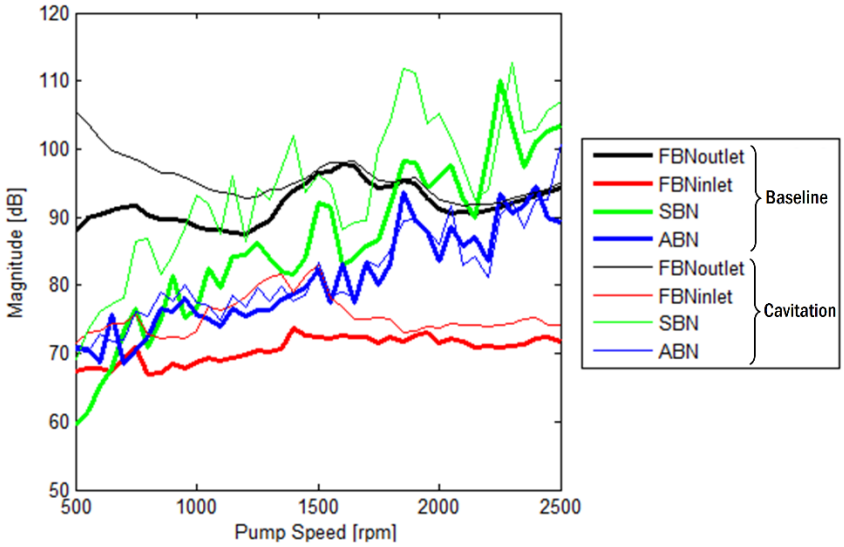

Figure 6.18 Summed PSD for all operating conditions

Comparing the red lines for the inlet ripple first, Figure 6.18 shows that the modified cavitation design is increased in inlet ripple at all operating conditions by an average of 5dB. The outlet ripple is larger in magnitude below 1500rpm due to the increased shaft frequency, and then above 1500rpm is nearly the same between the two designs. The case vibration also shows a large increase and the radiated noise shows a small increase at nearly all operating conditions. For a second comparison, the A-weighting curve was applied to the frequency data and then the data was summed in the same way as before. This A-weighted experimental result is shown in Figure 6.19.

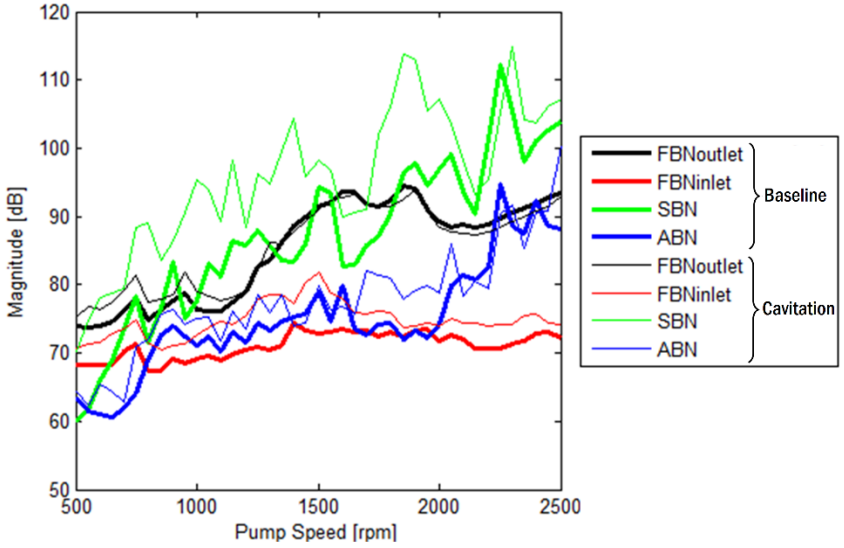

Figure 6.19 A-weighted summed PSD for all operating conditions.

The A-weighting removes most of the shaft frequency that was previously showing a difference between the two designs for the outlet ripple shown in black. The ABN also shows an increase as emphasized in Figure 6.20.

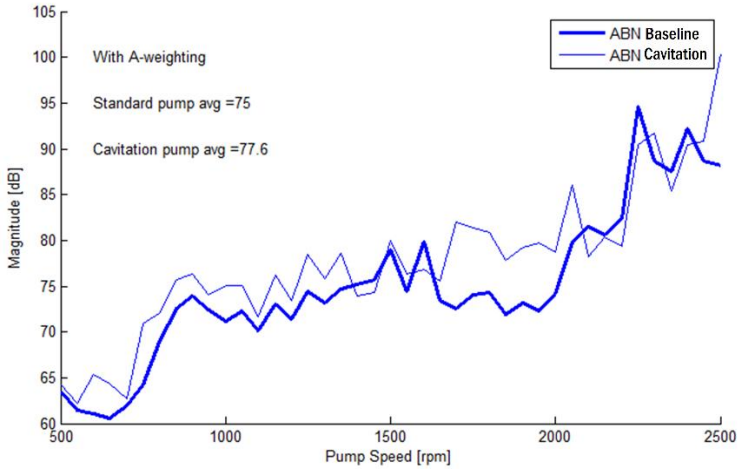

Figure 6.20 A-weighted summed PSD for ABN at all operating conditions.

The design with increase inlet ripple and cavitation shows an average increase of 2.6dB across all operating conditions with maximum of nearly 10dB increase in sound pressure at 1700rpm. This demonstrates that the cavitation and inlet ripple are a contributor to the radiated ABN which deserves more investigation. A final subjective comparison of the noise measured in different domains is shown in Figure 6.21.

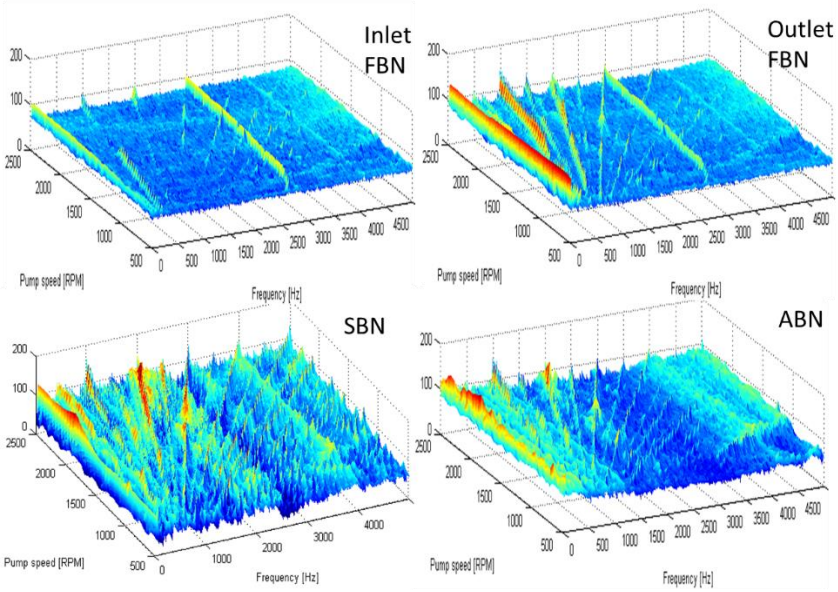

Figure 6.21 Comparing the PSD shapes for different domains.

The similarities in shape again show the importance of the pump driving frequencies in the structural vibration and the radiated sound pressure. There are some similarities in the shape of the inlet FBN vs the ABN in particular the dead portion of the first pump frequency between 2000rpm and 2200rpm. This dead band is not present in the outlet FBN. Furthermore, the general activation of structural resonant frequencies is evident in the SBN and ABN plots with increasing content beginning around 4 kHz which agrees with the acoustic model predictions from before.

6.4 Impact on the acoustic model for increased inlet load

In order to simulate the acoustic impact of an increased inlet load similar to the experimental study completed on Reference Pump #3, the dynamic portion of the inlet ripple predicted by the model for Reference Pump #1 was increased by a factor of 200 as shown in Figure 6.22, please compare to the unmodified force spectra in Figure 3.9.

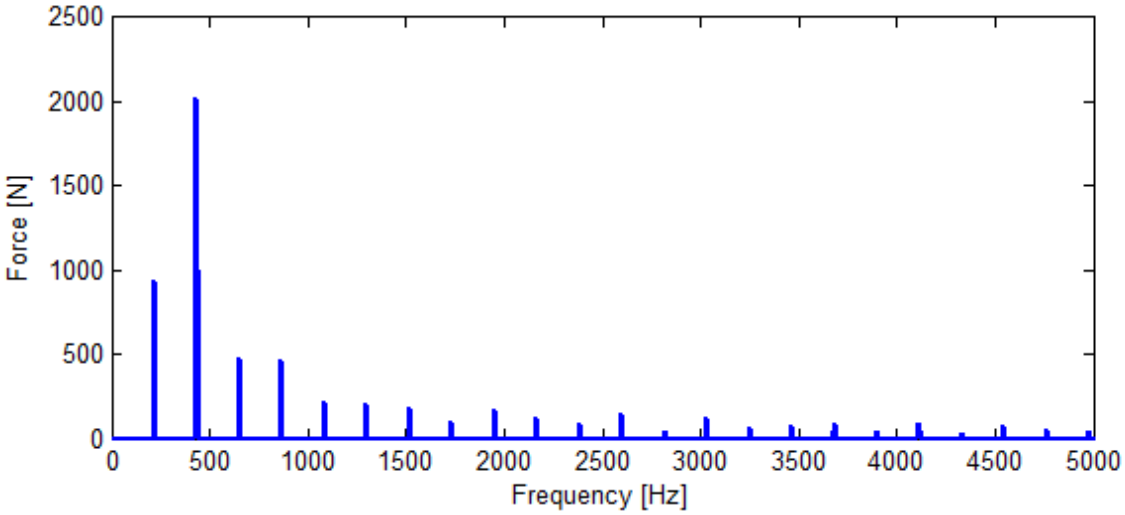

Figure 6.22 Increased inlet dynamic force load by 200x.

The resulting loads are identical to the previously simulated pump #1 at 1000 rpm 100 bar with the replacement of the increased factor on the inlet load as shown in Figure 6.23

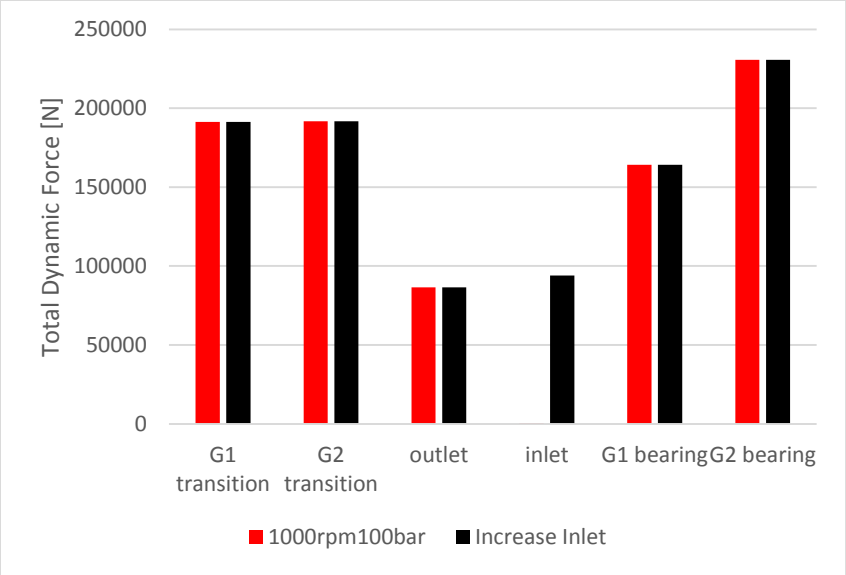

Figure 6.23 Increased inlet load by 200x compared to modeled load.

This magnification of the inlet load increases the total dynamic load applied on the acoustic model by a total of 10.9% on the inlet side, with most of the power from the new inlet ripple term coming at the first several frequency multiples.

The result from the acoustic model as was explained in Chapter 3 predicts effectively a zero increase in the total radiated sound power with the increase in inlet load compared to the standard HYGESim predicted load. This is mainly due to the low radiation efficiency of the pump structure with respect to the low frequency components present in the expanded inlet ripple, and the presence of those same frequency components in the other noise source terms.

However, in the real experiments, an increase in inlet ripple would also increase radiation from the inlet lines and attached structures, this is likely the largest contribution to the measured ABN increase shown in the current study. The potential for induced cavitation noise sources in the experimental study introduced an additional point source of noise due to implosion of gaseous air bubble which was not considered in the acoustic model. These are two important noise sources which were most likely the largest contributors to the larger ABN measured in the experiments.

Again, this study on the sources of noise in Reference Pump #3 investigated the inlet of the pump as a potential source of noise. For that aim, a modified design on

Reference Pump #3 was created in order to measure the difference between a pump that operates with minimal inlet flow ripple and cavitation, and one where there is an extreme amount of induced inlet noise sources. The second part of the study leveraged the previous work using Reference Pump #1 in order to evaluate what the acoustic model would predict for a similar increase in the inlet pressure ripple as what was seen in the experiments. The model result showed that the structural response of the pump body was minimal to the increased inlet load which agrees with the measured vibration of the pump body seen in Figure 6.14 and Figure 6.15. This also indicates that the attached inlet lines and structures as well as the potential for cavitation noise sources were the main contribution to the measured increase in ABN shown in Figure 6.16 and Figure 6.17 and hence were not captured in the model modifications which only considered the modified inlet pressure in the pump.

7. TRANSITION REGION SOURCE DESIGN CASE STUDY

There are two transition regions in typical EGP operation where there are steep transitions in the pressure which results in potential sources of noise. The main of study in previous optimization efforts is the pressure peak and depressurization in the meshing region. However, considering this as a source of noise shows that the forces induced by the depressurization of the chamber show that in order for the forces to propagate out of the body of the pump they must transmit either through the gears and into the journal bearings, or into the lateral pressure plates which are balanced with fluid pressure. Since the journal bearings and lateral plate balance pressures are considered in the acoustic model, the pressurization in the TSV during meshing is already accounted for. The second location that a sharp pressure gradient occurs in an EGP is when the TSV connects to the backflow groove which ports the high pressure fluid back to previous TSVs as discussed in detail in Chapter 3. An investigation was made into decreasing the total noise sources of the pump through smoothing the transition of pressure during the pressurization of each TSV. For this goal, a new groove orifice model was developed and a new TSV pressure profile for Reference Pump #1 was designed and examined for its impact on the predicted radiated noise.

7.1 Model of the displacement chamber pressure rise

For this consideration, a new submodel was developed for HYGESim which allows for the capability for better modeling of backflow groove designs which have narrow connections. The previous model considered typical EGP designs where there is a large connection equivalent to a direct orifice from each TSV to the HP volume. In the previously considered designs, the groove is very large and deep, so the red area is treated in Figure

7.1a is considered as the constricting orifice. However, if the groove depth is small, the constricting orifice instead must be considered as shown in Figure 7.1b where the red part is the maximum flow cross-section. The blue line indicates the geometry of a large backflow groove connecting the TSV to the outlet port.

The pump model prior to this development used the red area in Figure 7.1a as the equivalent area of connection from the TSV directly to the outlet.

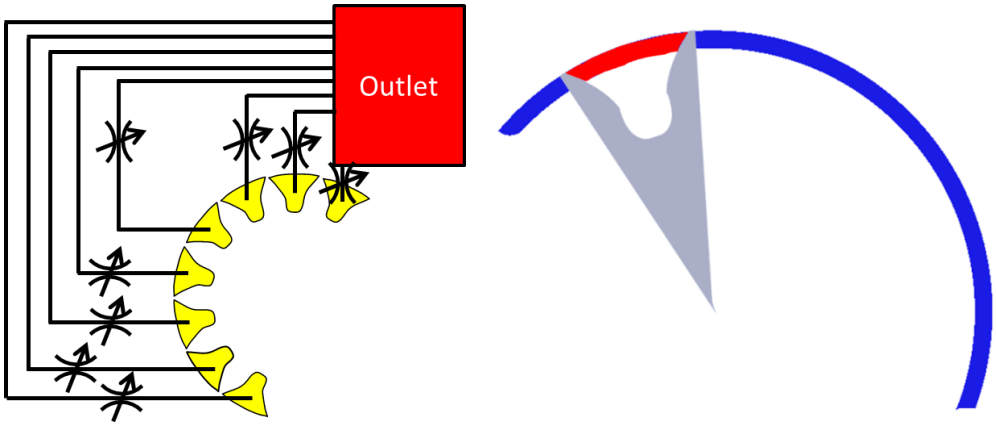

Figure 7.1 (a) Orifice connections for backflow groove. (b) Constricting area.

The prior assumptions of the model for the backflow groove connection is reasonable if the groove is very large, however, the model needed to be developed to include a better approximation of the groove behavior when the groove is very small as shown in Figure 7.2.

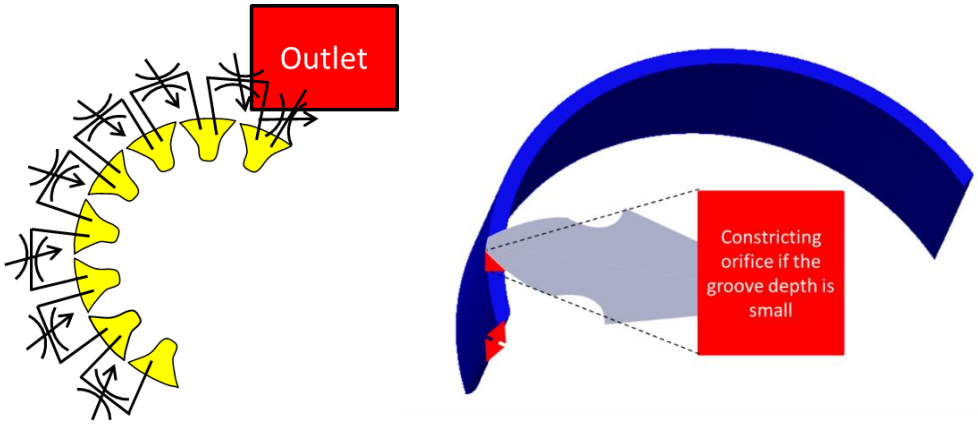

Figure 7.2 (a) Orifice connections between TSVs (b) Small orifice.

The new model development connects the backflow groove calculation internal to the model for the TSVs. An internal orifice connection was coded to port flow between adjacent TSVs according to the constricting orifice size. At the ends of the groove, the prior modeling method is used for when the groove is opening or closing. This allows for tapered ends to the backflow groove as calculated by the standard geometric code while also having a more accurate model for the fluid behavior in a small groove.

The new model developed for this study now allows for optimization of the backflow groove geometry in order to change the pressure rise to a more favorable profile. The initial design goal is to reduce the slope of the pressure rise to a minimum amount within the allowable space, that is, to pressurize the chamber more smoothly.

The goal of this design exercise was to modify the backflow groove for the purpose of changing the slope of the pressure rise from a near a step function smooth curve within the allowed angle of one TSV. Extending the curve beyond the angle of one TSV is impossible since adjacent TSVs would then interfere. The TSV pressure model results are shown in Figure 7.3. In this case of the standard groove, the slope of the pressure rise is nearly vertical. The new groove was designed to have the midpoint of the pressure rise at the same pump rotation angle as the original design at 1000 rpm 100 bar in order to preserve extremely similar gear balancing and hence journal bearing loads between the two cases. This curve is nearly ideal since it uses the entire TSV to accomplish the pressure rise.

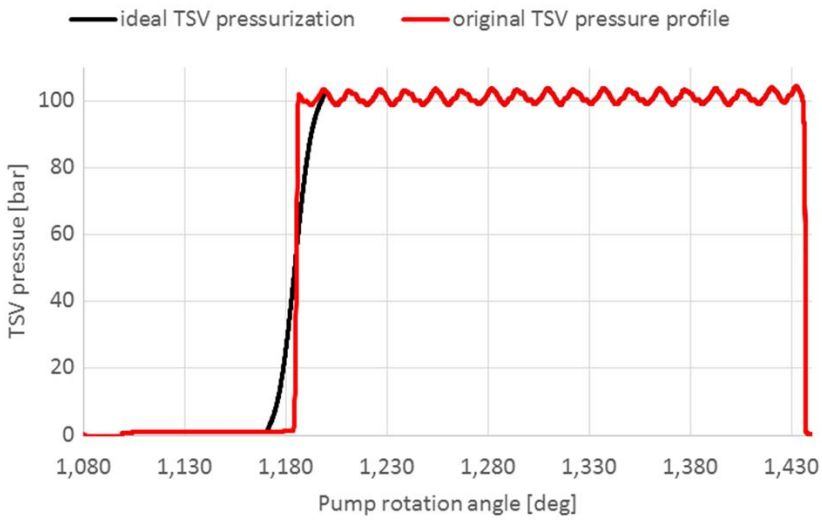

Figure 7.3: TSV pressure for different groove designs.

Furthermore, the new groove has no impact on outlet pressure ripple or volumetric efficiency since no additional leakage is incurred. The proposed modifications are very small, on the same order of magnitude as machining tolerances in the 10 to 100μm range. This means that further study is necessary to understand the feasibility of implementing the new designs as well as the accuracy of the pump model for small magnitude leakages through all gaps becomes paramount since the leakages are on the same scale as the proposed flow through the backflow groove extension. Implementation of the new designs both in acoustic modeling and in experimental prototypes is an area that can be further studied for noise improvement. One possible concern is that other leakages in the pump already achieve some partial effect of the smoother pressure rise, so a new measuring methodology would need to be created in order to accurately capture the improvement in TSV pressure profile.

7.2 Resulting load modifications

Modifying the transition region load conditions using the new smoothed pressure profile is shown in the following 8 figures. Please compare them to Figure 3.13 through Figure 3.20 in the Chapter 3. As was shown in the model introduction to noise sources, first the time domain dynamic force is shown as a function of pump rotation angle, and then the frequency spectra of the force is shown.

The inlet load at the first point on the case in the transition region approaches the profile of a saw tooth wave shown in Figure 7.4 with the frequency spectra shown in Figure 7.5.

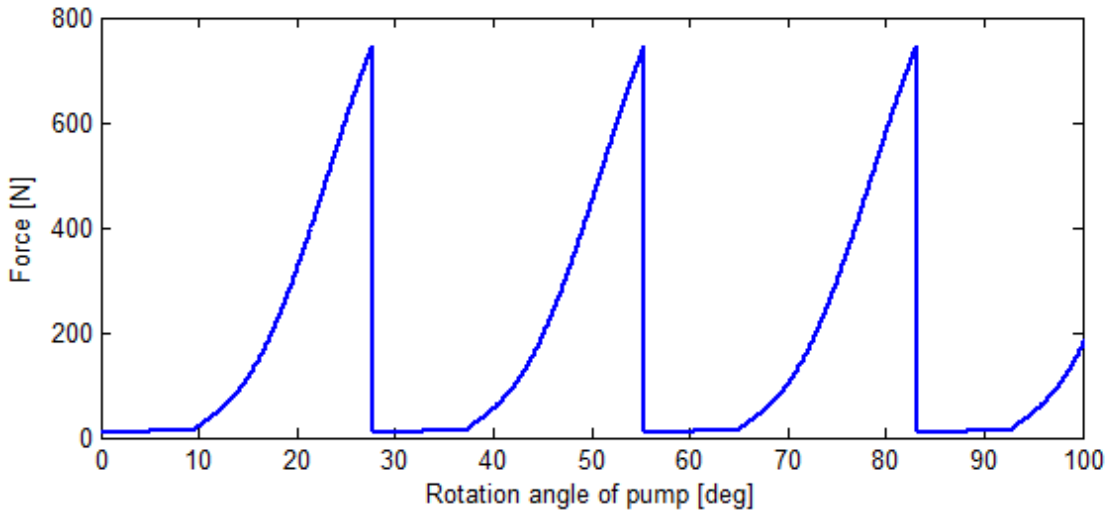

Figure 7.4: Gear 1 position 1 of TSV smooth force 1000 rpm 100 bar.

The frequency spectra is similar in profile to that which was previously seen in chapter 3 for the standard design.

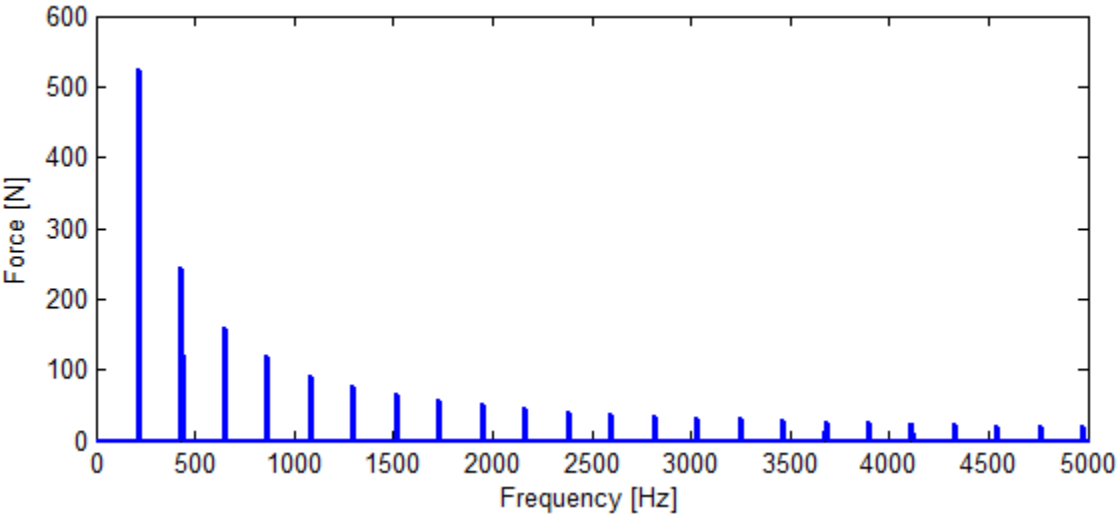

Figure 7.5: Gear 1 position 1 of TSV smooth force 1000 rpm 100 bar FFT.

The second position in the transition region begins to show the improvement in the smoothness of the pressure rise. Effectively half of the pressure gradient hammering seen by the case of the pump has been removed as shown in Figure 7.6.

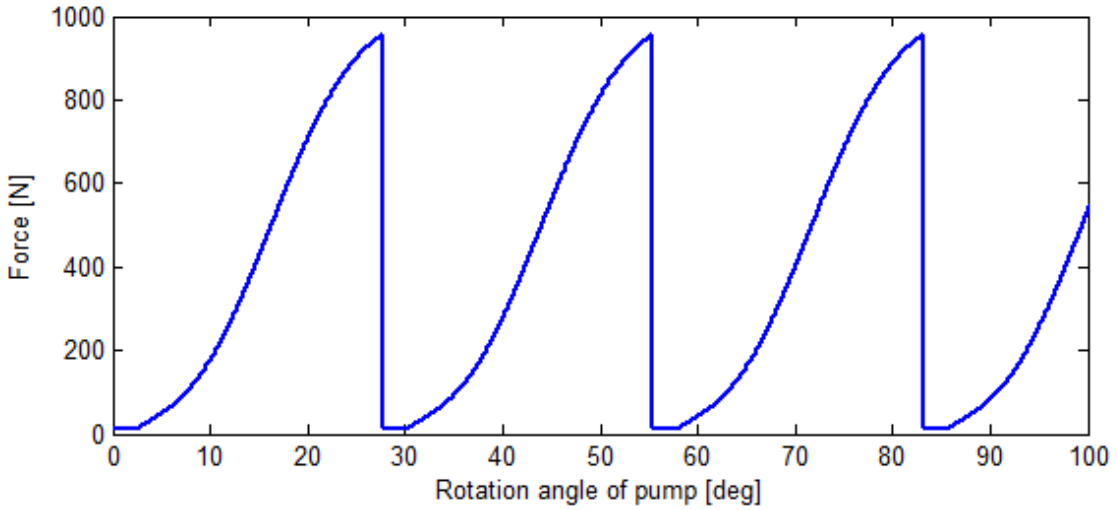

Figure 7.6: Gear 1 position 2 of TSV smooth force 1000 rpm 100 bar.

The frequency spectra has also been greatly decreased in Figure 7.7 compared to the standard design shown in Figure 3.16.

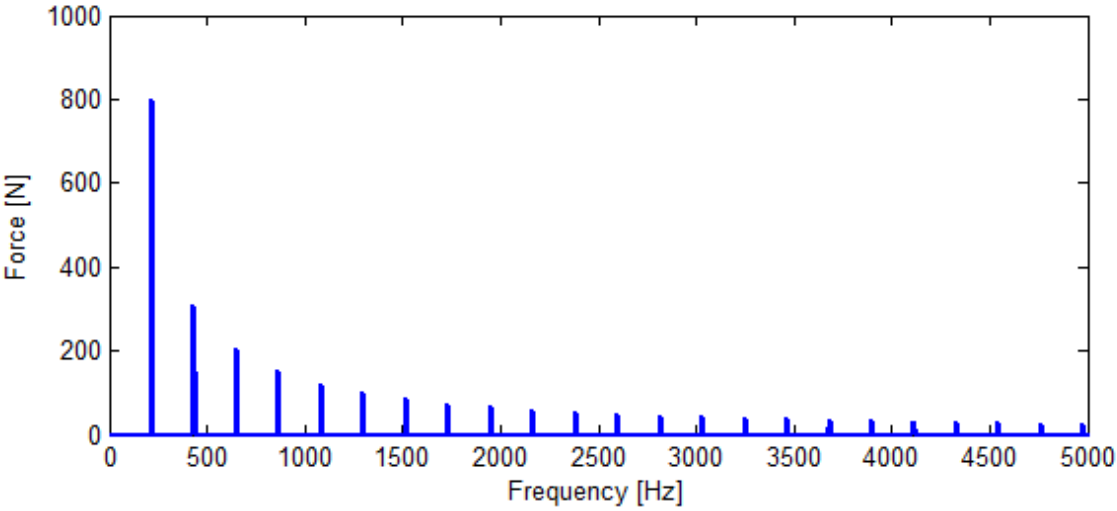

Figure 7.7: Gear 1 position 2 of TSV smooth force 1000 rpm 100 bar FFT.

The third position on the case shows a similar improvement where the general smoothness of the pressure seen by the fixed point on the pump case is greatly improved.

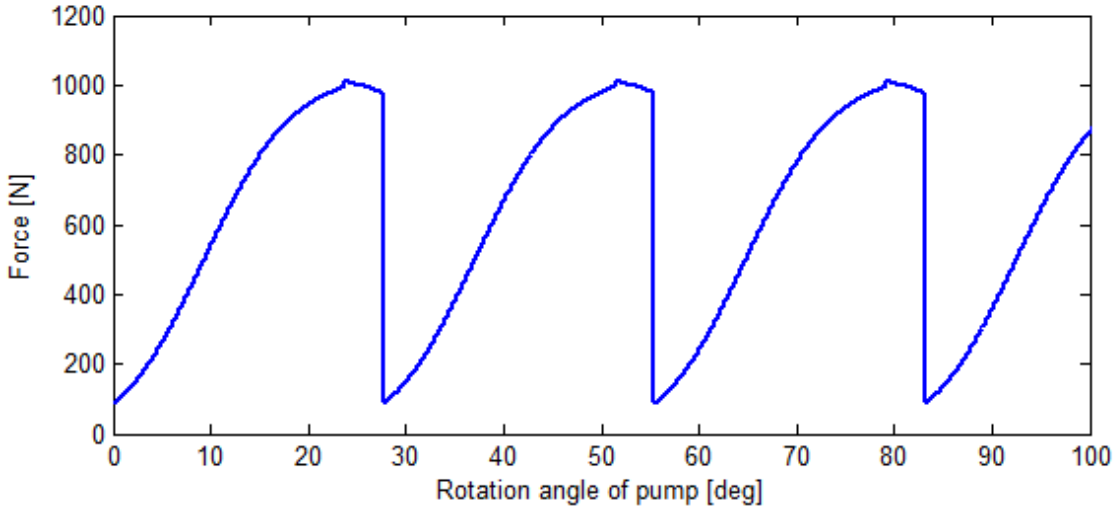

Figure 7.8: Gear 1 position 3 of TSV smooth force 1000 rpm 100 bar.

The improvement in the time domain again causes a large decrease in the frequency components related to the sharp pressure transitions as shown in Figure 7.9.

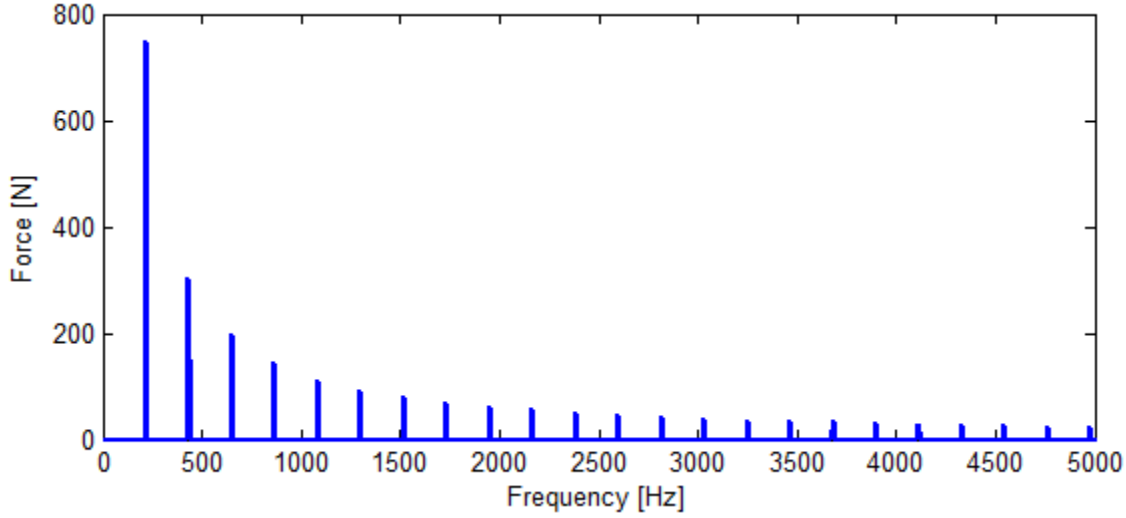

Figure 7.9: Gear 1 position 3 of TSV smooth force 1000 rpm 100 bar FFT.

The fourth and final point on the case in the transition region is very similar to the second and third points, but is included here for completeness and for comparison to the originally simulated design.

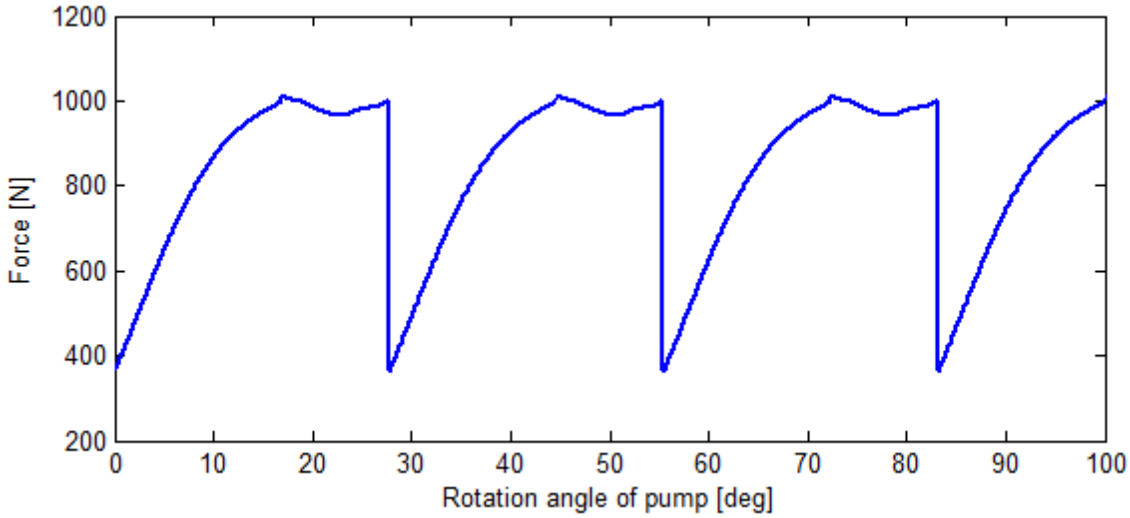

Figure 7.10: Gear 1 position 4 of TSV smooth force 1000 rpm 100 bar.

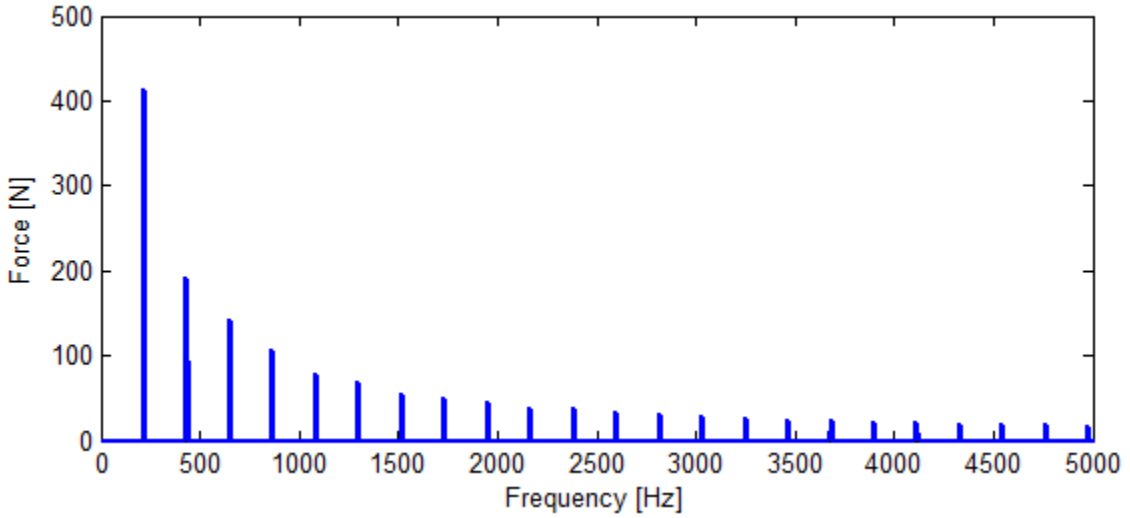

Figure 7.11: Gear 1 position 4 of TSV smooth force 1000 rpm 100 bar FFT.

As was shown in the model introduction, the gear 1 and gear 2 dynamic forces in the transition regions are symmetric, so the driven gear transition forces are not shown here to remain concise. The comparison of simulated results for the smoothing effort at the same four geometrical points is shown in Figure 7.12.

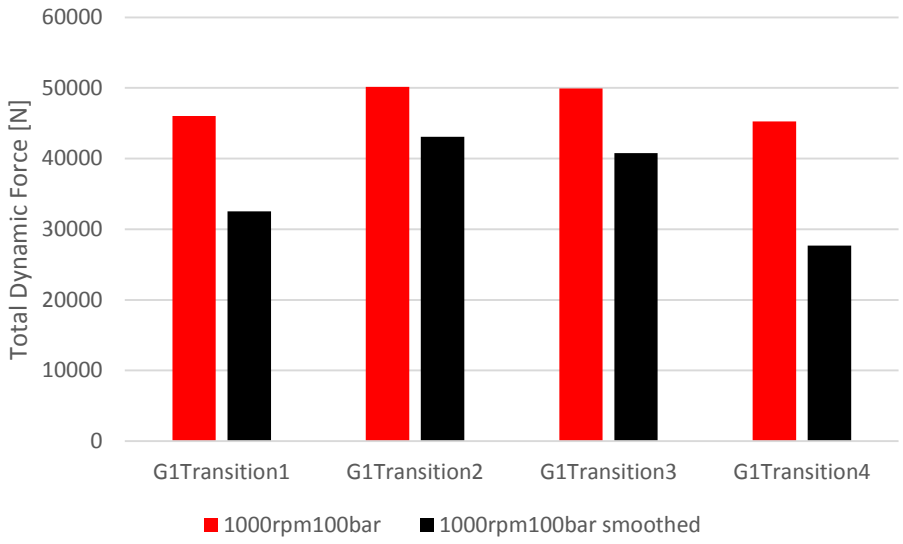

Figure 7.12: Summary of transition dynamic forces for gear 1 at 1000 rpm100 bar.

Considering the load conditions as symmetric leads to a total dynamic force of 144 kN for the smoothed transition region per gear compared to 191 kN for the original transition region. This is a total benefit of 24.8% reduction in the dynamic force on the transition region and an 11.0% reduction in the total predicted noise sources. This also includes a significant decrease in the amount of high frequency noise sources coming from the transition region, which were shown to interact with the pump structure in Chapter 3.

The forces were applied to the simplified structure and the result from the acoustic model shown in Chapter 3 was calculated for the modified transition region. The model predicts a 1.5 dB decrease in the radiated sound power for the smoothed transition pressure profile of 11.0% decrease in source. This shows how the acoustic model can be leveraged to improve current designs and prove the effect of modifications. Where the case study in Chapter 6 which had a similar magnitude change in the sound sources did not show a predicted model improvement in sound radiation from the pump body, the case study shown here does predict an improvement in the radiated noise from the pump. The main reason was that modifying the transition region changes a high frequency source internal to the pump, and hence it effects the radiation from the pump model. However, the inlet ripple change discussed in the Chapter 6 case study has a greater effect on the inlet lines

than the pump body, and hence the experimentally measured increase in sound pressure was not found in the model predictions.

The next steps to prove the concept are to prepare prototypes with modified backflow grooves and test the performance with respect to noise and efficiency. As discussed before, this requires a careful evaluation of the model performance to ensure that the small flows required for smooth pressurization are delivered by the controlled modified groove as opposed to a different leakage source.

8. CONCLUSIONS

In conclusion, a numerical model of the sources of FBN in external gear pumps was improved and investigated. The lumped parameter model HYGESim (HYdraulic GEar machine Simulator) was expanded to investigate the dynamic forces on the solid bodies caused by the pump operation and to predict interactions with the attached system. Vibration and sound radiation were then predicted using a combined finite element and boundary element vibro-acoustic model as well as the influence of additional models for system components to better understand the essential problems of noise generation in hydraulic systems. This model is a step forward for the field due to the coupling of an advanced internal model of pump operation coupled to a detailed vibro-acoustic model. The impact of internal sources on the radiated ABN was shown under a variety of loading conditions. The sources of noise in EGPs were investigated to a deeper level with respect to their influence on the radiated ABN. This was achieved both through experimental studies and through development and analysis of a FBN model for noise generation through adaption and improvement of the HYGESim pump model.

The common assumption that the outlet pressure ripple is the primary source of ABN was challenged through both a combined fluid-dynamic and structural-acoustic model, and also through experimental results at a wide variety of operating conditions. The FEM/BEM model showed the pump body resonances have only a few notable frequencies in the same range as those of the pressure load, and thus at speeds where the FBN frequencies dominate, an improvement in the FBN will likely see a corresponding improvement in the ABN. However, other sources of noise including the chamber pressurization transition region and the gear journal bearing forces have large high frequency components that interact with the pump structural resonances. These internal sources have a large impact on

the sound radiation from the body of the pump. The FBN source in the inlet and outlet lines are still a very important contributor to the total noise of the system. In particular, design of the outlet system and attached lines is key to preventing the FBN sources from propagating out into the attached system. These simulation studies demonstrate that a complete approach is required in order to better understand, and ultimately reduce the noise.

Several experimental studies were also completed in order to advance the current science. The first study validated the pump model in terms of outlet pressure ripple prediction through comparison to experimentally measured results for the reference pump as well as prototype pumps designed for low outlet pressure ripple. The second study focused on the air-borne noise through sound pressure and intensity measurements on reference and prototype pumps at steady-state operating conditions. A third study over a wide range of operating speeds and pressures was completed to explore the impact of operating condition and system design to greater detail through measuring noise and vibration in the working fluid, the system structures, and the air.

The numerical modeling and experimental investigation gives a deeper understanding of the mechanisms of noise generation and how the loading forces propagate out to the ABN. The work shows additional interactions that are not visible in single-domain noise studies, in particular, the impact of the journal bearings and the compressibility effects. The experimental studies give more details as to which components of the pump and system operation have the largest effect on the ABN and thus can be used to predict the effectiveness of future design efforts. A combination of the numerical and experimental approaches allows for deeper insights into the propagation of noise in displacement machines. The presented work and future efforts aid in the development of quieter pumps and motors. Applying the knowledge gained through experimental and simulation studies has brought new advances in the understanding of the physics of noise generation and propagation in hydraulic components and systems. The application of the new modeling and experimental approach allows for new advances which directly contribute to advancing the science of noise in hydraulic applications and the design of new quieter hydrostatic units and hydraulic systems.

8.1 Novel Contributions

The following contributions of this work are considered as novel and advance the science of noise in fluid power components and systems. First, development of the lumped parameter model HYGESim was completed for better modeling of sources of noise in displacement machines. Experimental validation of the pump model through development of a test rig for measuring the FBN was used to verify accuracy of the load sources. A simplified model of the harmonic characteristics of hydraulic lines was also considered in order to better understand the system level interaction introduced by the lines. Next a vibro-acoustic model for sound radiation from the body of an EGP was developed considering all internal sources of noise applied directly to the pump housing. A test circuit for measuring the sound power radiated by EGPs was implemented with a system for controlling the inlet port pressure of the pump. Noise measurements were expanded to account for the noise propagation in the fluid, structure, and air domains to create frequency domain transfer path analysis considering correlations between the different domains. Finally, the previous work was leveraged to analyze the impact of different noise sources including case studies on the inlet and transition regions.

The work demonstrated and published contributions for better understanding of mechanics of noise generation and propagation in displacement machines with the particular case of external gear pumps.

8.2 Publications

8.2.1 Published Journal Papers

Opperwall, T., Vacca, A., 2015/2016, Investigation of noise sources and propagation in external gear pumps, (In preparation).

Opperwall, T., Vacca, A., 2013, A combined FEM/BEM model and experimental investigation into the effects of fluid-borne noise sources on the air-borne noise generated by hydraulic pumps and motors, IMechE Proceedings of the Institution of Mechanical Engineers, Part C, Journal of Mechanical Engineering Science, April 22, 2013.

Opperwall, T., Vacca, A., 2014, Modeling Noise Sources and Propagation in Displacement Machines and Hydraulic Lines, JFPS International Journal of Fluid Power Systems.

8.2.2 Conference Papers and Presentations

Opperwall, T., Vacca, A., 2015, Experiments and Modeling for Quantifying Noise Sources in Hydraulic Pumps, 2015 Fluid Power Innovation & Research Conference, FPIRC15, October 14-16, Chicago, IL.

Opperwall, T., Vacca, A., 2015, A Transfer Path Approach for Experimentally Determining the Noise Impact of Hydraulic Components, SAE ComVEC 2015, October 6-8, 2015, Rosemont, IL, Paper 2015-01-2854.

Opperwall, T., Vacca, A., 2014, Modeling Noise Sources and Propagation in Displacement Machines and Hydraulic Lines, The 9th JFPS International Symposium on Fluid Power, JFPS2014, Oct 28-31, 2014, Matsue, Japan.

Opperwall, T., Vacca, A., 2013, Performing and Interpreting Experiments Towards Understanding Noise Generation in Displacement Machines, The 13th Scandinavian International Conference on Fluid Power, SICFP2013, June 3-5, 2013, Linköping, Sweden.

Vacca, A., Dhar, S., Opperwall, T., 2011, A Coupled Lumped Parameter and CFD Approach for Modeling External Gear Machines, SICFP2011 The Twelfth Scandinavian International Conference on Fluid Power, May 18-20, 2011, Tampere, Finland.

LIST OF REFERENCES

LIST OF REFERENCES

Abbes, M. S., Bouaziz, S., Chaari, F., Maatar, M., and Haddar, M. 2008, An Acoustic-Structural Interaction Modelling for the Evaluation of a Gearbox-Radiated Noise, International Journal of Mechanical Sciences, 50, 569-577.

Balaban, M., 2010, Noise Source Identification and Adoption of Proper Noise Control Strategies on Wheeled Tractors, Middle East Technical University, www.etd.lib.metu.edu.tr.

Bianchi, J., Balmes, E., Vermot des Roches, G., and Bobillot, A., Using modal damping for full model transient analysis, Proceedings of the International Conference on Advanced Acoustics and Vibration Engineering (ISMA), 2010

Binder, R.C., Fluid Mechanics. 3rd Edition, 3rd Printing. Prentice-Hall, Inc., Englewood Cliffs, NJ. 1956

Bonanno, A., and Pedrielli, F., 2008, A Study of the Structureborne Noise of Hydraulic Gear Pumps, 7th JFPS International Symposium on Fluid Power, 641-646.

Casoli P., A. Vacca, G.L.Berta, 2007, Potentials of a Numerical Tool for the Simulation of Flow in External Gear Machines, The Tenth Scandinavian International Conference on Fluid Power, SICFP'07, Tampere, Finland

Casoli, P., Vacca, A., Berta, G.L., 2008, Optimization of Relevant Design Parameters of External Gear Pumps, The Seventh JFPS International Symposium on Fluid Power, September 15-18, 2008, Toyama, Japan

Cho, Y. T., and Bolton, J. S., 2004, Acoustical Visualization of a Refrigeration Compressor by using Statistically Optimized Nearfield Acoustical Holography in Cylindrical Coordinates, NOISE-CON, 175-182.

Choi, J., Lee, H., Lee, J., Park, G., Park, J., Lim, C. and Park, K., 2011, Structural Optimization of an Automobile Transmission Case to Minimize Radiation Noise using the Model Reduction Technique, Journal of Mechanical Science and Technology, 25 (5), 1247-1255.

Citarella R., Federico L., Cicatiello A., 2007, Modal acoustic transfer vector approach in a FEM-BEM vibro-acoustic analysis, Elsevier Engineering Analysis with Boundary Elements, Volume 31 Issue 3, March 2007, 248-258.

Constans, E. W., Belegundu, A. D., and Koopmann, G. H., 1998, Design Approach for Minimizing Sound Power from Vibrating Shell Structures, AIAA Journal, 36 (2), 134-139.

Cremer, L., Heckl, M., and Petersson, B. A. T., 2005, Structure-Borne Sound, Springer, Verlag.

Desmet, W., et al. 2012, Numerical Acoustics Theoretical Manual, LMS International.

Devendran, R., 2012, Novel Design Methodology for External Gear Machines, Master's Thesis, Purdue University.

Devendran R., Vacca A., 2012, Optimal Design of Gears and Lateral Bushes of External Gear Machines, FPMC 2012 Bath/ASME Symposium on Fluid Power and Motion Control, September 12-14 2012, Bath, UK

Devendran, R.S., Vacca, A., 2013, Optimal Design of Gear Pumps for Exhaust Gas Aftertreatment Applications, Simulation Modelling Practice and Theory (Elsevier), vol. 38, pp. 1-19.

Dhar S., Vacca A., 2012, A Novel CFD- Axial Motion Coupled Model for the Axial Balance of Lateral Bushings in External Gear Machines, Elsevier Simulation and Modeling Practice and Theory. 2012; 26: 60-76.

Earnhart, N., Cunefare, K., 2012, Compact Helmholtz Resonators for Hydraulic Systems, International Journal for Fluid Power, 20(13), pp. 41-50, March, 2012.

Edge, K. A., 1999, Designing Quieter Hydraulic Systems – Some Recent Developments and Contributions, Proceedings of the Fourth JHPS International Symposium on Fluid Power, Tokyo, Japan, 3-27.

Engelen, A. J. V., 2009, “Noise Reduction Applied to a Decanter Centrifuge,” University of Canterbury, New Zealand, Christchurch.

Ericson L., Johansson A., and Palmberg J-O., 2009, Noise reduction by Means of Non-uniform Placement of Pistons in Fluid Power Machines in Proceedings of the 2009 ASME Dynamic Systems and Control Conference and Bath/ASME Symposium on Fluid Power & Motion Control Theme: System Engineering, Hollywood, Ca, USA October 12-14 2009

Fiebig, W., 2007, Location of Noise Sources in Fluid Power Machines, International Journal of Occupational Safety and Ergonomics, 13 (4), 441-450.

Fiebig, W., and Helle, K., 2010 The New Way of Noise Reduction in External Gear Pumps, 7th International Fluid Power Conference Aachen.

Gerges, S. N. Y., Johnston, D. N., and Rocha, L.Z., 2011, Handbook of Hydraulic Fluid Technology, CRC Press, 447-460.

Hartmann K., Harms H.H, Lang T. 2012 A Model Based Approach to Optimize the Noise Harmonics of Internal Gear Pumps by Reducing the Pressure Pulsation, 8th International Fluid Power Conference (IFK), March 26-28, 2012, Dresden, Germany

ISO International Standard, 1989, Acoustics – Determination of Sound Power Levels using Sound Intensity – Measurement at Discrete Points, ISO/DIS 9614-1.

ISO International Standard, 2003, Hydraulic Fluid Power – Test Code for the Determination of Sound Power Levels using Sound Intensity Techniques: Engineering method – Part 1: Pumps, ISO 16902:2003(E).

ISO International Standard, 1996,“Hydraulic Fluid Power- Determination of Pressure Ripple Levels Generated in Systems and Components - Part 1: Precision Method for Pumps, ISO 10767-1:1996(E).

ISO International Standard, 1999. Hydraulic Fluid Power- Determination of Pressure Ripple Levels Generated in Systems and Components - Part 2: Simplified Method for Pumps, ISO 10767-2:1999(E).

ISO International Standard, 2001. Hydraulic Fluid Power- Determination of Fluid-borne Noise Characteristics of Components and Systems – Part 1: Introduction, ISO 15086-1:2001(E).

Ivantysyn, J., and Ivantysynova, M., 2001, Hydrostatic Pumps and Motor, Principles, Designs, Performance, Modeling, Analysis, Control and Testing, Academic Books International, New Delhi.

Jeannon, J. M., and Cockreel, D. J., 1975, Acoustic Radiation of Rotary Positive Displacement Machinery, Journal of Sound and Vibration, 39 (2), 181-193.

Kela, L., 2010, Adaptive Helmholtz Resonator in a Hydraulic System, World Academy of Science, Engineering and Technology, 68, 1180-1187.

Kesseler, C. L., 1999, Complex Modal Analysis of Rotating Machinery, Division of Research and Advanced Studies of the University of Cincinnati.

Klop, R., and Ivantysynova, M, 2008, Investigation of Noise Source Reduction Strategies in Hydrostatic Transmissions, Proceedings of the 5th FPNI PhD Symposium, Cracow, Poland, 63-76.

Klop, R., and Ivantysynova, M., 2008, Influence of Line Length Concerning Noise Source Generation in Hydrostatic Transmissions, SAE International Commercial Vehicle Engineering Congress & Exhibition, Rosemont, IL, USA, 2008-01-2722.

Klop, R, 2010. Investigation of Hydraulic Transmission Noise Sources, PhD thesis, Purdue University.

Klop, R. and Ivantysynova, M. 2010. Sound Intensity Measurements to Investigate Noise Generation of Hydrostatic Transmissions Proceedings of the 7th International Fluid Power Conference Aachen 2010 (7IFK), Vol. 2, 229-242

Lau, G. K., and Du, H., 2004, Topology Optimization of Head Suspension Assemblies using Modal Participation Factor for Mode Tracking, Microsyst Technol, 11, 1243-1251.

Lätzel, M. Schwuchow, D., 2012, An innovative external gear pump for low noise applications 8th International Fluid Power Conference (IFK), March 26-28, 2012

McCulloch, C., Tournour, M., and Guisset, P., 2002, Modal Acoustic Transfer Vectors Make Acoustic Radiation Models Practical for Engines and Rotating Machinery, www.easc.ansys.com.

McKee, R., Broerman, E., 2009, Acoustics in Pumping Systems, Proceedings of the Twenty-Fifth International Pump User Symposium, Houston, TX, Feb 23-26, 2009.

Moore, P., Slot, H., Li, H., and Boersma, B. J., 2007, Simulation and Measurement of Flow Generated Noise, Journal of Computational Physics, 224, 449-463.

Mucchi, E., Dalpiaz, G.,and Fernåndez del Rincòn, A., 2010, Elastodynamic Analysis of a Gear Pump. Part I: Pressure Distribution and Gear Eccentricity, Mechanical Systems and Signal Processing, 24, 2160-2179.

Mucchi, E., and Dalpiaz, G., and Rivola, A., 2010, Elastodynamic Analysis of a Gear Pump. Part II: Meshing Phenomena and Simulation Results, Mechanical Systems and Signal Processing, 24, 2180-2197.

Nandi, S. K., 2004, Finite Element Analysis for Acoustic Behavior of a Refrigeration Compressor, www.ansys.com.

Negrini, S., 1996, A Gear Pump Designed for Noise Abatement and Flow Ripple Reduction International Fluid Power Exposition and Technical Conference. 23-25 April 1996.

Opperwall, T., Vacca, A., 2013, A combined FEM/BEM model and experimental investigation into the effects of fluid-borne noise sources on the air-borne noise generated by hydraulic pumps and motors, IMechE Proceedings of the Institution of Mechanical Engineers, Part C, Journal of Mechanical Engineering Science, April 22, 2013.

Opperwall, T., Vacca, A., 2014, Modeling Noise Sources and Propagation in Displacement Machines and Hydraulic Lines, The 9th JFPS International Symposium on Fluid Power, JFPS2014, Oct 28-31, 2014, Matsue, Japan.

Opperwall, T., Vacca, A., 2013, Performing and Interpreting Experiments Towards Understanding Noise Generation in Displacement Machines, The 13th Scandinavian International Conference on Fluid Power, SICFP2013, June 3-5, 2013, Linköping, Sweden.

Ortwig, H., 2005, Experimental and Analytical Vibration Analysis in Fluid Power Systems, International Journal of Solids and Structures, 42, 5821-5830.

Occupational Safety and Health Administration, 1991-2015, Occupational noise exposure, Occupational Safety and Health Standards 1910.95, https://www.osha.gov/.

Picó, R., Gautierb, F., and Redondoa, J., 2007, Acoustic input impedance of a vibrating cylindrical tube, Journal of Sound and Vibration, Elsevier. Volume 301

Plunt J., 2005, Examples of using Transfer Path Analysis (TPA) together with CAE-models to diagnose and find solutions for NVH problems late in the vehicle development process, SAE 2005-01-2508.

Puri, R. S., Moorey, D., Durodola, J. F., Morgans, R. C., and Howard C. Q., 2007, "A Comparison of Structural-Acoustic Coupled Reduced Order Models (ROMS): Modal Coupling and Implicit Moment Matching via Arnoldi," 14th International Congress on Sound and Vibration.

Sandberg, G., and Ohayon, R., 2009, Computational Aspects of Structural Acoustics and Vibration, Springer.

Schleihs, C., Murrenhoff, H., 2014, Modal Analysis Simulation and Validation of a Hydraulic Motor, Proceedings of the 9th JFPS International Symposium on Fluid Power, Matsue Japan, Oct. 28-31, 2014.

Schleihs, C., Murrenhoff, H., 2015, Acoustical Simulation of a Hydraulic Swash Plate Motor, Proceedings of the ASME/BATH 2015 Symposium on Fluid Power & Motion Control, Chicago Illinoise, Oct. 12-14, 2015.

Seeniraj, G.K., 2009, "Model based Optimization of Axial Piston Machines Focusing on Noise and Efficiency," PhD thesis, Purdue University, USA.

Seeniraj, G. and Ivantysynova, M. 2008. Multi-objective Optimization Tool for Noise Reduction in Axial Piston Machines. SAE International Journal of Commercial Vehicles.1(1):544-552, 2008

Seeniraj, G. and Ivantysynova, M. 2011. A Multi-Parameter Multi-Objective Approach to Reduce Pump Noise Generation. International Journal of Fluid Power, Vol. 12, No. 1, pp. 7 - 17.

Seo, J. H., Moon, Y. J., and Shin, B. R., 2008, Prediction of Cavitating Flow Noise by Direct Numerical Simulation, Journal of Computational Physics, 227, 6511-6531.

Seror, C., Sagaut, P., Bailly, C., and Juvé, D., 2001, On the Radiated Noise Computed by Large-Eddy Simulation, Physics of Fluids, 13 (2). 476-487.

Singhal, A. K., Athavale, M. M., Li, H., and Jiang, Y., 2002, Mathematical Basis and Validation of the Full Cavitation Model, Journal of Fluids Engineering, 124, 617-624.

Siemens AG, Transfer Path Analysis, © 2015 Siemens Product Lifecycle Management Software Inc. Corporate Information, http://www.plm.automation.siemens.com /en_us/products/lms/testing/transfer-path-analysis.shtml

Skaistis, S., Noise Control of Hydraulic Machinery, 1988, Marcel Dekker Inc, New York, New York.

Subani, N., Amin, N., 2015, Analysis of Water Hammer with Different Closing Valve Laws on Transient Flow of Hydrogen-Natural Gas Mixture, Hindawi Publishing Corp. Abstract and Applied Analysis, Vol. 2015, ID 510675.

Thiagarajan D., Dhar S., Vacca A., 2014, A Novel Fluid Structure Interaction-EHD Model and Optimization Procedure for an Asymmetrical Axially Balanced External Gear Machine, Tribology Transactions (accepted, available online from Oct. 1, 2014).

Usuda, S., Otsuka, M., Nagata, M., 2002, Noise Vibration Reduction of Newly Developed 3.0 I direct injection diesel engine. Elsevier JSAE Review, Vol. 23, Issue 3, pp. 285-289.

Vacca A., Guidetti M., 2011, Modelling and Experimental Validation of External Spur Gear Machines for Fluid Power Applications, Elsevier Simulation Modelling Practice and Theory, 19, 2007–2031.

Vacca A., Dhar S., Opperwall T., 2011, A Coupled Lumped Parameter and CFD Approach for Modeling External Gear Machines, The Twelfth Scandinavian International Conference on Fluid Power, Tampere, Finland.

Vassena A., Vacca A., 2010, Design Optimization of the Sliding Elements of External Gear Machines, 6th FPNI – PhD Symposium, June 15-19 2010, West Lafayette (IN), USA

Wang, C., Lai, J. C. S., and Astfalck, A., 2004, "Sound Power Radiated from an Inverter Driven Induction Motor II: Numerical Analysis," IEE Proc. Electr. Power Appl., 151 (3), 341-348.

Wang, S. et. al.,Numerical modeling and analysis of external gear pumps by applying generalized control volumes, Mathematical and Computer Modelling of Dynamical Systems, Volume 17, Issue 5, 2011

Yamazaki, T., and Kojima, E., 2003, Prediction of Sound Power Radiated from Oil Hydraulic Pump using FEM and BEM, Acoustic Science & Technology, 24 (2), 103-105.

VITA

VITA

Timothy Opperwall was born on March 8, 1988 in Dearborn, Michigan. He developed a strong interest in science and engineering in high school thanks to encouragement from his parents and excellent teachers. He received his Bachelors of Science in Engineering with a mechanical engineering concentration and mathematics minor in 2010 from Calvin College in Grand Rapids, Michigan. During his time at Calvin he enjoyed a hands-on internship with Innotec Group, completed a senior design project doing development work on a six-stroke engine, and worked on several research projects under Professor Richard De Jong which sparked an interest in noise and vibration. In August of 2010 he moved to Lafayette, Indiana to work under Professor Andrea Vacca at the Maha Fluid Power Research Center of Purdue University, where he completed his Master of Science in Mechanical Engineering degree. He then continued on in doctoral work under Professor Vacca through graduation in December of 2015. After graduation, Tim accepted a position at Husco International in Waukesha, Wisconsin. His research interests through graduate work and beyond include component design, simulation models, and experimental studies. These topics are aimed towards a focus on improving the noise performance of hydraulic components and systems.